

University of Ulm  
Department of Inner Medicine II  
Medical Director: Prof. Dr. Vinzenz Hombach



ulm university universität  
**uulm**

**MRI studies of Gadolinium based Contrast Agents loaded  
Nanocapsules and Iron loaded Nanoparticles in Chemical and  
Biological environment**

Dissertation

Submitted to the

Medical Faculty of the University of Ulm  
for the degree of Doctor of human biology

Presented by

Sonu Sharma, born in Rajasthan, India

2009

Dean of the Faculty: Prof. Dr. Klaus-Michael Debatin

1<sup>st</sup> Reviewer: Prof. Dr. rer. nat. Volker Rasche

2<sup>nd</sup> Reviewer: Prof. Dr. Katharina Landfester

Day of grant of Doctorate: 13.11.09

*Dedicated to my Parents*

# Contents

<b>List of frequently used symbols</b>	vi
<b>List of abbreviations</b>	vii
<b>1. Introduction</b>	1
1.1 Basics of MRI .....	1
1.2 Relaxation .....	8
1.3 Spin Echo Experiment .....	12
1.4 Contrast .....	13
1.5 Spatial encoding of the MR signal .....	17
1.6 MRI pulse sequences .....	22
1.7 Contrast agents in MRI .....	30
1.8 Relaxivity .....	33
<b>2. Relevant Methods For Characterization</b>	40
2.1 Dynamic Light Scattering .....	41
2.2 Inductively Coupled Plasma -Optical Emission Spectroscopy .....	44
2.3 Transmission Electron Microscopy.....	45
2.4 Scanning Transmission Electron Microscope .....	47
2.5 Energy Filtered Transmission electron microscopy.....	48
2.6 Energy Dispersive X-ray Spectroscopy.....	49
2.7 Fourier Transform Infrared Spectroscopy .....	50
2.8 $T_1$ quantification using Look-Locker Method.....	52
2.9 $T_2$ and $T_2^*$ quantification by MRI .....	54
<b>3. Characterization of MRI contrast agent loaded polymeric nanocapsules as versatile vehicle for targeted imaging</b>	
A An inverse miniemulsion approach	57
3A.1 Materials and Methods .....	61
3A.2 Results and Discussion.....	67
3A.3 Conclusion.....	81
B Gel Approach	82



3B.2	Materials and Methods .....	83
3B.3	Results and Discussion .....	84
3B.4	Conclusion .....	89
4.	<b>Studies of iron loaded nanoparticles and iron labeled Mesenchymal Stem cells by MRI</b>	91
4.1	Materials .....	95
4.2	Methods.....	96
A	<b>MR studies of iron loaded nanoparticles and Resovist®</b>	99
4A.1	Agarose phantom preparation .....	99
4A.2.	Results and Discussion .....	99
4A.3	Conclusion .....	100
B	<b>MR imaging of Resovist®/PLL labeled MSCs cells</b>	109
4B.1	Agarose phantom preparation .....	109
4B.2	Results and Discussion.....	110
4B.3	Conclusion .....	112
C	<b>Study of kinetic behavior of Resovist® labeled cells by MRI</b>	113
4C. 1	Agarose phantom preparation .....	113
4C. 2	Results and Discussion .....	113
4C.3	Conclusion .....	119
D	<b>Study of kinetic behavior of MU 19-5zdz N3+N4 labeled cells by MRI</b>	119
4D.1	Agarose Phantom preparation.....	119
4D.2	Results and Discussion.....	120
4D.3	Conclusion .....	123
4.3	Overall summary	125
5.	<b>Quantification of calcifications in endarterectomy samples by means of high – resolution ultra-short echo time (UTE) imaging.</b>	127
5.1	Materials and Methods .....	129
5.2	Results .....	133
5.3	Discussion .....	139
5.4	Conclusion .....	140
	<b>Summary</b>	141
	<b>References</b>	143
	<b>Acknowledgment</b>	191

## LIST OF SYMBOLS

$B_0$	Main/Static magnetic field of MRI
$B_1$	Radio frequency/oscillating field of MRI
Gd	Gadolinium
$M_Z$	Longitudinal Magnetization (parallel to the main magnetic field)
$M_{xy}$	Transverse Magnetization (perpendicular to the main magnetic field)
$M_0$	Equilibrium Longitudinal Magnetization
$r_1$	Longitudinal relaxivity (unit $\text{mM}^{-1}\cdot\text{s}^{-1}$ )
$r_2$	Transverse relaxivity (unit $\text{mM}^{-1}\cdot\text{s}^{-1}$ )
$R_2^*$	Effective transverse relaxation rate in gradient echo sequences ( $\text{s}^{-1}$ )
$R_1$	Longitudinal relaxation rate ( $\text{s}^{-1}$ )
$R_2$	Transverse relaxation rate ( $\text{s}^{-1}$ )
T	Tesla
$T_1$	Longitudinal relaxation constant
$T_2$	Transverse relaxation constant
$T_2^*$	Effective spin-spin relaxation time (due to field inhomogeneities)
$\tau_R$	Rotational Correlation time
$\mu$	Magnetic moment
$\omega$	Angular frequency
$\gamma$	Gyromagnetic ratio (42.6 MHz/T for $^1\text{H}$ )
$\chi$	Susceptibility of a medium (unit less in SI units). The slope of the linear correlation between induced magnetisation and applied magnetic field.

## LIST OF ABBREVIATIONS

CA	Contrast agent
CTMA-Cl	Cetyltrimethylammonium chloride
CT	Computed tomography
DTPA	Diethylene triamine pentaacetic acid
FFE	Fast field echo sequence
FOV	Field of view
GRE	Gradient echo
HDS	High density seeded
ICP-OES	Inductively coupled plasma - optical emission spectroscopy
LDS	Low density seeded
MSCs	Mesenchymal stem / stromal cell
nm	nanometer
PLLA	Poly-L-lactic acid
PLL	Poly-L-lysine
PMI	Perylenmonoimide
ROI	Region of Interest
SE	Spin echo
SI	Signal Intensity
SDS	Sodium n-dodecyl sulfate
SPIO	Superparamagnetic iron oxide particles
TE	Echo time
TEM	Transmission electron spectroscopy
TR	Repetition time
USPIO	Ultrasmall superparamagnetic iron oxide particles
UTE	Ultrashort Echo time

## Objective of the thesis

Detection of atherosclerotic plaque by noninvasive methods, such as MRI, allows us to study the plaque composition at a cellular and molecular level. Normally study of these plaques by MRI is accomplished by using molecular probes that can accurately and sensitively bind or target specific molecular and functional components of atherosclerotic plaque. However, molecular imaging by MR is challenging due to the fact that molecular targets are often present in very small numbers ( $10^{-9}$  to  $10^{-13}$  M/g tissue). Therefore, the high concentration of contrast agent necessary for detection, severely limits the application of MRI for monitoring molecular processes in vivo. As a result, improved imaging strategies and/or targeted molecular imaging contrast agents (that are able to deliver large payloads of an MR active label) are needed to further improve the detection and characterization of vulnerable plaques using MRI techniques.

Keeping in mind to achieve the goal of targeted molecular imaging for plaque characterization in future, the objectives of this thesis are:

- To develop and test the potential use of polymeric vehicles (in chemical and biological environment) which can carry high payload of contrast agents as potential candidate to do targeted molecular imaging.
- Another aspect is optimization of the MRI sequences to differentiate the signal loss generated by calcium and its future application to the imaging of iron based contrast agents to improve the differentiation between signal losses generated by iron based contrast agents and signal loss due to presence of calcium in plaque.

The thesis is structured as follows: Chapter 1 gives a qualitative treatment of the basic principles of MRI, as it is used as a main analytical tool in this work. Further an overview of  $\text{Gd}^{3+}$  and Fe based contrast agents is given in this chapter to understand the behavior of these metal ions in different chemical and biological environments like polymeric nanocapsules, mesenchymal stem cells as discussed in the subsequent chapters. Chapter 2 deals with a brief introduction about different analytical instruments used in this work besides MRI. Chapter 3

deals with the development and characterization of polymeric nanoshell encapsulated  $\text{Gd}^{3+}$  based commercially available contrast agents (Magnevist<sup>®</sup>, Gadovist<sup>®</sup> and Multihance<sup>®</sup>) synthesized by inverse miniemulsion technique.  $T_1$  relaxivity of the resultant contrast agents loaded nanocapsules were assessed at 1.5T MRI scanner. These nanocapsules were also characterized by different physico chemical characterization techniques like Fourier transform infrared spectroscopy (FT-IR), energy filtered transmission electron microscopy (EFTEM), scanning transmission electron microscopy (STEM), and energy dispersive x-ray (EDX) spectroscopy to localize the position of  $\text{Gd}^{3+}$  in these nanocapsules. Further preliminary MRI results obtained by using gels in the synthesis of polymeric nanocapsules for encapsulating the commercial contrast agents like Magnevist<sup>®</sup> are given in this chapter. Chapter 4 deals with MRI studies of Fe based contrast agent Resovist<sup>®</sup> and iron-PLLA nanoparticles synthesized by miniemulsion technique.  $T_2$  and  $T_2^*$  behavior of these particles along with their relaxivities were measured at 3T MRI scanner. Further, to study the behavior of these particles in biological environment, MRI studies of MSCs cells labeled with these particles were done regard to their cell numbers, iron distribution and uptake behavior. All these MRI studies were done using conventional  $T_2/T_2^*$  weighted sequence. However the negative contrast in MR images obtained using conventional  $T_2/T_2^*$  weighted sequences can be confused with signal loss caused by other sources like presence of calcium in plaque. Thus in chapter 5 attempt was made to detect the presence of calcium in endartecomy samples by using UTE sequence (TE = 50  $\mu\text{s}$ ) and comparison has been made between the images obtained from  $T_1\text{W}$  gradient echo sequence (TE = 5.7 ms), high-resolution volume CT (VCT) and histology.

# Chapter 1

## Introduction

The main aim of this chapter is to review some of the basic concepts of MRI which is the main analytical tool used in this study. This chapter focuses on the basics of MRI (section 1.1) followed by the origin of intrinsic contrast (section 1.4) in MRI. The intrinsic contrast can be enhanced by adding external chemical substances called contrast agents. Thus, section 1.7 describes types of contrast agents and how they affect the MRI relaxation properties. Since efficiency of these contrast agents is described by its relaxivity, a detailed description about the parameters, which affect the relaxivity and can be altered to enhance the relaxivity, is presented in section 1.8.

## 1.1 Basics of MRI

### 1.1.1 Magnetic moment (spin) $\mu$ of a single nucleus

Hydrogen has a significant magnetic moment and is nearly 100% abundant in the human body. For this reason medical magnetic resonance (MR) imaging uses the signal from the nuclei of hydrogen atoms ( $^1\text{H}$ ) for image generation. A hydrogen atom consists of a nucleus containing a single proton and of a single electron orbiting the nucleus (Fig. 1.1). The proton having a positive charge and the electron a negative charge, the hydrogen atom as a whole is electrically neutral.

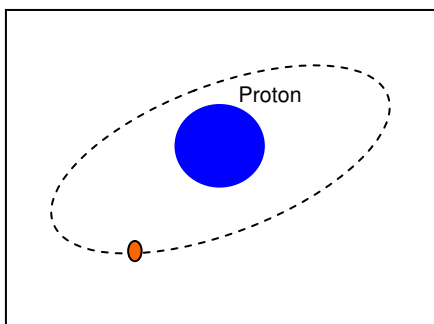


Figure 1.1: Schematic of a hydrogen atom.

Apart from its positive charge, the proton possesses a spin, an intrinsic property of nearly all the elementary particles. In the classical picture this means that the proton rotates about its axis like a spinning top [143, 201, 205]. The rotating mass results in a torque  $I$  and the rotating electrical charge results in a magnetic moment  $\mu$  (Fig. 1.2).

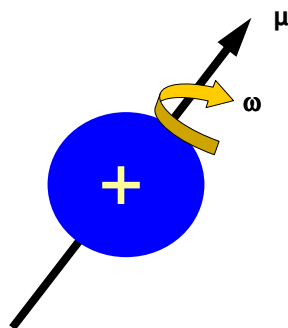


Figure 1.2: Classical description of the magnetic moment associated with proton.

External (electro) magnetic fields can interact with the magnetic moment as well as the moving magnetic moment can induce a current in an external coil (antenna) by the Faraday effect.

### 1.1.2 Spin in an external magnetic field

The spin is a quantum mechanical property, which can only have certain discrete values depending on the nucleus. Brought into an external magnetic field, each spin value represents an energy state of the nucleus (Zeeman Effect). Irradiation of the nucleus with electromagnetic waves of frequency  $\nu$  is given by

$$\nu = \gamma \cdot B_0 \quad (1.1)$$

with  $B_0$  being the strength of the external magnetic field and  $\gamma$  a nucleus specific constant (Fig. 1.3).

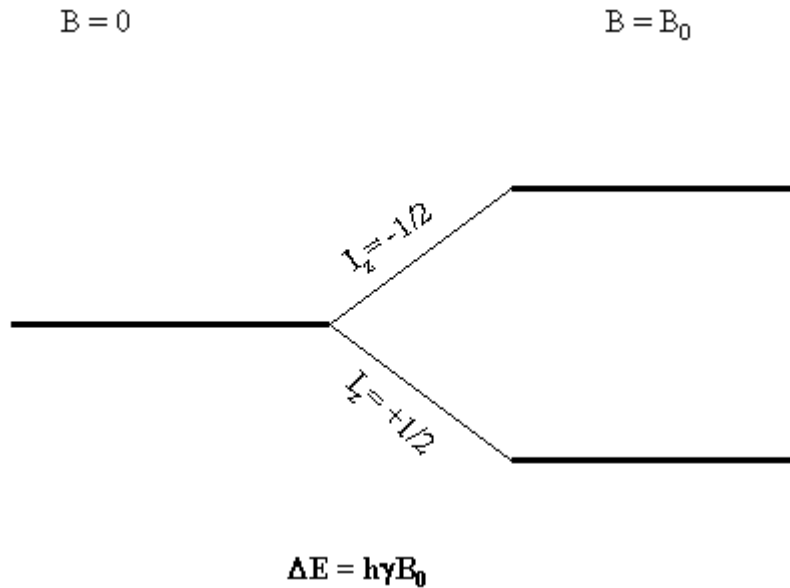


Figure 1.3: Split into two energy levels for  $I = 1/2$ .

The quantum mechanical properties of the spin can be considered in the classical picture by restricting the possible orientations of the magnetic moment of the spin to the direction of the main magnetic field  $B_0$  to  $m = 2I+1$  certain discrete values, with  $I$  being the quantum mechanical spin of the nucleus. For medical applications, the main target is the hydrogen atom (biological tissue consists to almost 65% of water, which causes a huge number of hydrogen



atoms), which possesses a spin of  $I = \frac{1}{2}$ . In the classical picture, in an external magnetic field the magnetic moment of  $I = \frac{1}{2}$  nucleus aligns either parallel (spin-up) or anti-parallel (spin down) at a distinct angle with the axis of the main magnetic field. The energy of the spin-up state is slightly lower than the spin-down state. Since a system always aims for the lowest possible energy state (thermodynamic equilibrium), at room temperature the spin-up state is higher populated than the spin-down state [28, 21, 49, 66, 74, 104, 157]. Similar to a gyroscope precessing around the axis of the gravitational field, the magnetic moment starts precessing around the axis of the external magnetic field with precession frequency, called the Larmor frequency and is given by

$$\omega_0 = \gamma \cdot B_0 \quad (1.2)$$

For hydrogen atoms, the gyromagnetic ratio  $\gamma$  and hence the dependency of the Larmor frequency on the main magnetic field results to  $\gamma_H = 42.6 \text{ MHz/T}$ , which results in Larmor frequencies between 21 MHz (0.5T), 63 MHz (1.5T) and 127 MHz (3T) on conventional clinical systems.

### 1.1.3 Population Distribution

The difference in population between the different states (spin up and spin down state) is defined by a Boltzmann distribution according to equation 1.3

$$\frac{N_{upper}}{N_{lower}} \sim e^{-\frac{\Delta E}{kT}} = e^{-\frac{h\gamma B_0}{kT}} \quad (1.3)$$

with  $k$  being the Boltzmann constant,  $T$  the temperature,  $h$  the Heisenberg constant, and  $\gamma$  the nucleus specific gyromagnetic ratio. From the equation it is clear that the difference depends on the strength of the external magnetic field.

### 1.1.4 Magnetization of a spin ensemble

To explain the signal formation from biological tissue, an ensemble from spins must be considered. As explained in the previous section, there are two populations of hydrogen nuclei: some high energy, spin down nuclei and a greater number of low energy, spin up hydrogen nuclei. The magnetic moments of all these nuclei precess around  $B_0$  at the Larmor frequency. As shown in Fig. 1.4 all the spins in certain energy states form a cone either in positive (spin-up) or negative (spin-down) z-axis. The macroscopic magnetic moment  $M$  results as the sum of all microscopic magnetic moments  $\mu_i$ .

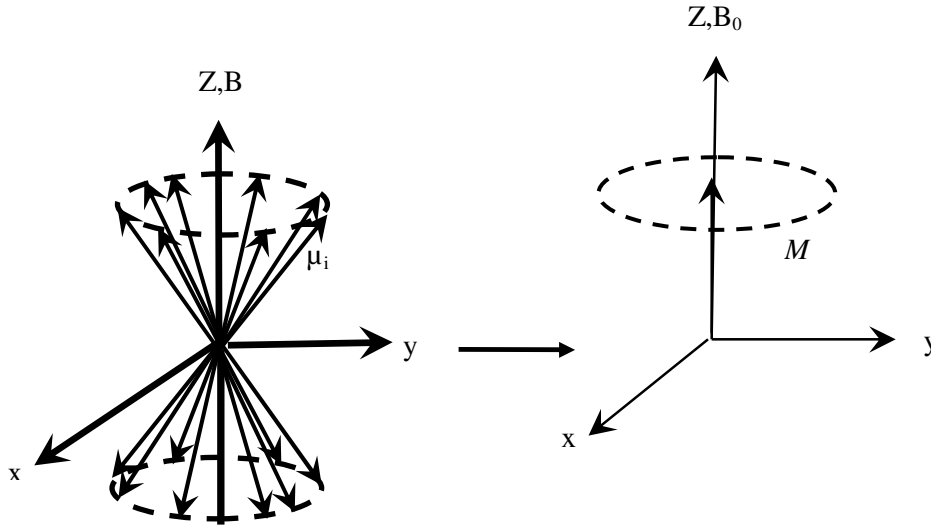


Figure 1.4: Formation of the macroscopic magnetic moment  $M$  from an ensemble of the microscopic magnet moments of the spins.

Since the xy-component of  $\mu_i$  is randomly distributed and the population of the low-energy (spin-up) state is higher than in the high-energy (spin-down) state  $M$  results as

$$M = M_o - \mu \frac{N_{lower}}{N_{upper}} \quad (1.4)$$

$M$  is a vector, with longitudinal component  $M_z$  and transversal component  $M_{xy}$ . Due to the random distribution of the transversal components of  $\mu_i$ , in the equilibrium state, the resulting transversal component of the macroscopic magnetic moment  $M_{xy}$  equals 0 and the longitudinal component  $M_z$  equals  $M_0$ . It can be shown that  $M$  behaves like a classical magnetic moment and that the behavior of  $M$  can be described by the classical Bloch equations [66, 113, 201].

### 1.1.5 Excitation of the spin system

Since in the equilibrium situation  $M$  is a static property, no electromagnetic signal is induced into an external antenna (coil) and no magnetic resonance (MR) signal is measured. To generate a detectable signal, a magnetic component in the  $xy$ -plane has to be generated, meaning that  $M$  has to be rotated toward the  $xy$ -plane, resulting in a non-zero  $M_{xy}$  component. Modification of  $M$  can be obtained by irradiation of the subject with electromagnetic waves (RF-pulse) at the Larmor frequency. Similar to conventional resonance phenomena, the precessing spins are synchronized and, hence energy is being deposit in the spin system, spins may be transferred from the low to the high-energy state. This causes the formation of a  $M_{xy}$  component (Fig. 1.5), which is rotating in the  $xy$  plane at Larmor frequency.

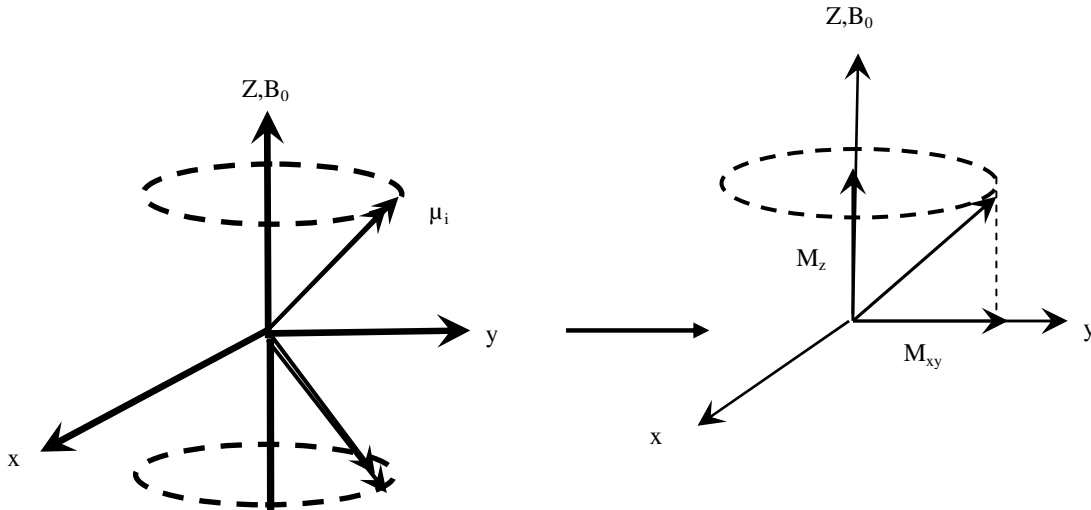


Figure 1.5: Formation of a detectable  $M_{xy}$  component by synchronization of the precessing spins and transfers of spins into the high energy state.

The rotating transversal magnetization induces an MR signal into the external coil. The process of generation of transversal magnetization is called excitation of the spin system. While irradiating the spin system,  $M$  is performing two rotations: (a) rotation around the  $z$  axis due to the precession of the spins, and (b) rotation orthogonal to the  $z$ -axis due to transition of spins to the higher energy level (excitation). The combination of the two rotations causes a spiral motion of  $M$  as shown in Fig. 1.6.

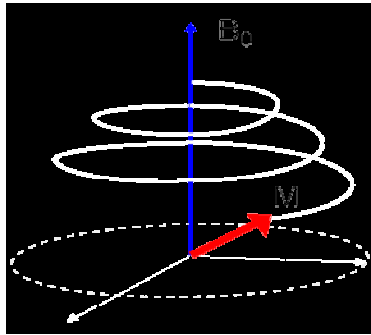


Figure 1.6: Spherical motion of  $M$  during excitation.

For simplification, MR signal can be described in a rotating frame coordinate system, in which the coordinate system rotates at the Larmor frequency. In this coordinate system,  $M$  is no longer rotating around the  $z$ -axis and the excitation can be described as a simple rotation around the  $y$ -axis. Depending on the length of the RF excitation pulse,  $M$  is rotating around a certain excitation angle  $\alpha$ . In principle,  $\alpha$  can be more or less be chosen arbitrarily. Typical values for the excitation range between  $10^\circ$  and  $90^\circ$  (depending on the acquisition technique). Special excitation angles are the  $90^\circ$ , in which the original magnetization  $M_0$  is completely being transferred to transversal magnetization and the  $180^\circ$  pulse, in which the magnetization is inverted [21, 79, 201].

## 1.2 Relaxation

After the excitation, the transversal component of the  $M$  (the projection of  $M$  onto the xy-plane) is rotating around the  $B_0$  axis, causing a RF signal in the receive coil. Over time, the signal is decreasing. The signal decay is caused by two concurrent processes: (a) spin-lattice relaxation ( $T_1$ -relaxation, longitudinal relaxation) and (b) the spin-spin relaxation ( $T_2$ -relaxation, transversal relaxation) [201].

### 1.2.1 Longitudinal relaxation

The longitudinal relaxation describes the return of the spin system to the thermal equilibrium state. After the excitation, the spin system is in an excited state. As in any system, the spin system falls back into the thermal equilibrium by transferring energy to its surroundings (the lattice). The transfer of energy causes spins to fall back to the lower energy state and hence cause the spin system to build up longitudinal magnetization until it finally approaches the thermal equilibrium state. The temporal behavior of the relaxation is described by an exponential function according to eq.1.5

$$M_z(t) = M_0(1 - e^{-t/T_1}) \quad (1.5)$$

with  $T_1$  being a tissue-specific constant describing the time required until 63% of the initial magnetization  $M_0$  is being reestablished after a  $90^\circ$  pulse (Fig. 1.7) [36, 79, 201].

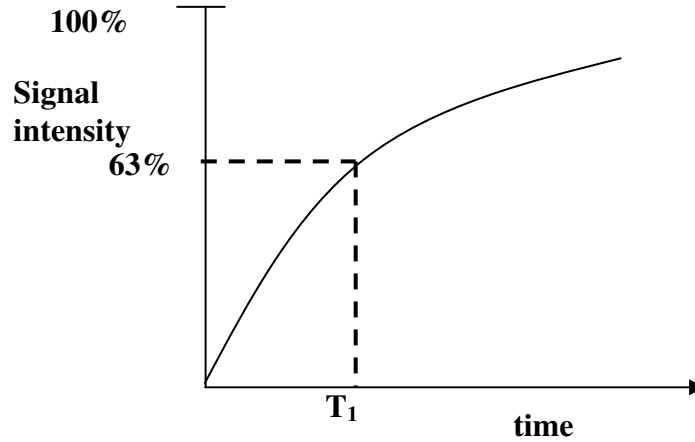


Figure 1.7:  $T_1$  recovery curve.

### 1.2.2 Transversal Relaxation

The transversal relaxation describes the decay of the MRI signal after the excitation. This decay of transverse signal occurs due to the loss of phase coherence between the spins. Directly after the excitation all the spins are perfectly in phase (directed into the same direction). This results into the maximal possible transversal magnetization. In an ideal system, the spins would remain in-phase and the loss of transversal magnetization would be caused by the spin-lattice relaxation only. In a real system, however, the transversal magnetization decays much faster, caused by (a) local magnetic field fluctuations and (b) local magnetic field distortions (inhomogeneities), which cause a loss of phase coherence and hence a reduction of the transversal magnetization (Fig. 1.8).

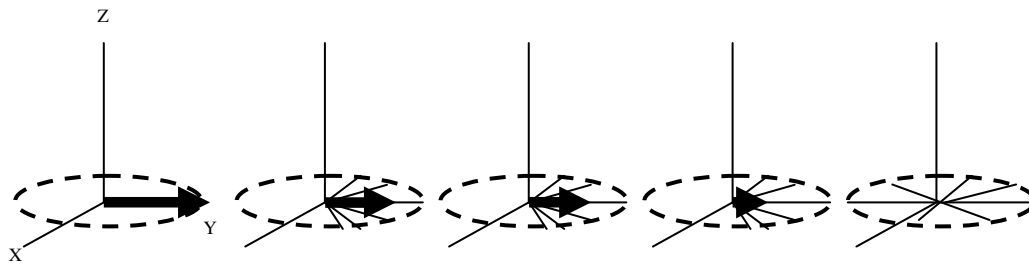


Figure 1.8: Decay of the transversal magnetization due to the loss of phase coherence of the spins.

### a) Local field fluctuations

The magnetic moment of each spin represents a tiny magnetic field (dipole field), which is superimposed to the main magnetic field  $B_0$ . Since the hydrogen atoms, and hence the related magnetic moments of the spins, are constantly moving, each spin is exposed to tiny rapidly fluctuating magnetic field changes caused by its neighboring spins. These fluctuating magnetic field distortions cause the spins to precess at locally fluctuating Larmor frequencies, which cause a loss of phase coherence. The transversal relaxation due to the fluctuating magnetic field is an exponential decay process (Fig. 1.9) and is described by the following equation

$$M_{xy}(t) = M_0 e^{-t/T_2} \quad (1.6)$$

$T_2$  in the above equation is the rate constant and is defined as the time required for the transverse component of  $M$  to decay to 37% of its initial value (Fig. 1.9).

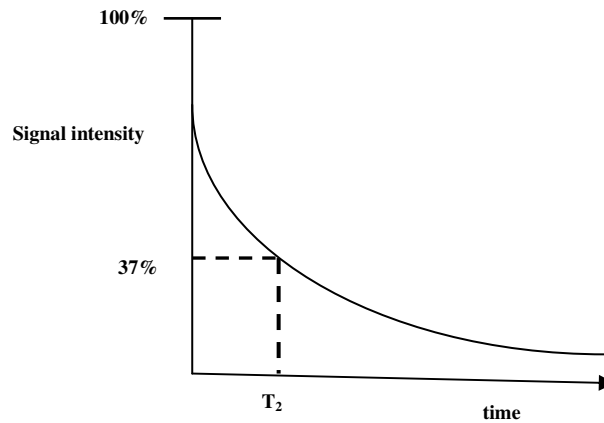


Figure 1.9:  $T_2$  relaxation curve. Exponential decay of  $M_{xy}$  with time constant  $T_2$ .

### (b) Static field distortion

Decent MRI systems provide magnetic fields with excellent field homogeneity with less than 1 ppm deviation within the imaging volume. Slight field distortions are compensated by static

shimming during the installation of the system. The remaining source of local field variation is the object under investigation, caused by the susceptibility differences of the different tissues. The susceptibility  $\chi$  of a given material refers to the tendency of a material to become magnetized in the presence of an external magnetic field. This alters the strength of the field both within the material itself and in its immediate neighbourhood [66, 143]. Mathematically it is represented as

$$M = \chi H \quad (1.7)$$

where,  $M$  is the internal magnetization,  $H$  is the intensity of external magnetic field and  $\chi$  is the susceptibility of a given material. Since  $\chi$  is a tissue property, whenever a sample contains tissues of different susceptibility, the strength of the magnetic field changes across their boundaries, causing spin dephasing e.g. between air and tissue and between bone (calcium) and tissue.

In contrast to the fluctuating field distortions introduced by the spin-spin interaction, the susceptibility introduced distortions are static. These static fields are superimposed and the combined effect yields an additional exponential signal decay, given by equation 1.8 with  $T_2^*$  being defined according to  $T_2$

$$M_{xy}(t) = M_0 e^{-t/T_2^*} \quad (1.8)$$

The relationship of  $T_2^*$  with the  $T_2$  from spin fluctuations and that from inhomogeneities of the magnetic field is given by the equation

$$1/T_2^* = 1/T_2 + 1/T_{2in homo} \quad (1.9)$$

where the term  $1/T_2$  is due to the random motion of spins and is not reversible, whereas  $1/T_{2in homo}$  is due to static field inhomogeneties and is reversible by a spin echo experiment [21, 27, 66, 119, 124, 157].



### 1.3 Spin Echo Experiment

A spin echo is formed by an excitation pulse of  $90^\circ$  followed by one or more refocusing pulses of  $180^\circ$ . The time between the two pulses is  $TE/2$  where  $TE$  is the echo time and is defined as the time between the RF excitation pulse and the center of the spin echo. The amplitude of the echo at  $TE$  is given by:

$$M_z = M_0 \exp^{-TE/T_2} \quad (1.10)$$

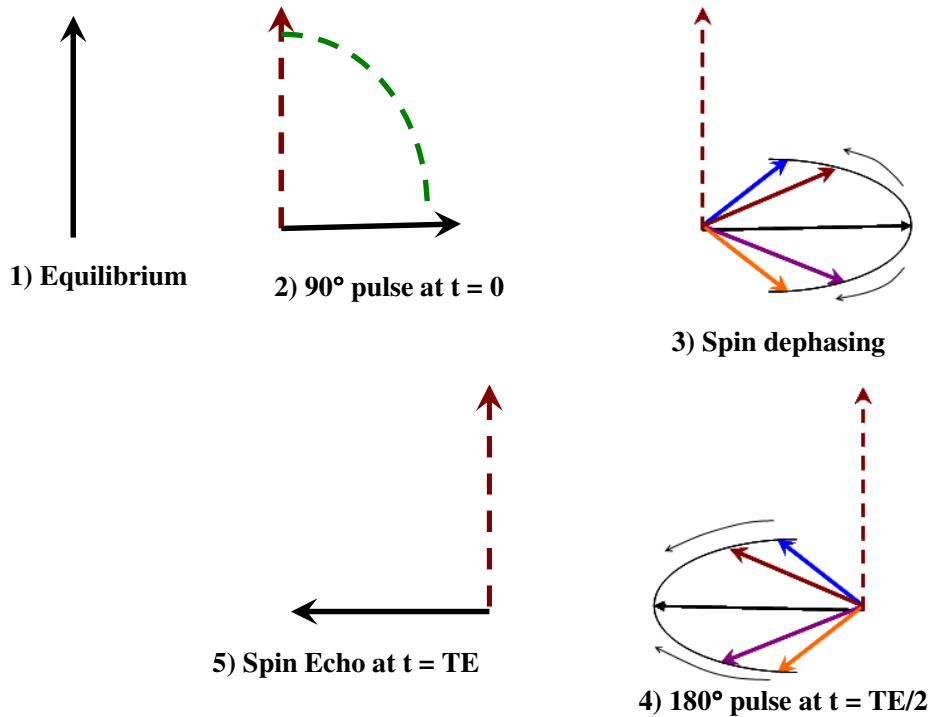


Figure 1.10: Principle of spin echo sequence.

The basic principle of spin echo formation is shown in Fig. 1.10. Initially the magnetization is in  $z$  direction. At time  $t = 0$  a  $90^\circ$  excitation pulse is applied, which flips the magnetization into the  $xy$  plane after which the transverse magnetization begins to dephase. Dephasing occurs because some spins precess faster than others as a result of the static magnetic field

inhomogeneities (please note that spin fluctuations are neglected here). Hence over time the spins accrue a magnetic field distortion  $\Delta B_0$  dependent phase  $\phi$  according to the equation 1.11.

$$\phi(t) = 2\pi\gamma\Delta B_0 t \quad (1.11)$$

The loss of phase coherence causes a reduction of the transversal magnetization. Then the  $180^\circ$  inversion pulse at  $t = TE/2$  causes a rotation of the spins around e.g. the x axis, which causes an inversion of the phase of the spins, yielding

$$\phi(TE/2) = -2\pi\gamma\Delta B_0 TE/2 \quad (1.12)$$

Thus those spins that were ahead before are now behind and vice versa. However, the spins that are now behind will catch up as they are still exposed to the same field inhomogeneities that caused the phase differences in the first place. Thus, after the second half of the TE interval has passed, all the spins are in phase. An echo is thus formed at time  $t = TE$ . The spin-echo principle relies on static magnetic field distortion. Thus only those components, which are static over time, can be compensated. Fluctuating contributions will still cause phase incoherence and the transversal magnetization will still decay with  $T_2$  instead of  $T_2^*$  [21, 66, 79, 201].

## 1.4 Contrast

Contrast in MRI arises due to intrinsic as well as due to extrinsic properties. The most important intrinsic factors are proton relaxations and the proton densities of the tissue. Extrinsic factors capable of influencing contrast include, the pulse sequence and pulse sequence parameters chosen. The extrinsic factors can be manipulated by the nature of the instrument, by varying the pulse sequences and/or parameters which is an advantage in MRI over the other imaging techniques. The intrinsic factors (proton relaxation rates and proton density) can be manipulated by administering external agents that can affect the proton

relaxation rate, called as contrast agents. The factors influencing the intrinsic contrast will be dealt here, whereas the role of contrast agents will be discussed in the section (1.7).

#### 1.4.1 Intrinsic contrast

The contrast in MRI is based on the signal difference between adjacent tissues. The contrast  $C$  between two tissues is defined as the ratio of the signal difference and the signal sum according to the equation 1.13

$$C = \frac{S_A - S_B}{S_A + S_B} \quad (1.13)$$

where  $S_A$  and  $S_B$  are signal intensities for tissue A and B. The signal in MRI is governed by the differences in the transversal and longitudinal relaxation properties of the tissues and, to a less significant part, the local spin density in the tissue.

Table 1.1: Relaxation constants ( $T_1$ ,  $T_2$ ) and relative proton density ( $PD$ ) for different human tissues.

Human tissue	$PD$ [%]	$T_1$ (ms)		$T_2$ (ms)	
		1.5T	3T	1.5T	3T
Myocardium	80	1030	1470	45	
Skeletal muscle	80	1000	1400	35	
Oxygenated blood (100% O <sub>2</sub> )	100	1450	1900	240	170
Deoxygenated blood (35% O <sub>2</sub> )	100	1450	1900	70	35
Fat	100	280	365	165	133
Kidney	81	700	1200	55	

From Table 1.1, it can be seen that the relative proton density does not substantially differ for the relevant soft tissues in the human body. Exceptions here are hard bone (calcium, higher proton density) and lung tissue (lower proton density). However, both tissues do not play a

major role in MRI since signal levels due to very short  $T_2$  (bone) and susceptibility (lung: air – tissue interface) are normally low.

The longitudinal relaxation property of the tissue is dependent on the main magnetic field strength.  $T_1$  values increase with field strength.  $T_2$  relaxation constants do normally less substantially depend on the main magnetic field strength. Dependency here is normally inverse proportional to the main magnetic field. The influence of the relaxation properties of the tissue on the resulting MRI signal can be controlled by adequate selection of the MR sequence parameters (Table 1.2). The important parameters here, are the repetition time (TR) and the echo time (TE).

Table 1.2: Resulting image contrast depending on the TR and TE.

Weighting	TE	TR
$T_1$ -weighted	Short	Short
$T_2$ -weighted	Long	Long
$PD$ -weighted	Short	Long

TR is defined as the time interval between subsequent excitations of the spin system. Within this time, the spins can rebuild longitudinal magnetization due to the spin-lattice (longitudinal) relaxation. A short TR causes a non-complete return of the spin system to thermal equilibrium (Fig. 1.11). At the point of the subsequent excitation, only a fraction of the longitudinal magnetization can be transferred to transversal magnetization. Hence the available transversal magnetization (which is used for image formation) is strongly dependent on the tissue  $T_1$  property (the available transversal magnetization is reciprocal proportional to the  $T_1$  constant of the tissue).

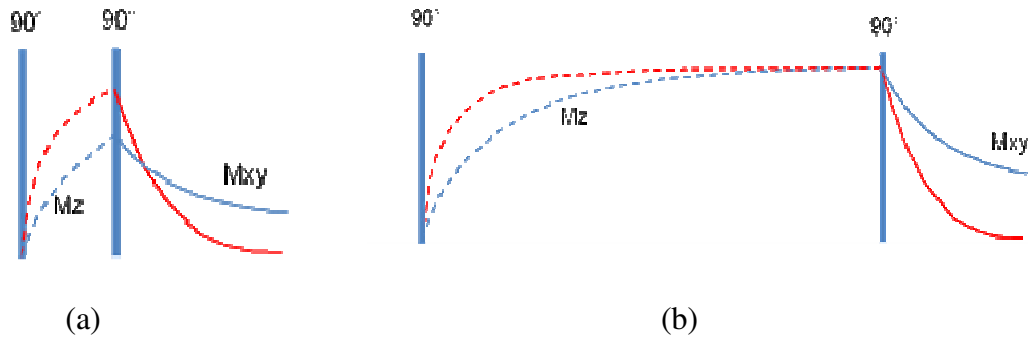


Figure 1.11: Available longitudinal magnetization in case of short TR (a) and long TR (b). Tissue with short  $T_1$  is denoted by red color and with long  $T_1$  is denoted by blue color.

A long TR ( $TR > 5 \cdot T_1$ ) causes an almost complete return of the spin system to thermal equilibrium. Hence the transversal magnetization generated during the subsequent excitation (and hence the MRI signal measured) does not depend on the tissue  $T_1$  value.

Superimposed to the dependency of the resulting MR signal on the repetition time, is its dependency on the echo time TE. TE is defined as the time between the actual excitation of the spin system and the time of the signal reception (more precise, TE is the time between excitation and coverage of the center of k-space). In this time period, the generated transversal magnetization decays due to the spin-spin interaction ( $T_2$ , spin-echo experiment) or the spin-spin interaction plus off-resonance induced dephasing ( $T_2^*$ , non spin-echo experiment). The resulting MR signal is still proportional to the chosen repetition time and the respective  $T_1$  weighting, but additionally weighted by the  $T_2$  and  $T_2^*$  decay. A short TE reduces the impact of the  $T_2$  and  $T_2^*$  relaxation on the final MR signal, a long TE can be used for increasing the impact of the  $T_2$  and  $T_2^*$  relaxation. Furthermore, the MRI signal is proportional to the local spin density  $\rho$  (or magnetization  $M_0$ ), which defines the maximal available magnetization of the tissue [66, 119, 143, 201]. The relationships between TR and TE and the resulting image contrast are summarized in Table 1.2. An overview of intrinsic contrast parameters of selected tissues is summarised in Table 1.3 [201].

Table 1.3: Signal intensity for different tissues

Tissue	$T_1$ -weighted	$T_2$ -weighted
Fat	High	High
Muscle	Low	Low
Fluid	Low	High
Fibrous tissue	Low/medium	Low
Air	No	No

## 1.5 Spatial encoding of the MR signal

With the current picture of the MR experiment, the origin of the MR signal is unknown. Assuming a perfectly homogeneous main magnetic field, after excitation each spin generates a signal  $S$  with constant frequency  $\omega_0$  and its location cannot be extracted from the MRI signal.

To resolve these ambiguities, the homogeneity of the static main magnetic field is disturbed by superposition of small switchable magnetic fields, the strength of which linearly scales with increasing distance to the iso-centre of the magnet. The linear magnetic fields are referred to as gradient fields or short gradients with abbreviation  $G$  (mT/m). Characteristic properties of the gradients include the gradient strength  $G_0$  (mT/m), describing the maximal amplitude of the respective gradient channel; its slew-rate  $dG/dt$  (mT/ms), describing the speed a certain gradient can be switch; and its linearity. To enable variation of the main magnetic field in all spatial directions, three orthogonally oriented gradients are used. Assuming a perfect linearity, the main magnetic field varies with the switched-on gradients according to:

$$\overline{B}(r) = B_0 + \overline{rG} = B_0 + xG_x + yG_y + zG_z \quad (1.14)$$

After excitation of the spin system, the received MRI signal  $S(t, r)$  at a certain location  $r$  is directly proportional to the local magnetization  $M_{xy}(t, r)$  and results to:

$$S(t, r) = M_{xy}(r)e^{i\gamma B(r)t} = M_{xy}(r)e^{i\gamma(B_0 + xG_x + yG_y + zG_z)t} = M_{xy}(r)e^{i\gamma(B_0 + \overline{Gr})t} \quad (1.15)$$

For calculation of the final MRI signal  $S(t)$ , all spins in the volume have to be considered, yielding:

$$S(t) = \int S(t, r)dr = \int M_{xy}(r)e^{i\gamma(B_0 + \overline{Gr})t}dr = e^{i\gamma B_0 t} \int M_{xy}(r)e^{i\gamma \overline{Gr}t}dr \quad (1.16)$$

With  $\overline{k} = \gamma \overline{Gr}$  and neglecting of the main magnetic field component,  $S(t)$  results as:

$$S(\overline{k}) = \int M_{xy}(r)e^{i\overline{k}r}dr \quad (1.17)$$

Eq.1.17 represents the Fourier-transformation  $S(\overline{k})$  of the spatial distribution of the transversal magnetization  $M_{xy}(r)$ . In MRI, the Fourier transform of the transversal magnetization is acquired in  $k$ -space. During the acquisition of a full MRI data set, sampling must comply with the Fourier transform properties [21, 66].

### 1.5.1 Fourier-transform properties

For imaging, the transversal magnetization must be discretized. Hence for MRI the properties of the discrete Fourier-transform DFT must be considered:

$$S(k_i) = \frac{1}{N} \sum_{n=0}^{N-1} M_{xy}(x_n) e^{-i2\pi x_n k_i / N} \quad (1.18)$$

To avoid aliasing in the reconstructed image, k-space data must be acquired over a certain range  $k_0$  at a certain resolution  $\Delta k$ , which depends on the chosen spatial resolution  $\Delta x$  and the respective field-of-view  $x_0$ .

### 1.5.2 k- Space encoding

Considering the direct relation of the position in k-space with the applied gradient fields (waveforms) according to  $\bar{k}(t) = \int \gamma \bar{G} dt$ , this may be expressed in a more general form

$$\bar{k}(t) = \int \gamma \bar{G}(t) dt \quad (1.19)$$

This implies that after the excitation of the spin system, the gradient fields have to be switched according to a function, which traverses the k-space dense enough and covers a sufficiently large volume according to Table 1.4 with simultaneous sampling of the MRI signal.

Table 1.4: Relation between k-space and x-space

	x-Space	k-Space
Coverage	$x_0$	$k_0 = 1/\Delta x$
Resolution	$\Delta x$	$\Delta k = 1/x_0$

In almost all MRI techniques, the k-space is not completely covered after a single excitation of the spin system. Main reason here is the resulting long acquisition time, which is required for full coverage of k-space. Due to the  $T_2$  and  $T_2^*$  signal decay, the MR signal will be completely gone after a few hundred ms. Therefore, in almost all MRI acquisition techniques, the acquisition of all k-space data is split up into subsequent acquisitions of segments of the k-space, each acquired after an independent excitation of the spin system. In almost all MRI techniques, k-space is covered on a rectangular grid. The acquisition is split up into a readout



phase, in which normally one line in k-space (aligned with the x-axis) and a phase encoding phase, in which the spin system is moved along the two remaining orthogonal axis.

### 1.5.3 Readout phase (frequency encoding)

The readout phase can be interpreted as a one dimensional MRI experiment (Fig. 1.12). Directly after the excitation, the spin system is in the center of k-space. Application of a negative gradient in x-direction drives the spin system along the  $k_x$ -axis into negative direction until it reaches the minimal required  $k_x$  value at  $t_1$ . By inverting the gradient sign, the spin system starts moving along the  $k_x$ -axis in positive direction. At  $t_2$ , the spin system is back to center of k-space. Continuation of the positive x-gradient enforces the spin system to continue moving along the positive direction until it reaches the maximal required  $k_x$ -value. The MRI signal is normally acquired from  $t_1$  to  $t_3$ . The negative part of the gradient is called pre-phasing gradient and the positive part is called the read out gradient.

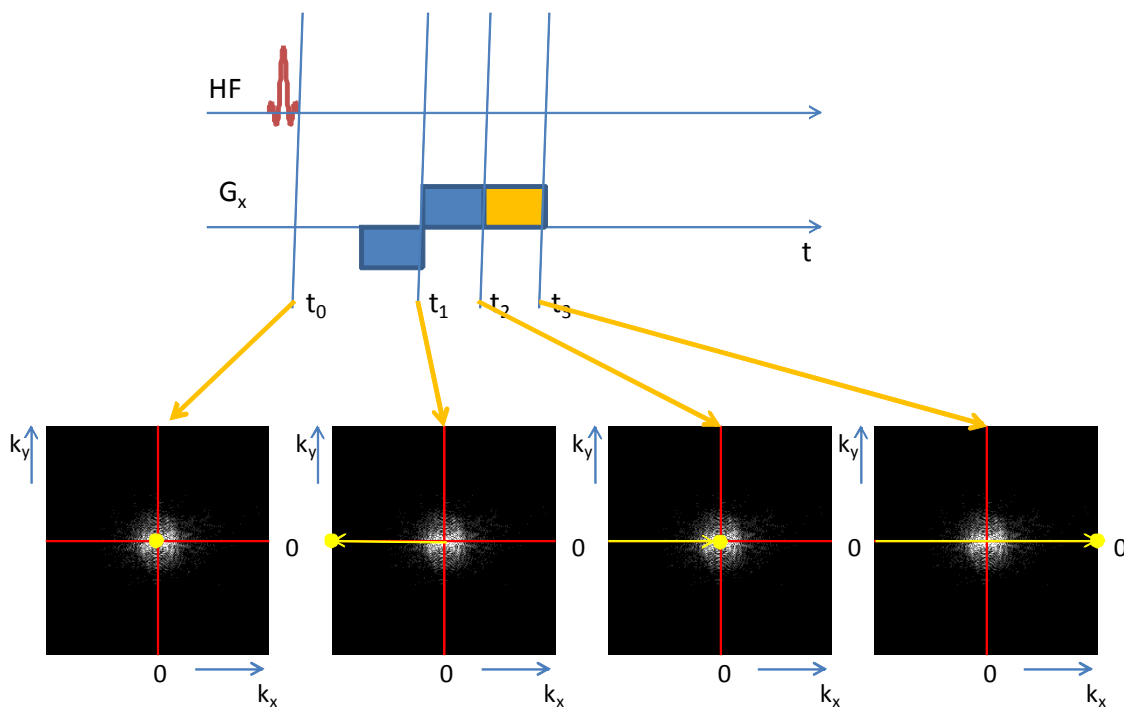


Figure 1.12: Principle of one readout experiment covering a single x-line in k-space.

### 1.5.4 Phase-encoding

For covering the entire k-space, the spin system has to be additionally moved along the y-direction (two-dimensional imaging) or the y- and z- direction (three-dimensional imaging). This is achieved by application of additional prephasing gradients in y- and z- direction (Fig. 1.13). Now, during the prephasing period, the spin system is additionally moved along the y- (2D) or y- and z- (3D) direction and during the readout period the MRI signal of a different line of k-space is acquired. By choosing different y- and z-gradient amplitudes, the spin system can be moved to different start points in k- space during the prephasing period.

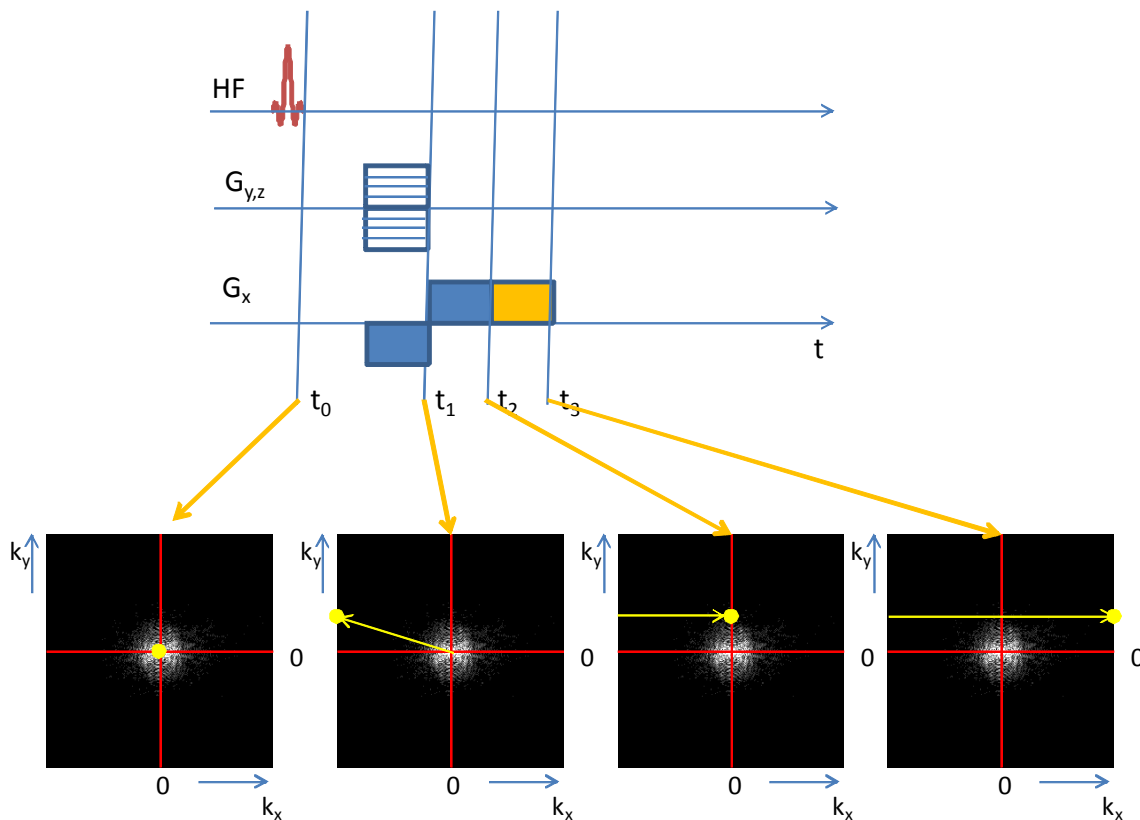


Figure 1.13: Principle of phase encoding.

For acquiring an MRI image with  $n_x \cdot n_y$  image pixel, in conventional imaging methods acquiring the MRI signal along a single line in k-space after each excitation,  $n_y$  excitations or

basic MRI readout experiments have to be performed. Extension to 3D imaging with  $n_x \cdot n_y \cdot n_z$  image voxel (voxel = 3D pixel) requires  $n_y \cdot n_z$  excitations of the spin system [21, 66].

## 1.6 MRI pulse sequences

As described earlier, each point of the k-space has to be covered during an MRI experiment. The different approaches and the resulting different switching of the respective gradient and RF waveforms called an MRI sequence. Different kinds of pulse sequence used in MRI are shown in Fig. 1.14.

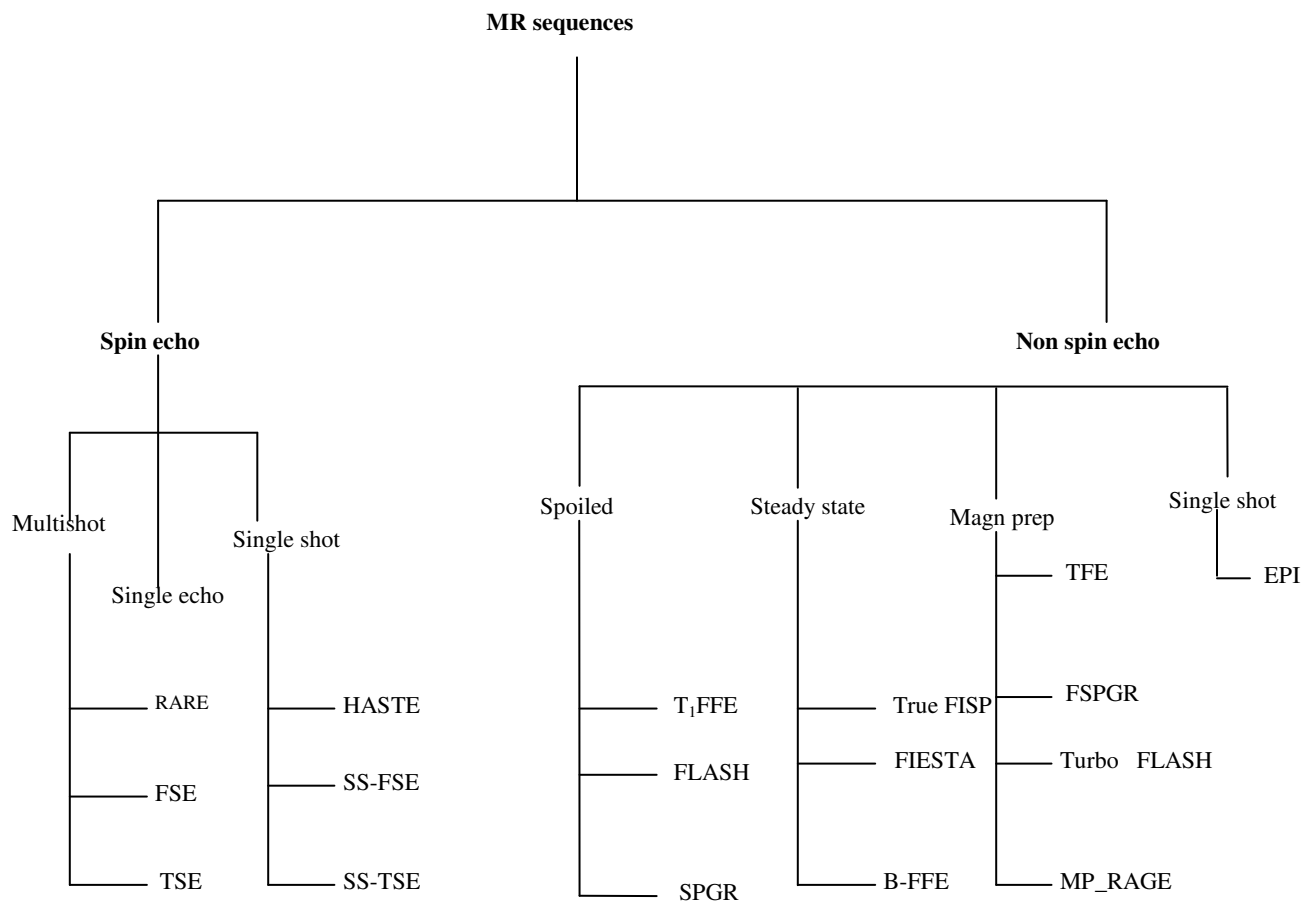


Figure 1.14: Different pulse sequences used in MRI.

Most MR sequences are based on one of the two following basic techniques.

### 1.6.1 Spin echo – based techniques (SE)

A spin echo based technique is based on a spin echo preparation before readout of the data. After excitation of the spin system (normally  $90^\circ$  excitation angle) at  $t = TE/2$  a  $180^\circ$  inversion pulse is applied and the timing of the sequence is such that the centre of k-space ( $k_x = 0$ ) is sampled at a more or less freely chosen echo time TE. For encoding of k-space, readout and phase encoding gradients are applied. It can be noticed here, since the inversion pulse represents a phase inversion in k-space, the dephasing and readout gradient have the same sign (Fig. 1.15 (a)). SE techniques are rather insensitive to off-resonances and normally provide excellent image quality with the compromise of long acquisition times. The rather long acquisition and repetition times cause SE-sequences to be quite motion sensitive.

### 1.6.2 Gradient echo (GE) based technique

Different from the spin echo techniques, in GE techniques the echo is not being generated by an inversion pulse, but by the readout gradient itself. For formation of the gradient echo, the spin system is first dephase (movement along the x-axis in negative direction) by applying a readout gradient with subsequent encoding of a single line of k-space (movement along the x-axis in positive direction). As mentioned earlier, an echo is formed ( $k_x = 0$ ) when the readout gradient compensates the effect of the dephasing gradient (Fig. 1.15 (b)). Since in a GE experiment, off-resonance induced phase shifts are not compensated, the signal decays with  $T_2^*$  instead of  $T_2$  as in the SE case. Since no inversion is required, GE techniques offer the potential for much shorter TE and TR, which may result in shorter image acquisition times. Due to the very short TR, the longitudinal magnetization can not sufficiently relax between subsequent excitation pulses. However, the frequent excitation of the spin system in short intervals causes the magnetization to approach a steady state after a certain number of excitations.

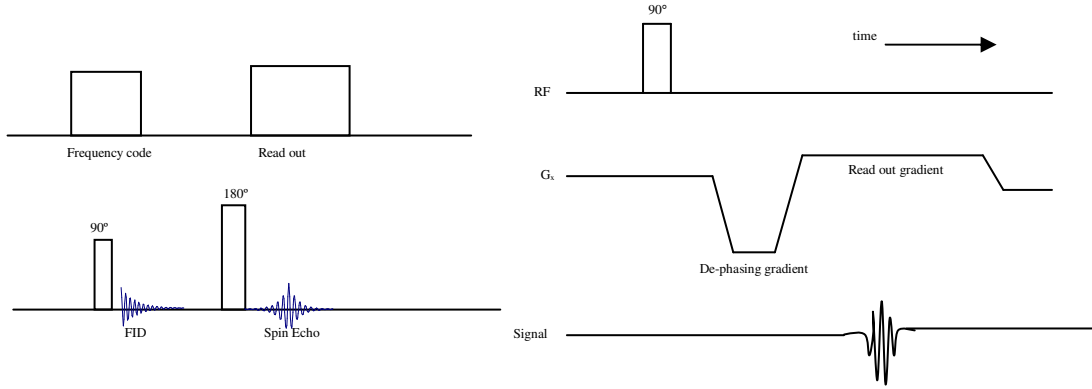


Figure 1.15: (a) Spin Echo (b) Gradient Echo sequence.

In a steady-state condition, the same amount of transversal magnetization is lost (by relaxation) as freshly generated (by excitation). Maximal steady-state signal is obtained with an excitation angle called as the Ernst angle and is given by:

$$\alpha_{opt} = a \cos \left( e^{-\frac{T_R}{T_1}} \right) \quad (1.20)$$

This Ernst angle is quite small (in the order of 10-20°) and hence the resulting transversal steady-state magnetization is only a fraction of the available magnetization, which in comparison with the SE techniques results in a substantially lower SNR. In case of short TR ( $TR < T_2$ ), the transversal magnetization cannot fully relax between subsequent excitation pulses. This causes magnetization to contribute to the MR signal over a variety of subsequent excitation cycles. The contributions of the residual transversal magnetization contain spin echo components (the RF pulses partly act like inversion pulses on the residual transversal magnetization) as well as gradient echo components originating from freshly excited spins. There are different gradient echo techniques known, which mainly differ by the way the residual transversal magnetization is treated [21, 66, 205].

### 1.6.2.1 Spoiled GE ( $T_1$ W-GE)

In the spoiled GE approach, the contribution of the residual transversal magnetization is cancelled out. This is achieved by applying a sufficiently huge dephasing gradient (so-called spoiler gradient) after the readout. Additionally or alternatively, subsequent excitation pulses and readouts are done with different RF phases, so that the residual signal is not in phase with the freshly generated magnetization. In spoiled GE, the signal is mainly formed from fresh magnetization, which, considering the short repetition time causes a strong  $T_1$  weighting of the residual images.

### 1.6.2.2 Spoiled GE ( $T_2$ W-GE)

Another form of the spoiled GE technique is  $T_2$ W-GE, in which, the strong spoiler gradient is applied prior to the readout period. This causes freshly generated magnetization to completely dephase before readout and hence not to contribute to the final acquired MR signal. Signal contributing to the actual measurement comprises only components, which has been generated several excitation pulses before (spin echoes). This approach yields a  $T_2$  weighting in the final image. However it is necessary that for the formation of the final echo, the magnetization has to remain in phase over the period of several excitation cycles. This property makes this technique extremely sensitive to all forms of motion. Furthermore, the signal to noise ratio of the sequence (freshly generated spins are dephase) is pretty poor. Therefore this technique is not very frequently used in clinical practice.

### 1.6.2.3 Steady-state-free-precision (SSFP)

In the SSFP approach, all spins are in-phase, meaning that all gradient and RF pulses are completely balanced (integral over all gradient waveforms and RF waveforms between two subsequent magnetic centers of the RF pulse equals zero). Since the residual transversal magnetization is kept in-sync, the residual signal results as a superposition of gradient- and spin echo components, which are either freshly generated by the most recent excitation pulse or generated during prior excitation pulses. Neglecting off-resonance effects, the SSFP

techniques generate a unique contrast, which depends on the fraction of the  $T_1$  and  $T_2$  tissue property.

### 1.6.3 Inversion Recovery (IR)

Inversion recovery (IR) sequence is basically a SE sequence with an additional  $180^\circ$  inversion pulse that precedes the usual  $90^\circ$  excitation pulse and  $180^\circ$  rephasing pulse (Fig. 1.16).

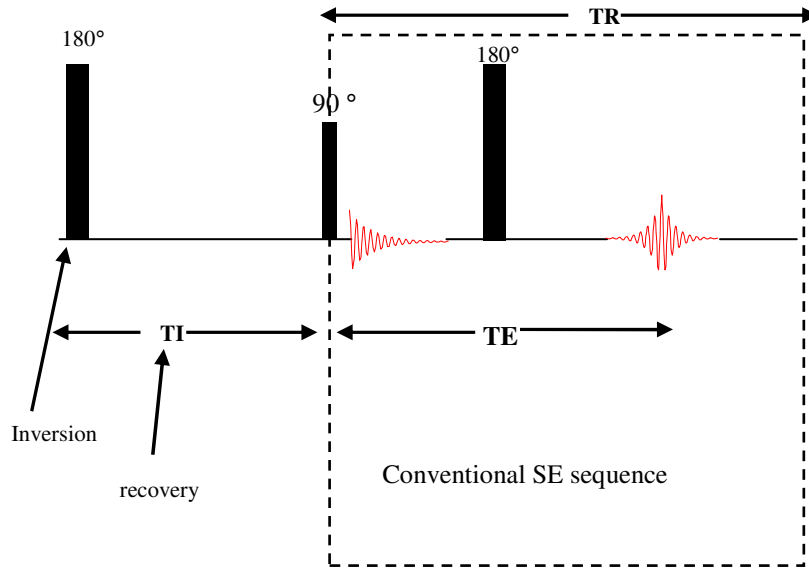


Figure 1.16: Basic Inversion Recovery Sequence.

An inversion pulse flips longitudinal magnetization from the positive  $z$ -direction into the negative  $z$ -direction. Following this pulse,  $T_1$  relaxation occurs in which the net magnetization from each tissue passes from an inverted condition through zero net magnetization to a relaxed condition. A user-definable inversion time ( $TI$ ) determines how much time is allowed for  $T_1$  relaxation. Subsequent excitation pulses are used to produce transverse magnetization for the resultant localization process. The signal intensity  $S$ , immediately preceding the  $90^\circ$  pulse is proportional to the  $M_z$  amplitude at time  $TI$  and is given by the equation

$$S(TI) = M_0 \left[ 1 - 2 \exp\left(-\frac{TI}{T_1}\right) \right] \quad (1.21)$$

where  $M_0$  is the equilibrium magnetization (proportional to the proton density) and  $T_1$  is the sample spin-lattice relaxation time.

Inversion-recovery images have considerable  $T_1$  weighting and provide excellent contrast control through choice of the TI. Fig. 1.17 shows the behavior of  $M_z$  as function of time, after a  $180^\circ$  pulse. The figure shows how  $M_z$  depends on the value of  $T_1$ . The time  $t = 0$  corresponds to the end of the  $180^\circ$  pulse, while the time  $t = \text{TI}$  is the instant at which the  $90^\circ$  pulse is applied. The three curves in Fig. 1.17 refer to three samples with different  $T_1$  times.

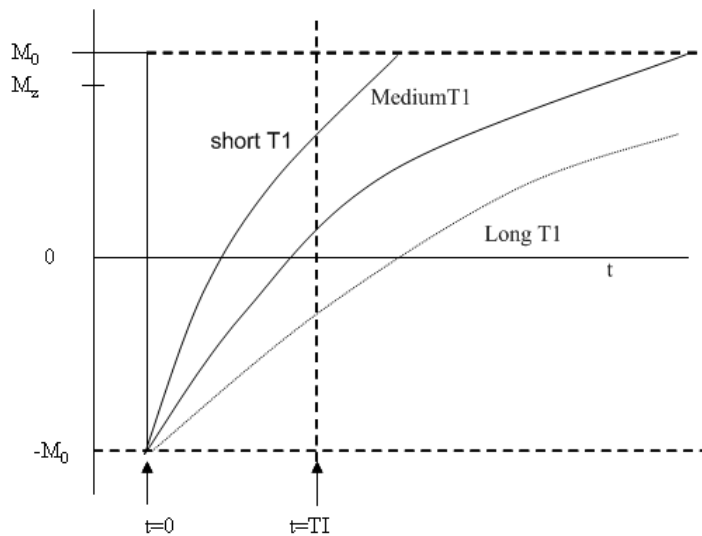


Figure 1.17:  $M_z$  as function of time in an IR sequence.

The major applications of inversion-recovery sequences are for suppression of tissue. Selecting a TI when a tissue is at zero net magnetization will cause the tissue to generate no signal. The TI time for this condition, known as the null point or null time for the tissue, is 0.692 times the  $T_1$  for the tissue to be suppressed, assuming TR is much longer than the tissue  $T_1$ .

One of the major limitations of inversion-recovery sequences is that they require a long TR. This is necessary so that the net magnetization is as close to full relaxation as possible prior to



the inversion pulse. The resultant long measurement times limit the usefulness of the technique for routine  $T_1$ -weighted imaging [21, 27, 66, 119, 201].

### 1.6.3.1 $T_1$ quantification by Inversion Recovery

Measurement of the  $T_1$  relaxation time is usually performed using inversion recovery sequences [65]. For  $T_1$  quantification the longitudinal magnetization is measured at different time intervals TI after an inversion pulse. Conventionally one data set with a given TI is acquired after each inversion pulse and the experiment is repeated after a sufficient long recovery period ( $>5 \cdot T_1$ ) with different TIs (single point method). This allows a different amount of  $T_1$  recovery to take place for each image before the magnetization is excited and the signal acquired. In this way, the recovery of longitudinal magnetization of a tissue is sampled with images acquired at multiple time points on the recovery curve. Standard curve-fitting techniques may be used to fit the signal intensity from each image versus TI in order to determine an average  $T_1$  either for a region of interest or for each pixel individually. This technique typically requires a total acquisition time of several minutes. For example to acquire a set of images with varying inversion times TI each  $256 \cdot 256$ -pixel image with a repetition time TR of 2.5 s will take  $256 \cdot 2.5$  s to acquire and a set of five points along the relaxation curve will therefore take about 53 min of imaging time [94]. Thus to overcome the problem of long imaging time modified sequence called Look -Locker was developed.

### 1.6.4 Look -Locker sequence

The Look -Locker sequence is a rapid imaging method used for the quantification of longitudinal relaxation times ( $T_1$ ). This sequence was originally proposed by D. C. Look and D. R. Locker [115]. A Look-Locker pulse sequence is a faster version of an inversion-recovery approach [27, 38, 65, 72, 94, 217]. In this pulse sequence, an inversion pulse inverts the longitudinal magnetization, but as the longitudinal magnetization recovers along the positive z-axis, small flip-angle pulses are used to create a small amount of transverse magnetization at multiple time-points along the  $T_1$  recovery curve. Gradient echo acquisitions are performed at

each of the time-points to sample the magnetization recovery. The sequence is shown in Fig. 1.18.

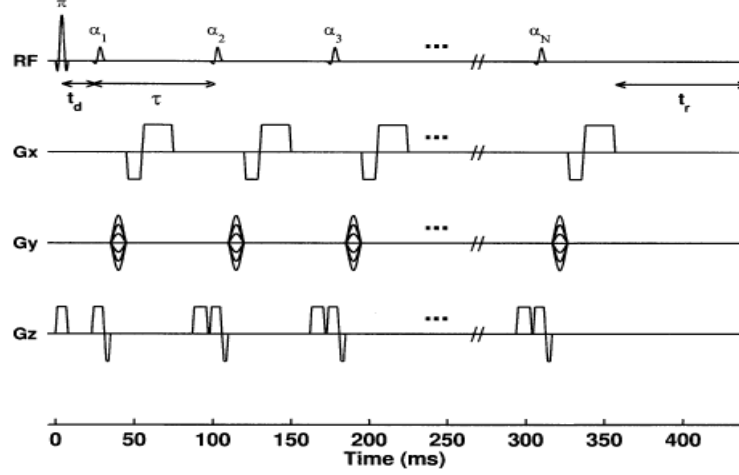


Figure 1.18: Schematic diagram of a conventional 2D Look-Locker pulse sequence [48].

As shown in Fig. 1.18, following an inversion pulse (for optimal dynamic range), the recovery of longitudinal magnetization to an equilibrium state is repeatedly sampled by a series of small flip-angle RF pulses ( $\alpha$ ) separated by a small time ( $\tau$ ). The recovery of the magnetization is modulated by the  $\alpha$  pulses, and therefore the magnetization is driven to equilibrium state with the modified relaxation time  $T_1^*$  where

$$T_1^* = \frac{T_1}{1 - \left[ \frac{T_1}{\tau} \right] \ln(\cos(\alpha))} \quad (1.22)$$

As shown in Fig. 1.18, the inversion-pulse/ $\alpha$ -pulse train is repeated for every ky phase encode step. For N  $\alpha$ -pulses, a series of N images are formed corresponding to times  $TI_n = t_d + (n-1)\tau$ , ( $n = 1, 2, \dots, N$ ) after the inversion pulse, where  $t_d$  is the time between the inversion pulse and the first  $\alpha$  pulse. A  $T_1$  map can be produced by fitting the  $T_1$  recovery curve of each pixel to a theoretical signal equation.

In this work, instead of the conventional gradient-echo (GE) readout, Look-Locker sequence with balanced steady-state free precession (b-SSFP) readout was used because of its higher signal-to-noise ratio (SNR) and lower tendency to modulate the relaxation curve [164]. Details of this approach can be seen in [41]. Advantages of using the Look-Locker pulse sequence is that imaging time to collect data for  $T_1$  estimates can be significantly reduced [94].

## 1.7 Contrast agents in MRI

Contrast is a term used to describe the relative difference between the signal intensity of two adjacent regions by using a color scale (normally a grey scale for MRI). For imaging modalities, such as conventional X-ray and CT, the image contrast is based on electron density difference that can be altered by the presence of a contrast agent (barium or iodinated complexes). Here, contrast is therefore directly related to the concentration of contrast agent in the tissue. For MRI, contrast is complex since the signal emitted by water protons is dependent upon both intrinsic and extrinsic factor. Intrinsic factors (proton relaxation rates and proton density) can be manipulated by administering external agents that can affect the proton relaxation rate, called contrast agents. These MR contrast agents are chemical compounds that work by enhancing the relaxation rate of protons in the tissue and thereby altering the signal intensity in the image relative to areas not affected by the contrast agent. They work as a catalyst that decreases the proton relaxation times ( $T_1$ ,  $T_2$  and  $T_2^*$ ) of tissue water. Thus it is the effect of contrast agent that is observed in contrast enhanced MR images and not the contrast agent itself. MRI contrast agents are classified into two broad groups depending on their effect on relaxation times (a) paramagnetic or  $T_1$  agents, which affect  $1/T_1$  more than  $1/T_2$  of tissue and (b) superparamagnetic or  $T_2$  agents, which affect the  $1/T_2$  of the tissue [160].

### 1.7.1 Paramagnetic or $T_1$ contrast agents

Paramagnetic agents contain water soluble metal ions with one or more unpaired electrons and thus possess high magnetic moment. Examples of paramagnetic metal ions are  $\text{Cu}^{2+}$ ,  $\text{Co}^{2+}$ ,  $\text{Co}^{3+}$ ,  $\text{Gd}^{3+}$ ,  $\text{Mn}^{2+}$ ,  $\text{Mn}^{3+}$ , and  $\text{Ni}^{3+}$ . Gadolinium ion is generally preferred in MRI contrast agents as it contains seven unpaired electrons and thus possesses a very high magnetic

moment ( $\mu^2 = 63 \text{ BM}^2$ ). Paramagnetic relaxation of water protons originates from dipole-dipole interactions between the nuclear spins of the hydrogen nuclei of water molecules and the fluctuating local magnetic field caused by the spins of unpaired electrons. The magnetic field of an electron is 657 times stronger than the magnetic field of a proton spin, and so if the magnetic field of electrons oscillates at or near the Larmor frequency, they will have a strong  $T_1$  effect. This is the case for the unpaired electrons in  $\text{Gd}^{3+}$ . The electron spin resonance of  $\text{Gd}^{3+}$  matches the Larmor frequency, inducing electron-nuclear dipolar interactions (exchange of spins), increasing the rate of transfer of energy to the lattice, which shortens the  $T_1$  relaxation time. The result is that the tissue signal near the contrast agent is much greater than for the neighboring tissue in a  $T_1$ -weighted image. Intravenous  $T_1$  contrast agents are available in both ionic and nonionic formulations. For *in vivo* applications, the gadolinium ions must be chemically bound to a ligand in order to reduce the toxicity and alter the pharmacokinetic properties of the metal [156]. The resultant gadolinium complexes are referred to as chelates, and the currently available gadolinium based chelates are known as extra cellular fluid (ECF) agents or extracellular contrast agents because they are distributed in the extracellular space. However, there are intravascular contrast agents also, which bind to the albumin and mainly remain in the blood-pool. Half-life time of extracellular contrast agents is usually in the order between 1 and 2 h and systemic clearance by the kidney is normally done after 24 h. Intravascular contrast agents remain in the blood stream for hours and systemic clearance can take up to 14 days. Currently, research is going on to make these contrast agents target specific, so that they can be used for specifically targeting of molecular markers and can act as indicators for local molecular processes. One of the strategies for this, involve the use of polymeric nanocapsules as vehicles to carry these contrast agents. The advantage of this approach is, the polymeric surface can be functionalized and they can carry a high load of the contrast agents at a particular site, generating high local field effect.

### 1.7.2 Superparamagnetic or $T_2$ contrast agents

Superparamagnetic substances are substances having very strong paramagnetic properties. They have very high magnetic moment that arises due to the arrangement of the paramagnetic ions in a rigid crystal lattice, which increases the mobility of their surrounding electrons (e.g.

iron oxide in the form of superparamagnetic nanoparticles). The commonly available superparamagnetic contrast agents are based on crystalline magnetite ( $\text{Fe}_3\text{O}_4$ ) or maghemite ( $\gamma\text{-Fe}_2\text{O}_3$ ), water insoluble iron oxide crystals [98, 168]. These crystals are often referred as nanoparticles, and each nanoparticle contains several thousand paramagnetic Fe ions ( $\text{Fe}^{2+}$  and  $\text{Fe}^{3+}$ ). Commonly, these contrast agents are used because of their significant capacity to produce predominantly  $T_2$  and  $T_2^*$  relaxation effects. These effects arise due to local field inhomogeneities caused by the high magnetic moment of these contrast agents, which accelerates dephasing of the protons beyond normal FID and thus shorten  $T_2$  and  $T_2^*$  further. This phenomenon is known as magnetic susceptibility (the tendency of a substance to become magnetized or to distort an applied magnetic field) and predominantly occurs in the presence of high local field strengths or at interfaces. This susceptibility may also cause artifacts. Magnetic susceptibility becomes manifest as a pronounced signal loss that is best appreciated on  $T_2$  and  $T_2^*$  weighted images. The agents producing a signal loss are therefore termed negative contrast agents [124,201].

Basically iron oxide nanoparticles are commonly sub-divided into two groups, depending on the overall size of the particles, particles with a total particle size of less than about 50 nm are referred to as ultra small particles of iron oxide (USPIO), where as particles with a total size in the range 50-200 nm are referred to as small particles of iron oxide (SPIO). Two compounds in the SPIO family are commercialized for intravenous use: ferumoxides (Endorem, Europe; Feridex, U.S. and Japan) and ferucarbotran (Resovist<sup>®</sup>, Europe and Japan). In both cases, the clinical targets are liver tumors. These nanoparticles are medium sized (70 to 150 nm) and coated with dextran (ferumoxides) or carboxydextran (ferucarbotran) [151]. Several USPIO particles have been investigated in humans such as ferumoxtran-10 (dextran) [37], VSOP (very small iron oxide particle; citrate), feruglose (pegylated starch) [182] and SHU555C (carboxydextran) [187]. Some USPIO nanoparticles have a similar composition to SPIO nanoparticles, but have a smaller total diameter. This avoids the self aggregation of SPIO particles due to magnetic attraction. Due to crystalline nature, superparamagnetic agents are particulate in nature [15].

## 1.8 Relaxivity

The efficiency by which a contrast agent changes the proton relaxation rate is termed as relaxivity of the agent [3, 126, 133, 215] and it is given by the following equation

$$1/T_{1,2} = 1/T_{1,2}^0 + r_{1,2} \cdot C \quad (1.23)$$

where  $T_{1,2}$  is the respective  $T_1$  or  $T_2$  proton relaxation time in the presence of contrast agent,  $T_{1,2}^0$  is the corresponding proton relaxation time in the absence of contrast agent, and  $C$  is the concentration of the contrast agent. The proportionality constant,  $r_{1,2}$  is called the relaxivity ( $r_1$  or  $r_2$ ) of the agent and the unit of relaxivity is  $\text{mM}^{-1} \cdot \text{s}^{-1}$  [138].

### 1.8.1 Theory for paramagnetic contrast agent induced relaxivity

Detailed theory about the relaxivity properties of paramagnetic contrast agents is given by the Solomon-Bloembergen equations [23,177]. These relaxivity properties arise due to three distinct types of contributions towards the water proton relaxivity i.e., inner sphere contribution, second sphere contribution and outer sphere contribution. Thus, the observed relaxivity can be represented as a sum of the contributions from three different factors as given by the following equation.

$$r_I = r_I^{IS} + r_I^{SS} + r_I^{OS} \quad (1.24)$$

Here, the term  $r_I^{IS}$ ,  $r_I^{SS}$  and  $r_I^{OS}$  correspond to the relaxivity contribution from inner sphere, second sphere and outer sphere water molecules respectively. The molecular parameters arising from these contributions are depicted in the Fig. 1.19 and explained in subsequent sections below.

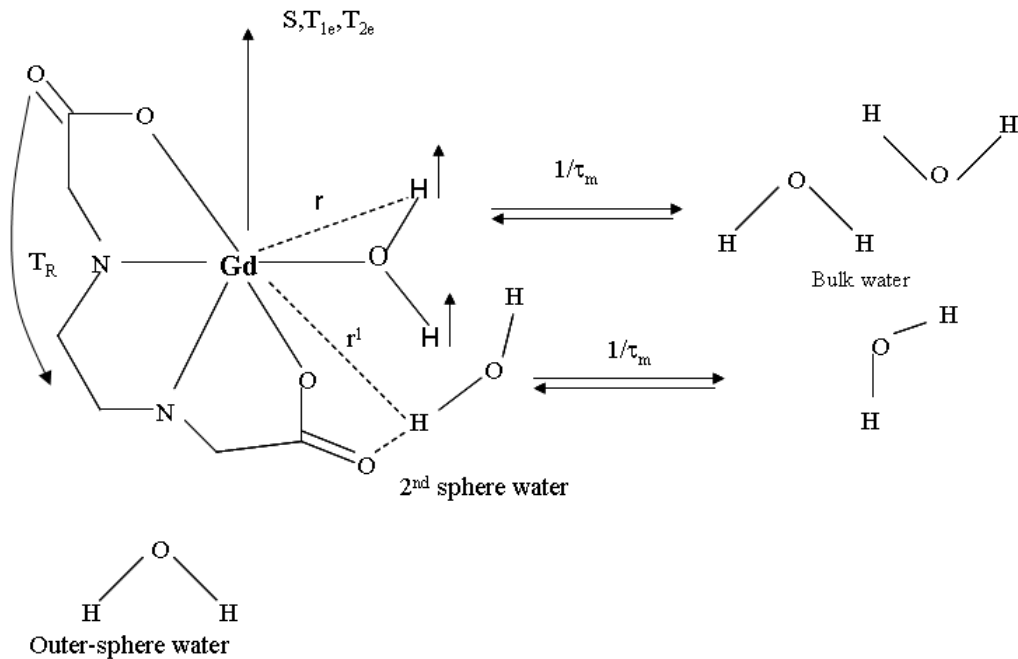


Figure 1.19: Schematic representation of the various types of water molecules surrounding the metal complexes together with the molecular parameters influencing the relaxivity [33].

### 1.8.1.1 Inner Sphere Contribution

This contribution arises from the inner sphere water molecules that are attached directly to the paramagnetic metal ion [111, 124]. These water protons relax efficiently and undergo rapid exchange with bulk water protons and contribute to the overall relaxation rate of the bulk water. The theory for the inner sphere relaxation was first developed by Solomon [177] and subsequently extended by Bloembergen and Morgan [23]. The contributing factors for the inner sphere relaxivities are given by the equation

$$r_1^{IS} = P_M q \left[ \frac{1}{T_{1m} + \tau_m} \right] \quad (1.25)$$

where,  $P_M$  is mole fraction of the metal ion,  $q$  is the number of water molecules bound per metal ion,  $T_{1m}$  is the relaxation time of the bound water protons (the reciprocal of  $T_{1m}$  i.e.  $1/T_{1m}$  is the longitudinal proton relaxation rate),  $\tau_m$  represents the residence lifetime of the bound

water (the reciprocal of  $\tau_m$  ( $1/\tau_m$ ) is the water exchange rate,  $k_{ex}$ ). Here,  $T_{lm}$  is the sum of dipolar (“through space”), and scalar or contact (“through bond”) contributions as represented by the following Solomon-Bloembergen equation [23,177]

$$\frac{1}{T_1 M} = \frac{2}{15} \left( \frac{\gamma_I^2 g^2 \mu_B^2}{r^6} \right) S(S+1) \left( 7 \frac{\tau_c}{1 + \omega_s^2 \tau_c^2} + \frac{3\tau_{cl}}{1 + \omega_I^2 \tau_c^2} \right) + \frac{2}{3} S(S+1) \left( \frac{A}{\hbar} \right)^2 \left[ \frac{\tau_e}{1 + \omega_s^2 \tau_c^2} \right] \quad (1.26)$$

where  $\gamma_I$  is the proton gyromagnetic ratio,  $g$  is the electron g-factor,  $\mu_B$  is the Bohr magneton,  $r$  is the proton-metal ion distance,  $\omega_s$  is the electron Larmor frequency,  $\omega_I$  is the nuclear Larmor frequency,  $S$  is the total spin of the metal ion,  $A/\hbar$  is the electron-nuclear hyperfine coupling constant. The dipolar and scalar relaxation mechanism are modulated by the correlation times  $\tau_c$  and  $\tau_e$  as given below [111].

$$\frac{1}{\tau_c} = \frac{1}{\tau_R} + \frac{1}{T_{le}} + \frac{1}{\tau_m} \quad (1.27)$$

$$\frac{1}{\tau_e} = \frac{1}{T_{le}} + \frac{1}{\tau_M} \quad (1.28)$$

where,  $\tau_m$  is the water residence time as mentioned above,  $\tau_R$  is the rotational tumbling time of the entire metal water,  $T_{le}$  is the longitudinal electron spin relaxation.

From the above equations, the parameters that directly affect the inner sphere and thus the overall relaxivity are  $q$ ,  $r$ ,  $\tau_m$ ,  $\tau_R$ , and  $T_{le}$ . These parameters can be fine tuned by altering the chemical environment around the paramagnetic metal ion [45]. Increasing the value of  $q$  increases the relaxivity. However, increase in value of  $q$  above 2 most likely makes the complex unstable [33, 95] and might increase the toxicity of the system. Decrease in the distance between  $Gd^{3+}$  and hydrogen ( $r$ ) will lead to an increase in relaxivity due to the closer



contact of proton with paramagnetic metal ion. Decreasing the term  $\tau_m$  will allow more water molecules to be affected by the gadolinium (III) ion resulting in an increase in relaxivity. If the value of  $\tau_m$  is decreased too much, the relaxivity of the complex will begin to decrease because the lifetime of the water molecules bound to the gadolinium (III) ion will not be long enough to influence the relaxation of the protons of the bulk water molecule [95]. By optimizing the value of  $\tau_R$  or  $T_{1e}$  the relaxivity of the contrast agent can be increased. There is an interdependence of the terms  $\tau_m$ ,  $\tau_R$  and  $T_{1e}$ . For most small molecule gadolinium (III) complexes,  $\tau_R$  is the limiting parameter among the three variables. As the value of  $\tau_R$  becomes optimized  $\tau_m$  and  $T_{1e}$  begin to influence the relaxivity of the contrast agents. In summary, to increase the relaxivity of a contrast agent, one has to design a ligand that will enable the complex to have a greater number of inner sphere water molecules,  $q$ ; optimally short water resident time,  $\tau_m$ ; and a slow tumbling rate,  $\tau_r$  while maintaining sufficient thermodynamic stability.

#### 1.8.1.2 Second Sphere Contribution

This contribution arises due to water molecules on the hydrophilic side of the complex (Fig. 1.19) or due the hydrogen bonded water molecules. The inner sphere relaxation theory can also be applied to this case if the lifetime of this interaction is long enough compared to the time required for the water molecule and the chelate to diffuse past each other [111].

#### 1.8.1.3 Outer Sphere Contribution

This is the contribution from the water molecules that are freely diffusing around the paramagnetic center, these water molecules are also termed as bulk water. The outer sphere contribution to the relaxation times incorporates the fluctuation due to electronic relaxation as well as due to translation diffusion [57]. Unlike inner sphere relaxation which involves chemical link between paramagnetic metal ion and water molecule, the outer sphere relaxation does not involve any chemical or electrostatic interaction between metal ion and water. The electron-nuclear dipolar interaction in this case is modulated due to translation diffusion of both species. The expression for outer relaxivity is given by the following equation

$$\left[ \frac{1}{T_1} \right]_{\text{outersphere}} = \frac{C\pi N_s \gamma_I^2 \gamma_s^2 \hbar^2 S(S+1)}{d^3 \tau_D} [7I(\omega_s, \tau_D, T_{1e}) + 3I(\omega_I, \tau_D, T_{1e})] \quad (1.29)$$

In the above equation, C is a numerical constant that differs slightly between the different models used to derive the equation,  $N_s$  is the number of metal ions per cubic centimeter, d is the distance of closest approach of the solvent molecule to the metal complex,  $\omega_s$  is the electron Larmor frequency,  $\omega_I$  is the nuclear Larmor frequency,  $T_{1e}$  is the longitudinal electron spin relaxation and  $\tau_D$ , the relative translation diffusion time [21]. The relative translation diffusion time,  $\tau_D$  is represented by the equation 1.30, where  $D_I$  and  $D_s$  are diffusion coefficients of water and metal complexes respectively.

$$\tau_d = \frac{d^2}{D_I + D_s} \quad (1.30)$$

Diffusion coefficients can be estimated if the motion is described by the diffusion of rigid spheres in a medium of viscosity  $\eta$  as shown in equation 1.31

$$D = kT / 6\pi a \eta \quad (1.31)$$

where, a is the molecular radius, k is the Boltzmann constant and T is the absolute temperature. The “7-term” and “3Term” spectral density function in equation 1.29 are mathematically complex terms in the Pfeifer [139] and Freed [57] versions of the equation. The other symbols in the equation 1.29 are the same as explained in section 1.8.1.1. For small-sized monoaquo  $\text{Gd}^{3+}$  complexes, the outer sphere contribution can account for 40-50% of the observed relaxivity, but for macromolecular systems this contribution is of less importance.

In summary, inner sphere theory accounts for the exchange between coordinated water molecules and bulk water, whereas outer sphere theory describes the relaxation induced by the diffusion of water molecules within the magnetic field gradients around the paramagnetic hydrated ion. The relaxation of current clinically approved agents is due to approximately 60%

inner sphere and 40% second and outer sphere effects [122]. For chelated ions, in the absence of water exchange, the outer sphere relaxation mechanism dominates.

### **1.8.2 Theory for superparamagnetic contrast agent induced relaxivity**

The theory describing the magnetic interaction of superparamagnetic compounds with water protons has been described by using different theoretical models in literature [155]. Exhaustive mathematical treatments of these models are beyond the scope of this thesis and can be referred in literature [155, 124]. A qualitative treatment of these theories is given here. One of the important models describing the above mentioned interaction is derived from classical outer-sphere paramagnetic relaxation model. In the classical outer-sphere theory, the dipolar interaction fluctuates due to the translational diffusion time of the water molecule and the Neel relaxation process. The short coming of this model is, it is relevant for a lower molecular weight iron complex such as ferritin and it does not describe the relaxation of iron oxide contrast agents because the equations do not take into account the curie contributions that modulate relaxation at high field, and the anisotropic energy that modulates the relaxation at low field. Then the outer sphere model has been modified to take into account the missing contributions by using Freed (low field fitting, characteristic correlation times  $\tau_D$  and  $\tau_N$ ) and an Ayant (high field fitting, characteristic correlation time  $\tau_D$ ) models of fitting weighted by magnetization of the sample (Langevin function) [124].

Till now, we have discussed the fundamentals of MRI, origin of contrast, factors affecting the relaxivity of contrast agents. One of the main aims of this thesis is to deliver commercially available contrast agents to a specific target. To have a better understanding of various commercially available contrast agents and their physico chemical properties, a table is given below with commercially available contrast agents and their important MRI related properties.

Table 1.5: Overview of most commonly used Gadolinium and Iron based contrast agents. Relaxivity values are provided for 1.5T and 3T [158].

Product	Active component	Effect of contrast agent	Relaxivity*		Relaxivity*	
			1.5T		3T	
			$r_1$	$r_2$	$r_1$	$r_2$
Gadovist®	Gadobutrol (Gd-DO3A-butriol)	Postive; $r_1$ enhanced	3.3	3.9	3.2	3.9
Magnevist®	Gadopentetate –Dimeglumine (Gd-DTPA)	Postive; $r_1$ enhanced	3.3	3.9	3.1	3.7
Multihance®	Gadobenate – Dimeglumine (Gd-BOPTA)	Postive; $r_1$ enhanced	4.0	4.3	4.0	4.7
Omniscan®	Gadodiamide (Gd-DTPA-BMA)	Postive; $r_1$ enhanced	3.3	3.6	3.2	3.8
Resovist® (SHU 555 A)	Ferucarbotran	Negative; $r_2^*$ enhanced	8.7	61	4.6	143
Feeridex / Endorem AMI- 25	Ferumoxide	Negative; $r_2^*$ enhanced	4.7	4.7	4.1	93
SHU 555 C	Ferucarbotran	Negative; $r_2^*$ enhanced	13.2	44	7.3	57

\* Values in  $\text{mM}^{-1} \cdot \text{s}^{-1}$

## Chapter 2

### Relevant Methods for Characterization

This chapter summarizes the basic principles of different types of instruments used in this work for the quantitative and qualitative analysis of contrast agent loaded nanocapsules and nanoparticles. Section 2.1 deals with the Dynamic Light Scattering (DLS) instrument, which was used for the size determination of the nanocapsules and nanoparticles, followed by section 2.2 which deals with Inductively Coupled Plasma – Optical Emission Spectroscopy (ICP-OES), used for the quantitative determination of metal ion concentration in the nanocapsules. Further Transmission Electron Microscopy (TEM) along with Scanning Transmission Electron Microscope (STEM), Energy Filtered Transmission Electron Microscopy (EFTEM) and Energy Dispersive X-ray Spectroscopy (EDS or EDX) were used to locate the position of the metal ions in the nanocapsules and particles. The basic principle and instrumentation details of these techniques are discussed in the section 2.3, 2.4, 2.5 & 2.6 respectively. Fourier Transform Infra Red spectroscopy (FT-IR) technique was used to prove the binding of functional groups present in the contrast agents to the polymeric shells. This is discussed in section 2.7. Magnetic Resonance Imaging (MRI) was used as the main analytical tool in this thesis. Principle and technical details of this technique are discussed in Chapter 1. However, details about the quantitative  $T_1$ ,  $T_2$  and  $T_2^*$  methods used for the analysis of nanoparticles are discussed in the section 2.8 and 2.9 respectively.

## 2.1 Dynamic Light Scattering

Dynamic light scattering (sometimes referred to as Photon correlation spectroscopy or Quasi-elastic light scattering) is a technique used for measuring the size of particles typically in the sub micron region. DLS measures Brownian motion and relates this to the size of the particles. Brownian motion is the random movement of particles due to the bombardment by the solvent molecules that surround them. Normally DLS is concerned with measurement of particles suspended within a liquid. If the particles or molecules are illuminated with a laser, the intensity of the scattered light fluctuates at a rate that is dependent upon the size of the particles as smaller particles are “kicked” further by the solvent molecules and move more rapidly. Analysis of these intensity fluctuations yields the velocity of Brownian motion (velocity of the Brownian motion is defined by a property known as the translational diffusion coefficient (usually given the symbol,  $D$ )) and hence the particle size using the Stokes-Einstein relationship.

$$d(H) = \frac{kT}{3\pi\eta D} \quad (1)$$

Where:-

$d(H)$  = hydrodynamic diameter (m)

$D$  = translational diffusion coefficient ( $\text{m}^2 \cdot \text{s}^{-1}$ )

$k$  = Boltzmann's constant ( $\text{m}^2 \cdot \text{kg} \cdot \text{s}^{-2} \cdot \text{K}^{-1}$ )

$T$  = absolute temperature (K)

$\eta$  = solvent viscosity ( $\text{kg} \cdot \text{s}^{-1} \cdot \text{m}^{-1}$ )

The diameter measured by DLS is a value that refers to how a particle diffuses within a fluid and hence referred as hydrodynamic diameter (Fig. 2.1). The diameter that is obtained by this technique is the diameter of a sphere that has the same translational diffusion coefficient as the particle. The translational diffusion coefficient will depend not only on the size of the particle “core”, but also on any surface structure, as well as the concentration and type of ions in the medium.

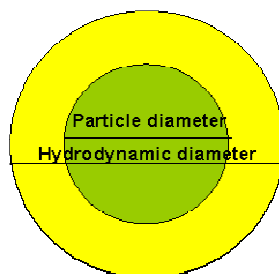


Figure 2.1: Particle diameter and hydrodynamic diameter.

A typical DLS system comprises of six main components as shown in the Fig. 2.2. High power monochromatic laser (1) acts as a light source to illuminate the particles in the sample. Major portion of the laser beam passes straight through the sample (2), but some of the light are scattered by the particles within the sample. A photodiode detector (3) is used to measure the intensity of the scattered light. In principle it is possible to detect the scattered light in all directions. For an accurate measurement of the scattered light, its intensity should be in a specific range and for this purpose an “attenuator” (4) is used that will adjust the intensity of the scattered light accordingly. The scattering signal of the detector is passed to a digital signal processing board called a correlator (5). The correlator compares the scattering intensity at successive time intervals to derive the rate at which the intensity is varying. This correlator information is then passed to a computer (6), where the software analyses the data and derive the particle size information.

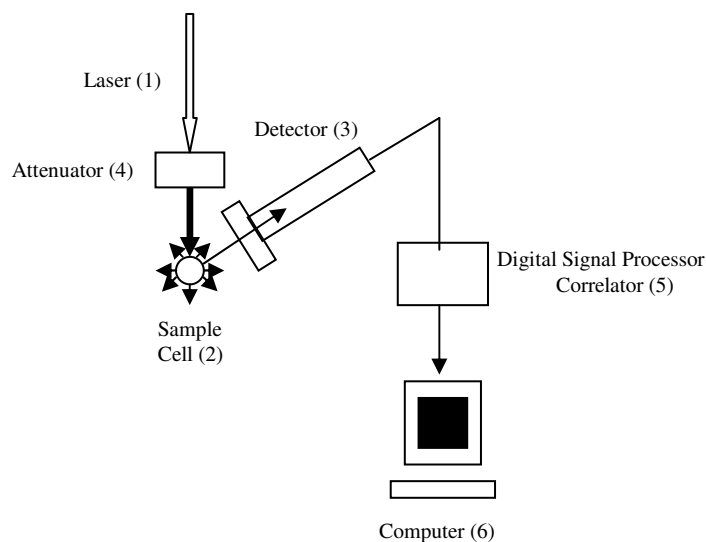


Figure 2.2: Schematic representation of a typical DLS system showing its six main components: (1) laser; (2) sample cell; (3) detector; (4) attenuator; (5) correlator; and (6) computer.

In dynamic light scattering, polydispersity or polydispersity index (PDI) is a very important width parameter. PDI is an index that describes the variation in particle sizes within the sample. It indicates the degree of distribution of the particle sizes and the deviation from the average particle size. Monodisperse particles have the same particle size; higher the PDI, wider is the width of the particle size distribution (PSD). We can have a PDI from 0 to 0.05 normally for standards that are made to be mono disperse. For a very good mono dispersity the value ranges from 0.05 to 0.08. If the value is between 0.08 and 0.7 the sample is considered to have mid range polydispersity. If the PDI is  $> 0.7$  it indicates that the sample has a very wide range of particle sizes [20, 214].

**Advantages:** Analysis by this technique is accurate, reliable and repeatable in one or two minutes. It is possible to do the measurement in native environment of the material. Sample preparation for this analysis is very simple or no sample preparation. Even high concentration or turbid samples can be used directly for analysis. The instrumental set up is simple and fully automated. Measurement of sizes  $< 1\text{nm}$  are possible. Size measurement of molecules with molecular weight  $< 1000$  Dalton can be done. For this analysis, very low volume of sample is required (as little as  $12\text{ }\mu\text{l}$ ).



**Limitations:** There is a lack of selectivity and relatively low signal strength making it difficult to study one component in a complex mixture of comparably sized molecules.

In the present work, the particle sizes of contrast agent loaded polymeric shell nanocapsules were determined using DLS.

## 2.2 Inductively Coupled Plasma –Optical Emission Spectroscopy

Inductively coupled plasma optical emission spectrometry (ICP-OES) is an analytical technique used to determine the concentrations of a wide range of elements in solution. In the present work we used this technique to determine the concentration of gadolinium and iron metal ions present in our contrast agent based samples. A schematic representation of a typical ICP-OES instrument is given in Fig. 2.3.

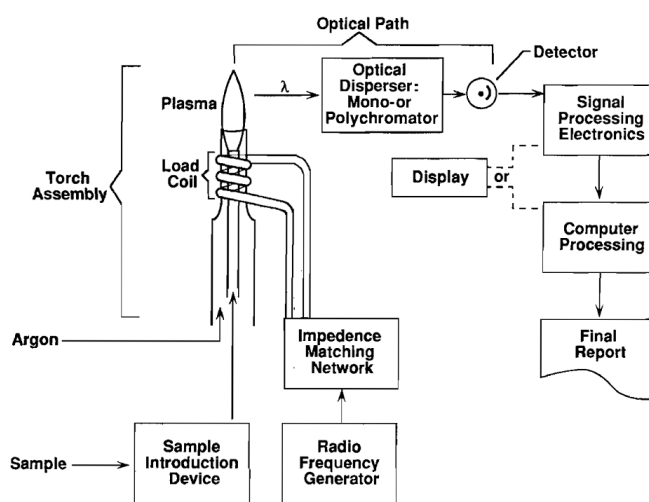


Figure 2.3: Block diagram of a typical inductively coupled plasma – optical emission spectrometer (ICP-OES) [169].

In this technique, the sample solution (in liquid form) is introduced into the core of inductively coupled argon plasma (ICP), which generates temperature of approximately 8000°C. At this temperature all elements become thermally excited and emit light at their characteristic

wavelengths. This light is collected by the spectrometer and passes through a diffraction grating that serves to resolve the light into a spectrum of its constituent wavelengths. Within the spectrometer, this diffracted light is then collected and amplified to yield an intensity measurement that can be converted to an elemental concentration by comparison with calibration standards. This technique is particularly suited for stoichiometry and material determinations. Samples for ICP analysis are prepared by various ways; if the sample is solid it will have to be dissolved in water. If the solid is insoluble in water, various methods can be used to solubilize the samples in water that include microwave digestion, high pressure fusion and acid digestion [82, 83, 169, 175].

**Advantages:** In ICP-OES, parallel and sequential analysis of multiple elements is possible and the instrumentation is suitable to automation, thus enhancing accuracy, precision. This instrument has a very high sensitivity (low limit of detection for majority of element is 10 ppb or lower).

**Limitations:** The emission spectra are complex and inter-element interferences are possible if the wavelength of the element of interest is very close to that of another element present in the same sample. The sample to be analyzed must be digested prior to analysis in order to dissolve the element(s) of interest.

In this thesis, metal ion concentrations were quantitatively determined using ICP-OES for the contrast agent loaded polymeric shell nanocapsules.

## 2.3 Transmission Electron Microscopy

TEM is used to examine objects that are as small as a single column of atoms, which is tens of thousands times smaller than the smallest object resolvable by a conventional microscope. Here in this study, we have used TEM for determining the sizes and morphological features of polymeric nanocapsules and contrast agent encapsulated polymeric nanocapsules. Using advanced TEM techniques (STEM, EFTEM) we have mapped the position of contrast agents inside the nanocapsules.

Transmission electron microscope (TEM) is a microscopic technique where electrons are used instead of light (as in conventional microscope) as source to image the target. Electrons are negatively charged particles incapable of passing through glass. Therefore, the lenses of an electron microscope are electromagnet and by varying the strength of these lenses, the magnification of the image formed can be changed.

Electrons are charged particles, and because collision with charged molecules in air will absorb and deflects electrons hence air distorts the electron beam. To avoid this problem, the optical system of an electron microscope must be evacuated. The electron source is produced by heating a tungsten filament at voltages usually ranging from 60,000 to 100,000 volts. The electromagnetic lenses then focus the electrons into a very thin beam. Typically a TEM consists of three types of lensing. These are condensor lenses, objective lenses, and projector lenses (Fig. 2.4). Condensor lenses are responsible for the primary beam formation, whilst the objective lenses focus the beam down onto the sample. The electron beam then travels through the sample. Depending on the density of the material present, some of the electrons are scattered and disappear from the beam. At the bottom of the microscope the unscattered electrons hit a fluorescent screen (because electrons are invisible to eye, the images they form are focused onto an imaging device), which gives rise to a "shadow image" of the specimen with its different parts displayed in varied darkness according to their density. The projector lenses are used to expand the beam onto the fluorescent screen or other imaging device, such as film. The image can be studied directly by the operator or photographed with charged coupled device (CCD) camera [82,169, 175, 210].

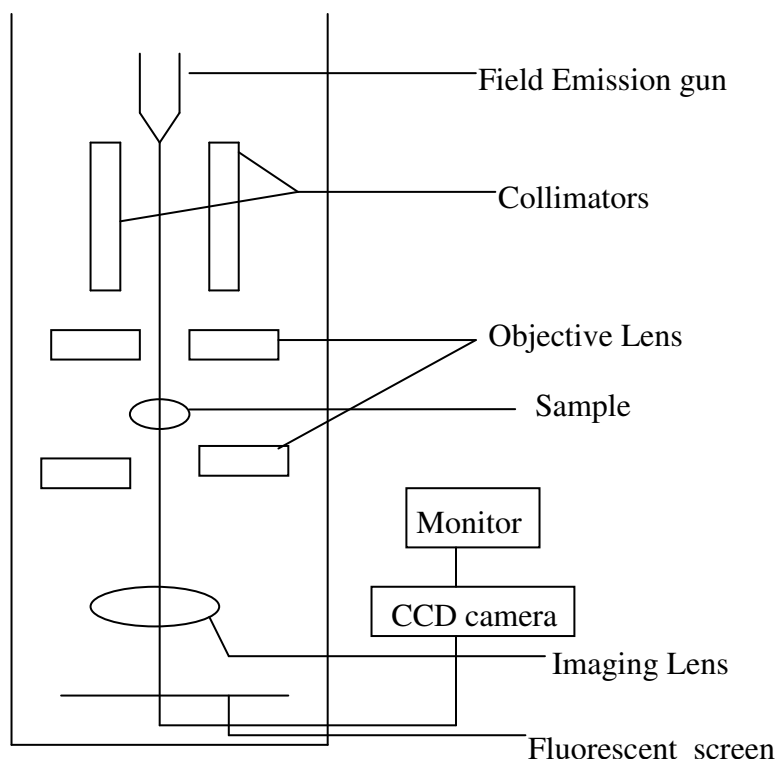


Figure 2.4: Block diagram of a typical transmission electron microscope.

**Advantages:** TEM has the capability of imaging material structures with atomic-size resolution. It has an outstanding image contrast and using TEM small area crystallographic analysis could be done.

**Limitations:** Major limitation of TEM analysis is that it takes significant sample preparation time. It is not possible to analyze materials that are not stable to electron beam. TEM analysis has a limited field of view, often less than 10 microns, so the sample for analysis may not be a representative of the bulk.

## 2.3 Scanning Transmission Electron Microscope

Scanning transmission electron microscope (STEM) is a special TEM-technique which essentially provides high resolution imaging of the inner microstructure and the surface of a thin sample (or small particles), as well as the possibility of chemical and structural characterization of micrometer and sub-micrometer domains through evaluation of the X-ray

spectra and the electron diffraction pattern. A STEM differs from TEM in the way that a TEM operates without scanning the electron beam, as in optical microscopy, while an STEM is based on a scanning beam, similar to scanning electron microscopy (SEM). In STEM technique, electrons pass through the sample, but, as in scanning electron microscopy, the electron optics focuses the beam into a narrow spot which is scanned over the sample. The scanning motion of the beam across the sample makes these microscopes suitable for various types of analyses and thereby obtaining valuable information from each analysis. The STEM can be operated in several modes including:

- (a) **Bright Field STEM:** Contrast in this mode is based on differences in average atomic number, differences in crystallinity and/or differences in crystallographic orientation. This technique utilizes the electrons that have not been scattered.
- (b) **Dark Field STEM:** This technique is sensitive to differences in average atomic numbers of the elements present in the sample. This technique utilizes inelastically scattered electrons for imaging [83, 209].

**Advantages:** This technique is used for nanoparticles characterization (for eg. core/shell investigations, agglomeration), ultra small area elemental maps.

**Limitations:** same as TEM (section 2.3).

In this study, STEM in bright field mode was used to locate the position of contrast agents ( $Gd^{3+}$  ions) inside the polymeric shell contrast agent loaded nanocapsules.

## 2.5 Energy Filtered Transmission Electron Microscopy

Energy Filtered Transmission electron microscopy (EFTEM) is a technique used in TEM analysis. It provides the distribution of the selected element on the image. When a high energy electron beam traverses a sample, different types of interactions occur between the incident electron and the electron in the sample material. Although most of the incident electrons pass

through the sample without getting scattered by the electrons in the sample, some electrons are scattered and these scattered electrons carry information about the sample. There are two types of scattering, (a) elastic scattering (no change in the energy before and after scattering) and (b) inelastic scattering (change in energy, the incident electron loses a fraction of its energy). For imaging purposes elastic part of the scattered electrons are needed as imaging with inelastic part results in blurred images and a decreased signal-to-noise ratio. Thus it is necessary to remove the inelastically scattered electrons from the images. To overcome this problem, energy filters have been used in TEM which can select the electrons that have lost a certain amount of energy in inelastic scattering processes. These electrons are used to create images with higher signal to noise ratio.

Since the energy-loss spectrum of a material contains signature of all the chemical species present, one can actually "tune in" to a certain element and obtain the two-dimensional distribution of that element in the specimen and select optimum image contrast. Energy shifts can be observed which are related to the chemical environment of the atoms, and hence bonding information may be derived from the fine structure of the energy-loss spectrum[207].

Here in this study, EFTEM was used to study the distribution of the  $\text{Gd}^{3+}$  present in the contrast agent loaded polymeric shell nanocapsules.

## **2.6 Energy Dispersive X-ray Spectroscopy**

Energy Dispersive X-ray Spectroscopy (EDS or EDX) is an analytical application that can be coupled with several techniques including SEM, TEM and STEM. EDX when combined with these imaging tools can provide elemental analysis or chemical characterization of a sample.

This technique involves the analysis of a sample through the interactions between electromagnetic radiation and matter, analyzing x-rays emitted by the matter in response to being hit with charged particles. Its characterization capabilities are due to the fundamental principle that each element has a unique atomic structure allowing x-rays that are characteristic of an element's atomic structure to be identified uniquely from each other. To

stimulate the emission of characteristic x-rays from a specimen, a high energy beam of charged particles such as electrons or protons or a beam of x-rays, is focused into the sample being studied. At rest, an atom within the sample contains ground state (or unexcited) electrons in discrete energy levels or electron shells bound to the nucleus. The incident beam may excite an electron in an inner shell, ejecting it from the shell while creating an electron hole in the original electron shell. An electron from an outer, higher-energy shell then fills the hole, and the difference in energy between the higher-energy shell and the lower energy shell may be released in the form of an x-ray. The number and energy of the x-rays emitted from a specimen can be measured by an energy dispersive spectrometer. As the energy of the x-rays is characteristic of the difference in energy between the two shells, and of the atomic structure of the element from which they were emitted, this allows the elemental composition of the specimen to be measured [82].

**Advantages:** This analysis is very quick, versatile; inexpensive.

**Limitations:** Size restrictions on samples; samples must be vacuum compatible (not ideal for organic material); limited sensitivity for elements with low atomic number.

## 2.7 Fourier Transform Infrared Spectroscopy

Fourier Transform Infrared Spectroscopy (FTIR) technique provides specific information about chemical bonding and molecular structures, making it useful for analyzing organic materials and certain inorganic materials. Chemical bonds vibrate at characteristic frequencies, and when exposed to infrared radiation, they absorb the radiation at frequencies that match their vibration modes. Measuring the radiation absorption as a function of frequency produces a spectrum that can be used to identify functional groups and compounds.

Infra red region of the electromagnetic spectrum extends from  $14,000\text{ cm}^{-1}$  to  $10\text{ cm}^{-1}$ . For chemical analysis, the mid infra-region ( $4,000\text{ cm}^{-1}$  to  $400\text{ cm}^{-1}$ ) is the region of most interest as it corresponds to the vibrational energy of most of the molecules. All molecules vibrate, even at a temperature of absolute zero. In general, a polyatomic molecule with  $N$  atoms has  $3N-6$  distinct vibrations. Each of these vibrations has an associated set of quantum states In IR

spectroscopy the IR radiation induces a jump from the ground (lowest) to the first excited quantum state. Not all possible vibrations within a molecule will result in an absorption band in the infra red region. To be infrared active, the vibration must result in a change of dipole moment during the vibration. This implies that vibrations in homonuclear diatomic molecules such as Hydrogen ( $H_2$ ), Nitrogen ( $N_2$ ) and Oxygen ( $O_2$ ) will not be IR active, as these molecules have zero dipole moment and these stretching will not result in any corresponding IR band in the spectra. In contrary, for heteronuclear diatomic molecules such as carbon monoxide (CO) and hydrogen chloride (HCl), which do possess a permanent dipole moment, infrared activity occurs because stretching of this bond leads to a change in dipole moment (dipole moment = charge  $\cdot$  distance). For interpretation of an IR spectrum it is necessary to refer to correlation tables of infrared data. There are many different tables available for reference [132].

A typical IR instrument contains a source for IR radiation, an interferometer, a sample chamber, detector and a computer to perform the Fourier transformation. There are a variety of techniques for sample preparation dependent on the physical form of the sample to be analysed. For solid there are two main methods for sample preparation involving the use of Nujol mull or potassium bromide disks. In case of liquid samples, a drop of the sample is placed between two potassium bromide or sodium chloride circular plates to produce a thin capillary film. The plates are then placed in a holder ready for analysis. To obtain an infrared spectrum of a gas requires the use of a cylindrical gas cell with windows at each end composed of an infrared inactive material such as KBr, NaCl or  $CaF_2$ . The cell usually has an inlet and outlet port with a tap to enable the cell to be easily filled with the gas to be analyzed [175].

**Advantages:** It is a quick and relatively cheap technique; useful in identifying many functional groups using their characteristic stretching frequencies. IR spectrum of a compound is unique and therefore it can be used as a fingerprint for this compound. IR analysis is non destructive and the samples can be recovered back.



**Limitations:** Limited surface sensitivity (typical sampling volumes are  $\sim 0.8 \mu\text{m}$ ); minimum analysis area:  $\sim 15$  micron. This technique has limited application in inorganic chemistry. This analysis is normally not quantitative (for quantitative analysis we need standards and calibration).

In the present work, this technique was used to characterize polymeric compounds using their specific absorption bands for specific functional groups in the monomer as well as in the polymer formed.

## 2.8 $T_1$ quantification using Look-Locker measurement

$T_1$  values were measured at 1.5T using a multi-image IR sequences (also known as a “Look-Locker” sequence [115], details of which are explained in chapter 1 (section 1.6.7). In brief the Look-Locker (LL) sequence consists of an initial inversion pulse followed by a train of pulses with constant, limited flip angle. The inversion pulse prepares the longitudinal magnetization, which from then on recovers exponentially according to  $T_1$  relaxation. The small flip angle pulses sample this build up. The resulting signal provides a set of measurements along the  $T_1$  decay curve, from which the  $T_1$  can be estimated using a least square procedure. Scheffler et al. [164] suggested the balanced-Steady State Free Precession (b-SSFP) sequence to read out the magnetization in the LL sequence. The recovery curve is apparently less perturbed by the readout pulses than in the fast low angel shot (FLASH) readout sequence, provided the sample does not have a short  $T_2$  since the image contrast is proportional to  $T_1/T_2$ .

In this work, b-SSFP look-locker sequence was used (Fig. 2.5). The time integrated area (over one TR between any two RF excitation pulses) of each gradient waveform in all gradient direction is zero. The name b-SSFP refers to this zero net area property and in such a way to balance the gradient waveform and RF pulses. A SSFP signal is generated with b-SSFP. Advantages of using b-SSFP readout are that it provides higher signal-to-noise ratio (SNR) and has less impact on the  $T_1$  relaxation curve [62, 185]. Data acquisition was performed with the following sequence parameter [1.5/12000/16° repetition time (ms) / echo time (ms) /flip angle (°)], spatial resolution of  $1 \text{ mm}^3$ , and temporal resolution of 30 ms.

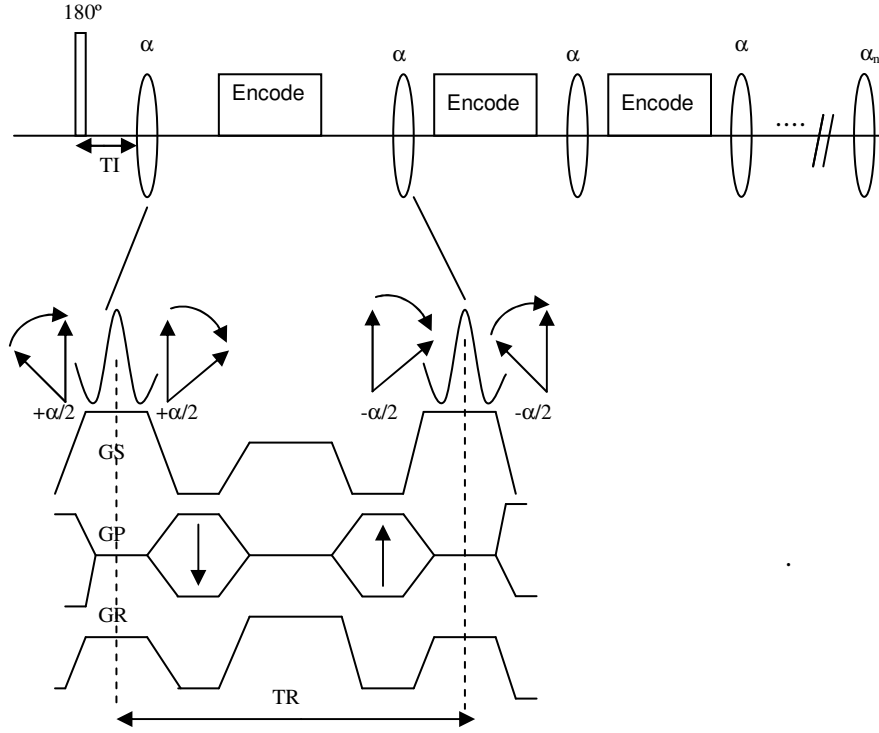


Figure 2.5: (A) b-SSFP Look Locker Sequence. The signed gradient areas of slice-select GS, phase-encoding GP, and read-gradient GR are zero within one TR. Due to the complete refocusing of transverse magnetization; the longitudinal magnetization oscillates between  $\pm \alpha/2$  around the z-axis [164].

$T_1$  values were calculated from the MR magnitude data of a region of interest (ROI) in the center of the sample by fitting of the data to a three parameter exponential function (2) applying a Levenberg-Marquardt optimization algorithm (Mat Lab, Math Works Inc.).

$$S(t) = \left| a - b \cdot e^{-t/T_1} \right| \quad (2)$$

## 2.9 $T_2$ and $T_2^*$ quantification by MRI

Basically  $T_2$  values are obtained from a set of images measured at different echo times. For  $T_2$  quantification multi spin-echo experiment is used with an echo train length of 8 and echo spacing of 10 and 15 ms. Each echo of the echo train is encoded with the same phase encoding gradient for a specific TR. The transverse magnetization was monitored by measuring the intensity of the echoes during the sequence. The entire decay curve was acquired during one echo train, which makes this measurement a very efficient one. The final  $T_2$  values were calculated by fitting a mono exponential function to the acquired data  $S(t)$ . All analyses were done based on the magnitude MRI data. Since in the magnitude data, noise will add a constant offset to the measured data [121], the model of exponential decay of the signal was extended by a constant offset term yielding

$$S(t) = S_0 e^{-t/T_2} + n \quad (3)$$

A pixel-by-pixel monoexponential fitting procedure is performed on the data set employing least squares minimization, and a value for  $T_2$  is calculated for each voxel over the region of interest.

$T_2^*$  weighted imaging and  $T_2^*$  mapping based on gradient echo sequences are widely used in many biomedical applications of MRI, such as functional MRI, evaluation of iron concentration in tissues, detection of organ lesions, and cell tracking [121]. However, one well-known problem associated with  $T_2^*$  weighted imaging and  $T_2^*$  mapping is that physiologically relevant or contrast agent induced changes in  $T_2^*$  weighted signal intensity are masked by signal losses caused by macroscopic field inhomogeneity [121], which may originate from magnet imperfections, poor shimming, tissue–air interfaces, etc. As a result,  $T_2^*$  quantification by conventional gradient-echo imaging methods are generally thought to be useful only when macroscopic field inhomogeneity is negligible [69]. In the present work the  $T_2^*$  quantification is obtained by using gradient echo sequence. 16 gradient echoes with echo spacing between 3 and 7 ms were used to acquire the values. The final  $T_2^*$  values were

calculated by fitting a mono exponential function to the acquired data  $S(t)$ . All analysis was done based on the magnitude MRI data. Since in the magnitude data, noise will add a constant offset to the measured data, the model of exponential decay of the signal was extended by a constant offset term [69] yielding

$$S(t) = S_0 e^{-\frac{t}{T_2^*}} + n \quad (4)$$

However these measured values also suffered from the superimposed magnetic field distortions  $\Delta B_0$ , causing a more rapid decay of the MRI signal  $S(t)$ , resulting into underestimation of the resulting  $T_2^*$  values. For reduction of the impact of the superimposed  $B_0$  variation, the following model (developed by Prof. Dr. rer. nat. Volker Rasche, University Hospital Ulm) was used to correct all the measured values acquired by using gradient echo sequence. Details of the model is given in the Section I

### Section I

**Author:** Prof. Dr. rer. nat. Volker Rasche, Department of internal medicine II, University Hospital Ulm, Germany

$$S(t) = S(t) e^{-t/T_{2,I}} e^{-t/T_{2,\Delta B0}} = S(t) e^{-\left(t/T_{2,I}^* + t/T_{2,\Delta B0}^*\right)} = S(t) e^{-t(R_{2,I}^* + R_{2,\Delta B0}^*)} \quad (5)$$

According to the model, the measured value in the  $T_2^*$  map can be interpreted as:

$$R_2^* = \frac{1}{T_2^*} = R_{2,I}^* + R_{2,\Delta B0}^* \quad (6)$$

Knowledge of  $R_{2,\Delta B0}^*$  enables calculation of the iron-induced contribution to the measured  $T_2^*$  value  $T_{2,I}^*$  according to

$$T_{2,I}^* = \frac{1}{R_{2,I}^*} = \frac{1}{R_{2,I}^* - R_{2,\Delta B0}^*} \quad (7)$$

For a course estimation of the local values, the resulting  $T_2^*$  value in the surrounding agarose gel is compared to the expected value  $T_{2, ref}^*$ , which is defined as the maximal  $T_2^*$  value over the phantom.  $R_{2, \Delta B0}^*$  for the agarose gel is calculated according to Eq. 6 and used for local off-resonance correction according to Eq. 7.

## Chapter 3

### Characterization of MRI contrast agent loaded polymeric nanocapsules as versatile vehicle for targeted imaging

#### Part A– An inverse miniemulsion approach

Magnetic resonance imaging (MRI) has evolved as a prominent imaging technique in diagnostic clinical medicine and biomedical research due to its non-invasiveness, excellent contrast resolution, and good (submillimeter) spatial resolution [25, 33]. Signal in MRI is dependent on the local relaxation properties and densities of the nucleus under investigation. For proton imaging, the resultant image contrast is governed by the differences in longitudinal ( $T_1$ ) and transversal ( $T_2$ ) relaxation properties of protons [88, 127]. The relaxation properties of tissues can be altered by the administration of contrast agents prior to scanning [204]. These contrast agents are defined as chemical compounds that are capable of markedly altering the local relaxation properties of the water protons in tissue. The efficiency of a contrast agent to change the relaxation rate is represented quantitatively as relaxivity, with  $r_1$  being the relaxivity corresponding to  $T_1$  relaxation or longitudinal relaxation (defined as the time required to build up 63% of the longitudinal magnetization) and  $r_2$  being the relaxivity corresponding to the  $T_2$  relaxation or transverse relaxation (defined as the time after which 37% of the initial transversal magnetization is lost) [111, 126]. Relaxivities are usually expressed in  $\text{mM}^{-1}\cdot\text{s}^{-1}$  [114]. Recent contrast agents are based on complexes of paramagnetic and superparamagnetic metal ions such as complexes of  $\text{Fe}^{3+}$ ,  $\text{Gd}^{3+}$ , and  $\text{Mn}^{2+}$ , which show high magnetic moments and thus a high relaxation efficiency [22].

In general, there are two classes of MR contrast agents. Positive contrast agents, which predominantly cause shortening of the  $T_1$  relaxation and negative contrast agents, which predominantly cause shortening of the  $T_2$  relaxation. Positive contrast agents are usually comprised of paramagnetic gadolinium ( $\text{Gd}^{3+}$ ) complexes. These contrast agents increase the rate of energy exchange between the nuclear spin system and the environment and hence reduce  $T_1$ . These contrast agents generate a signal enhancement on  $T_1$ -weighted MRI images. Negative contrast agents are usually based on superparamagnetic components, which increase local dephasing of the spins due to the introduced field perturbations. The increased dephasing causes a signal decrease on  $T_2$  and  $T_2^*$  weighted images. Examples here are superparamagnetic iron oxide particles (SPIOs) and ultra small SPIOs (USPIOs) [4, 188].

Although MRI has good spatial resolution, it suffers from its rather low sensitivity in detection of low-concentrations of local contrast agent's aggregations as in the case of targeted contrast agent imaging. Since for this application the limiting factor is the number of local receptor sites, the relaxivity per binding site of a certain contrast agent must be optimized. This can either be achieved by optimization of the relaxivity of the compound or by increasing the contrast agent load per binding site.

The relaxivity of paramagnetic complexes mainly depends on the water exchange between bulk water and water bound to the chelated  $\text{Gd}^{3+}$  and on the rotational correlation time of the  $\text{Gd}^{3+}$  ions [32]. The rotational correlation time can be increased by conjugating the  $\text{Gd}^{3+}$  chelates to macromolecular objects like dendrimers [29, 206], liposomes [192], micelles [189], and nanoparticles [125].

Several approaches for increasing the local contrast agent load per potential binding site have been introduced. Turner et al. [189] used gadolinium-labeled-shell cross-linked nanoparticles (40 nm diameter) which resulted into  $r_1$  of  $39 \text{ mM}^{-1} \cdot \text{s}^{-1}$  per  $\text{Gd}^{3+}$  ion (0.47T) and possess 510  $\text{Gd}^{3+}$  ion per particle, which resulted in  $r_1$  of  $2 \cdot 10^4 \text{ mM}^{-1} \cdot \text{s}^{-1}$  per nanoparticle. In another approach based on perfluorocarbon, Wickline et al. [125] reported more than 90,000  $\text{Gd}^{3+}$  ion per particle. This resulted into an ion based  $r_1$  relaxivity of  $17.9 \text{ mM}^{-1} \cdot \text{s}^{-1}$  and particle based relaxivity of  $1.69 \cdot 10^6 \text{ mM}^{-1} \cdot \text{s}^{-1}$ . The diameter of the nanoparticle used was approximately 250

nm. This was a very promising approach as it incorporated a large number of gadolinium diethylenetriaminepentaacetic acid (Gd-DTPA) complexes on the surface of perfluorocarbon nanoparticles. Zhilang et al. [35] synthesized paramagnetic porous polymersomes where the encapsulated  $\text{Gd}^{3+}$  chelates were attached to dendrimers, with a diameter of the polymersomes in the order of 125 nm. On an average 44,000  $\text{Gd}^{3+}$  were encapsulated within each polymersome. These polymersomes resulted into relaxivity values of  $7.2 \text{ mM}^{-1}\cdot\text{s}^{-1}$  per  $\text{Gd}^{3+}$  and 315, 637  $\text{mM}^{-1}\cdot\text{s}^{-1}$  per vesicle. The higher relaxivity was achieved by a slower rotational rate (caused by the attachment to the dendrimer) while maintaining an efficient water exchange due to the porosity of the polymersome. In another approach [161], Ru (bpy):  $\text{Gd}^{3+}/\text{SiO}_2$  nanoparticles were synthesized using water-in-oil (W/O) microemulsion system. These paramagnetic silica nanoparticles with a diameter of approximately 100 nm have been reported to exhibit a  $r_1$  of  $9.0 \text{ mM}^{-1}\cdot\text{s}^{-1}$  per Gd ion (4.7T) and contain 16,000  $\text{Gd}^{3+}$  ions per nanoparticle, which resulted in a  $r_1$  value of  $140,000 \text{ mM}^{-1}\cdot\text{s}^{-1}$  per nanoparticle. Winter et al. [211] have used lipid encapsulated, perfluorocarbon nanoparticles for fibrin detection and for the detection of the molecular signature of angiogenesis. They have compared Gd-DTPA-phosphatidylethanolamine (PE) with Gd-DTPA-bis-oleate (BOA) nanoparticles. Gd-DTPA-BOA paramagnetic nanoparticles present more than 50,000 Gd-DTPA chelates on the surface of a 250 nm nanoparticle, with molecular relaxivity in excess of  $1,000,000 \text{ mM}^{-1}\cdot\text{s}^{-1}$ . Substitution of Gd-DTPA-BOA with Gd-DTPA-PE resulted in a molecular relaxivity of  $2,480,000 \text{ mM}^{-1}\cdot\text{s}^{-1}$  per nanoparticles. This enhancement in relaxivity is likely due to the faster water exchange with the surface gadolinium. The ion-based relaxivities at 1.5T for Gd-DTPA-BOA and Gd-DTPA-PE were 17.7 and 33.7  $\text{mM}^{-1}\cdot\text{s}^{-1}$  respectively. The encapsulation of gadolinium complexes inside apoferritin spheres was presented by Aime et al. [5]. Approximately 10 units of the hydrophilic gadolinium chelate complex were loaded per apoferritin sphere, this approach resulted in a very high relaxivity value of about  $80 \pm 5 \text{ mM}^{-1}\cdot\text{s}^{-1}$ . This increase was interpreted as a result of multiple interactions between the  $\text{Gd}^{3+}$ , water molecules, and exchangeable protons. Another approach was developed by Reynolds et al. [152]. The nanoparticles loaded with gadolinium salt in an intermediate layer caused a reduction in the relaxation time. Since relaxivities were not reported, a comparison with commercial contrast agents is not possible.



An enhancement in the relaxivity after encapsulation of the contrast agent into polymeric shells or attachment to macromolecules in the above discussed cases is likely due to reduction in the rotational correlation time of the  $Gd^{3+}$  chelate. Besides an enhancement in the relaxivity, a further important advantage of the multimeric contrast agent encapsulation into polymeric shells results from the potential high payload of the contrast agent per vesicle and the potential for surface functionalization. The resulting higher amount of contrast agent per binding site is supposed to significantly increase the sensitivity of MRI, especially in molecular imaging applications. Consequently, agents with many efficiently relaxing paramagnetic centers confined into a small space are advantageous over large macromolecules with only few  $Gd^{3+}$  centers [114]. For a non-invasive monitoring of local intravesicle delivery with MRI, Chen et al. [34] encapsulated Gd-DTPA into biodegradable, bioadhesive polymeric micro particles.

Recently, we have introduced the concept of applying the principle of inverse miniemulsion [39] to encapsulate different contrast agents like Magnevist<sup>®</sup> (Schering, Germany), Gadovist<sup>®</sup> (Schering, Germany) and Multihance<sup>®</sup> (Bracco, Italy) in various types of polymeric shells [88], resulting in stable capsules with high concentration of contrast media. Miniemulsion is defined as a system where small droplets with high stability in a continuous phase are created by using the high shear. The system is called a “direct miniemulsion” if the dispersed phase is hydrophobic and an “inverse miniemulsion” if the dispersed phase is hydrophilic. In general, the use of miniemulsions technique allows producing small, stable droplets, obtained by intense shearing of a mixture containing hydrophobic monomer, water, surfactant and a hydrophobe (terminology is used when process is direct miniemulsion) or lipophobe (terminology is used when process is inverse miniemulsion). For the stable production of these polymeric nanocapsules phenomenon of Ostwald ripening and coalescence process needs to be suppressed. Coalescence is the process of aggregation of two droplets to form one larger droplet through collision, while Ostwald ripening is defined as the process whereby large droplets grow at the expense of smaller ones due to the transport of dispersed phase molecules from the smaller to the larger droplets through the continuous phase. Stabilization against coalescence can be obtained by means of addition of suitable surfactants which can act as steric or electrostatic stabilizing agents. Ostwald ripening can be suppressed by the addition of hydrophobe or lipophobe to the dispersed phase. This lipophobe acts as an osmotic pressure

agent and cannot diffuse from one droplet to other and some agent is trapped in each droplet. This provides an osmotic pressure inside the droplets, which counteracts the Laplace pressure (Laplace pressure is the pressure difference between the inside and the outside of a bubble or droplet). The use of the miniemulsion technique thus produces small stable droplets and subsequent polymerization of these droplets leads to particles or capsules, which ideally keep their size [106, 107, 184].

In the presented work, contrast agent loaded nanocapsules were synthesized using inverse miniemulsion technique. Various types of nanocapsules were synthesized using different kind of monomers and contrast agents. The relaxivity values of the resultant nanocapsules were measured by MRI. The chemical composition of the polymeric nanocapsules was investigated by Fourier Transform-Infra Red Spectroscopy (FT-IR). Location of the contrast agents within the nanocapsules was studied by using various analytical techniques like TEM, EFTEM, STEM, and EDX spectroscopy. Further as a proof for the stability of these capsules the effectiveness of the contrast agent loaded nanocapsules were assessed in the physiological fluid, human blood plasma.

### **3A.1 Materials and Methods**

#### **3A.1.1 Synthesis of nanocapsules\***

Magnetic resonance contrast agent loaded nanocapsules were prepared by an inverse miniemulsion technique [88]. In a typical synthesis procedure, 0.05 g monomer-1 [1,6-hexanediol (Aldrich) for polyurethane nanocapsules, diethylenetriamine (Aldrich) for polyurea, and dextran ( $M_w \sim 70,000 \text{ g}\cdot\text{mol}^{-1}$ , Fluka) for crosslinked dextran nanocapsules] were dissolved in 0.65 g water (for reference capsules without any contrast agents) or contrast

\* The contrast agent loaded nanocapsules were provided by Dr. Umaporn Paiphansiri, (Prof. Katherina Landfester group) MPI Mainz.

agent solution [Magnevist<sup>®</sup> (Gd-DTPA, Schering AG Berlin, Germany), Gadovist<sup>®</sup> (Gadobuterol, Schering AG Berlin, Germany), Multihance<sup>®</sup> (Gadobenate dimeglumine, Bracco, Italy)] for contrast agent loaded nanocapsules along with 0.015 g NaCl (Fischer) in a 5 ml glass vial. This mixture was added to a surfactant solution of P (B/E-b-EO) [consisting of a poly (butylene-co-ethylene) block ( $M_w = 3700 \text{ g}\cdot\text{mol}^{-1}$ ) and a poly (ethylene oxide) block ( $M_w = 3600 \text{ g}\cdot\text{mol}^{-1}$ ) synthesized by anionic polymerization [166]] in 3.75 g cyclohexane (VWR). After stirring for 1 h, the miniemulsion was homogenized in an ice-cooled bath by ultrasonication for 3 min at 70% amplitude with a Branson sonifier W450 digital (6.4 mm tip). Then a mixture containing 0.14 g monomer 2 [tolylene-2, 4-diisocyanate (TDI, Fluka)], surfactant P (B/E-b-EO) and cyclohexane were added continuously over a time period of 300 s with constant stirring. In the case of polyurethane and crosslinked dextran capsules, the interfacial polyaddition was done at 60 °C and for polyurea capsules at room temperature.

To redisperse the nanocapsules in an aqueous medium, 0.6 g of the nanocapsules in the cyclohexane phase were mixed with an aqueous solution of 30 mg sodium dodecyl sulphate (SDS) dissolved in 18 g of water. The mixture was stirred for 1 h at 40 °C. Then the redispersion was kept in an ultrasonication bath for 5 min to avoid the aggregation of the nanocapsules before further vigorous stirring at 40 °C for 12 h. A schematic representation of a typical synthesis is shown in Fig.3A.1.

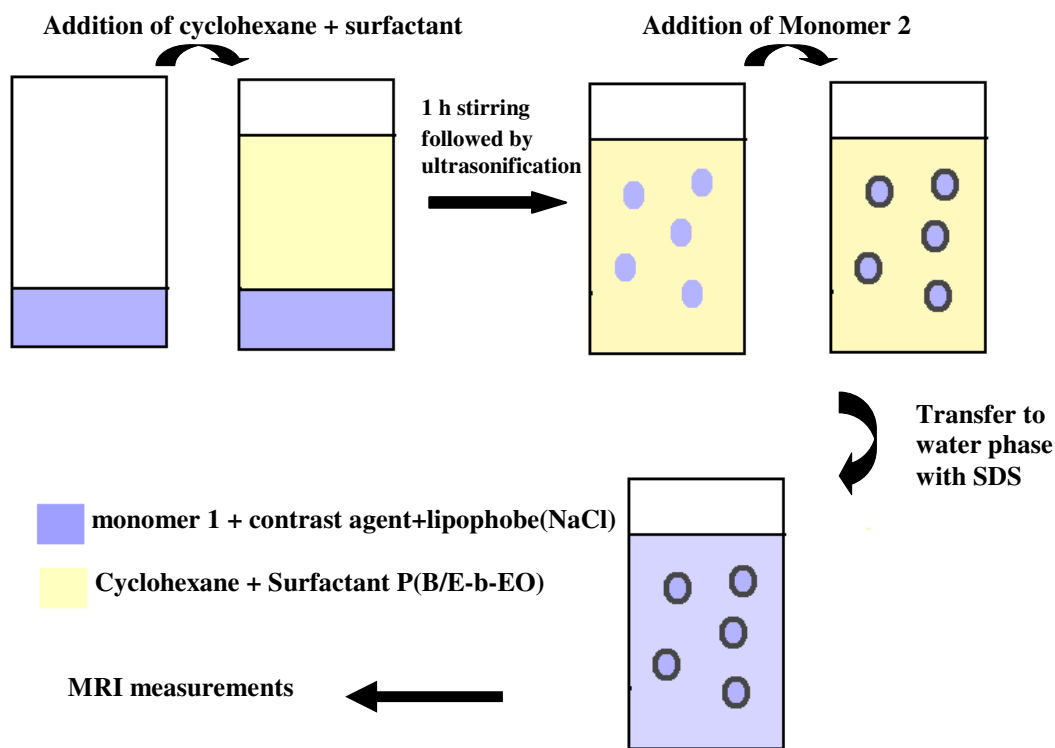


Figure 3A.1: Schematic representation of the synthesis of contrast agent loaded polymeric nanocapsules by inverse miniemulsion approach.

For the evaluation of the impact of monomer-1 versus monomer-2 ratios on the relaxivity of encapsulated contrast agents, the molar ratio of monomer-1(diol) versus monomer-2 (TDI) was varied. Different nanocapsules were prepared using four different diol:TDI ratios (1:2, 1:4, 1:8, 1:10) keeping the amount of diol constant.

### 3A.1.2 Preparation of dilution series for reference experiment of gadolinium based contrast agent

As reference experiments, dilution series of Magnevist<sup>®</sup>, Gadovist<sup>®</sup> Multihance<sup>®</sup> were prepared in water. A stock solution with a  $Gd^{3+}$  concentration of 5 mM was prepared by adding 100  $\mu$ l of Magnevist<sup>®</sup> (concentration of commercially available Magnevist<sup>®</sup> is 0.5 M

solution) in 10 ml of water, 50  $\mu$ l of Gadovist<sup>®</sup> (concentration of commercial available Gadovist<sup>®</sup> is 1 M) solution in 10 ml of water and 100  $\mu$ l of Multihance<sup>®</sup> (concentration of commercially available Multihance<sup>®</sup> is 0.5 M) solution in 10 ml of water. This stock solution was further diluted with a requisite amount of water to get dilution series ranging from 1 mM to 0.0625 mM of Gd<sup>3+</sup> concentration and the  $T_1$  values were measured at a 1.5T MRI instrument.

### 3A.1.3 Quantification of gadolinium content<sup>\*</sup>

The total concentrations of gadolinium (Gd<sup>3+</sup>) in the stock solutions (encapsulated nanocapsules in aqueous phase) were determined by Inductively Coupled Plasma - Optical Emission Spectroscopy (VARIAN-Vista-Pro, CCD-simultaneous ICP-OES). The sample preparation for analysis included a microwave digestion for 1 h at 150 °C after adding HNO<sub>3</sub>/aq. H<sub>2</sub>O<sub>2</sub>. Then the resultant mixture was used for the analysis of Gd<sup>3+</sup> content by ICP-OES. The concentration of Gd<sup>3+</sup> containing solution includes the concentration error of  $\pm 4\%$ .

### 3A.1.4 Characterization by electron microscopy

Transmission electron microscopy (TEM) experiments were performed on a Philips EM400 microscope operating at 80 kV. A drop of diluted aqueous nanocapsules suspension was mounted on 400 - mesh carbon coated copper grids and dried at room temperature. The size distribution of the nanocapsules was measured by dynamic light scattering technique (DLS) using a zeta Nanosizer (Malvern Instruments, U.K.) at a single scattering angle of 173° and a temperature of 25°C. The shell thickness was determined by averaging the shell thicknesses of several capsules ( $15\pm 5$ ) in TEM images.

TEM analysis was also performed after freeze drying the sample. For freeze drying, the samples were adsorbed on a carbon coated 3 mm electron microscopical copper grid and were

<sup>\*</sup>These measurements were done by Dr. Dirk Dautzenberg, Institute for radiochemistry, TU-Munich, Germany.

fast frozen in liquid propane super-cooled by liquid nitrogen. Later the grids were transferred to a freeze etching device BAF 300 (Blazers) and freeze dried at -90 °C in a vacuum of about  $10^{-6}$  mbar. Sample was then coated with 6 nm of carbon by electron beam evaporation. Then these samples were warmed up to room temperature and imaged in a 200 kV Philips TEM at an accelerating voltage of 10 kV<sup>\*</sup>.

Energy filtered TEM (EFTEM) and scanning TEM (STEM) investigation was done at a CM 20 TEM at 200 kV in conventional bright field (BF) mode, and in Titan 80-300 at 300 kV in BF mode respectively. Samples were prepared from concentrated colloidal solutions. A soapy bubble was inflated from the above solution and a carbon-coated copper TEM grid was placed on it, so that a thin film of the solution covered the whole grid. The grid was then dried in air at room temperature for 30 h before analysis.

### 3A.1.5 Gadolinium content per capsule

The number of  $Gd^{3+}$  ions per capsule was calculated on the basis of assumptions that all the  $Gd^{3+}$  is inside the capsule, and all monomers added forms the polymer. On the basis of solid mass ( $P_M$ ) of the polymer, overall volume of the polymer is calculated by  $P_v = \frac{P_M}{\rho}$  with  $\rho$

being the density of the polymeric nanocapsule ( $1.21 \text{ g}\cdot\text{cm}^3$  for polyurethane) and  $P_M$  (0.19 g).

Volume of one capsule was calculated using the formula  $P_v^C = \frac{4}{3}\pi[r_c^3 - (r_c - S_T)^3]$ . ( $r_c = 100$

nm,  $S_T = 20$  nm,  $Gd_M = 0.051\text{g}$ ). The number of capsules ( $n_c$ ) was then computed using the

formula  $n_c = \frac{P_v}{P_v^C}$ . The Gadolinium load per capsule ( $Gd_M^C$ ) is obtained by  $Gd_M^C = \frac{Gd_M}{n_c}$ .

Gadolinium complex per capsule was then obtained by the formula  $Gd_p^c = \frac{6.023 \cdot 10^{23} \cdot Gd_M^C}{157}$ ,

where 157 is the molar mass of Gd.

<sup>\*</sup> Analysis was done by Prof. Paul Walther (Central Electron Microscopy Unit, University of Ulm), and Dr. Andrey Chuvilin (Electron Microscopy Group of Materials Science, University of Ulm) Ulm, Germany.

### 3A.1.6 Stability studies

To prove the stability of the nanocapsules two separate experiments were done. In the first experiment the redispersed (in water) contrast agent loaded nanocapsules were dialyzed with an Amicon membrane (exclusion Mw 30,000) against water for 5 h at 2000 rpm in a centrifuge. The concentration of  $Gd^{3+}$  in the resultant solution containing the capsules (supernatant solution) was quantified using ICP-OES and on the basis of the concentration so obtained a series of concentrations of  $Gd^{3+}$  was made. Relaxivity value of the resultant series was then measured by MRI (explained in section 3A.1.7).

Second experiment was done in a physiological fluid human blood plasma which was collected from the blood bank. The aim was to prove that nanocapsules were stable in physiological fluid and the  $Gd^{3+}$  complexes were well inside the nanocapsules. For this purpose, two different types of polymeric shell (polyurethane- and dextran-) encapsulated, Multihance<sup>®</sup> loaded nanocapsules were used. These nanocapsules (which were in the water phase) were then added in requisite amount to plasma medium. The concentration of  $Gd^{3+}$  in the resultant plasma medium containing the capsules was quantified using ICP-OES and on the basis of the concentration so obtained a series of concentrations of  $Gd^{3+}$  was made. Relaxivity value of the resultant series was then measured by MRI (explained in section 3A.1.7).

### 3A.1.7 MRI relaxivity measurements and data analysis

Relaxivity values of different encapsulated and non-encapsulated contrast agents were determined in water and plasma. All imaging experiments were performed at 1.5T on a clinical scanner (Intera, Philips Medical Systems) using a standard head coil. b-SSFP-Look Locker [37, 115] technique [1.5/12000/16° echo time (ms) / repetition time (ms) / flip angle (°)], spatial resolution of 1 mm<sup>3</sup>, temporal resolution of 30 ms was used to measure the longitudinal relaxation rate ( $1/T_1$  in s<sup>-1</sup>). Longitudinal relaxivities ( $r_1$ ) were retrieved from a dilution series containing varying Gadolinium ( $Gd^{3+}$ ) concentrations in water and in human plasma (Details of  $T_1$  calculations are explained in section 2.8). The longitudinal relaxation

rate ( $1/T_1$  in  $s^{-1}$ ) was plotted against  $Gd^{3+}$  concentration (mM) of the sample and the slope was calculated according to equation (1) yielding the value of  $r_1$  relaxivity:

$$\frac{1}{T_1^{obs}} = \frac{1}{T_1^d} + r_1[C] \quad (1)$$

where  $1/T_1^{obs}$  is the relaxation rate of the sample containing  $Gd^{3+}$  and  $1/T_1^d$  is the relaxation rate of the reference sample without  $Gd^{3+}$  (i.e. is pure water/plasma),  $C$  is the concentration of  $Gd^{3+}$  (in mM) and  $r_1$  is the slope of the linear correlation (equal to relaxivity in  $mM^{-1} \cdot s^{-1}$ ).

## 3A.2 Results and Discussion

### 3A.2.1 Effect of various biodegradable polymeric shells on the relaxivity

Efficient water exchange through the polymeric shell is one of the key factors which affect the  $T_1$  relaxivity of encapsulated contrast agents. Magnevist<sup>®</sup> was encapsulated by using three different biodegradable polymeric shells i.e polyurea, dextran, and polyurethane. Relaxivity values of the resultant polymeric shell encapsulated contrast agent loaded nanocapsules are given in Table 3A.1 (For detailed  $T_1$  data refer Appendix A, Table A.1). Sizes of these nanocapsules as measured by DLS and TEM are shown in Table 3A.1



Table 3A.1: Effect of different polymeric shells on diameter and relaxivity of encapsulated Magnevist<sup>®</sup> nanocapsules in water phase.

Polymeric Shell	Average size (nm) <sup>*</sup>	PDI	Average Size (nm) <sup>£</sup>	Average shell thickness (nm) <sup>\$</sup>	Relaxivity (mM <sup>-1</sup> ·s <sup>-1</sup> )	R <sup>2#</sup>
Polyurethane	250.45 ± 29.15	0.281	170	24	4.35 ± 0.035	0.999
Dextran	301.25 ± 30.7	0.534	190	20	4.40 ± 0.080	0.999
Polyurea	210 ± 30.7	0.281	220	23	4.60 ± 0.027	0.998

<sup>\*</sup> Measured by DLS; <sup>£</sup> Measured by TEM; <sup>\$</sup> Measured by TEM.

<sup>#</sup> R<sup>2</sup> is measure of goodness of fit of linear regression.

DLS measurement shows higher diameter in case of dextran shell encapsulated Magnevist<sup>®</sup> nanocapsules as compared to polyurea and polyurethane shells encapsulated Magnevist<sup>®</sup>. The size of nanocapsules depends on several factors namely the chemical nature, molecular weight, viscosity and interfacial tension. Increased size in case of dextran encapsulated contrast agent nanocapsules could be due to the reason that dextran (which is used as monomer for cross linked dextran nanocapsules) is a polysaccharide having high molecular weight (70,000 g·mol<sup>-1</sup>) as compared to 1,6 hexanediol (monomer used for polyurethane shell nanocapsules) having molecular weight (118.17 g·mol<sup>-1</sup>) and diethylenetriamine (monomer used for polyurea shell nanocapsules) and its structure comprises of long chains as compared to short chain structures of 1,6 hexanediol and diethylenetriamine. Thus high molecular weight and increased viscosity after ultrasonification due to long chain structure in the case of dextran could be the possible reason for the observed increase in size. However in the case of diameter obtained from TEM the reduction in size could be due to shrinkage of the nanocapsules during the process of drying while sample preparation for TEM.

TEM images of these nanocapsules are shown in Fig. 3A.2 (A, B) for polyurea and dextran shell nanocapsules, respectively and Fig. 3A.5 (B) for polyurethane shell. The  $T_1$  relaxivity values of these encapsulated contrast agents were  $4.35 \pm 0.035 \text{ mM}^{-1} \cdot \text{s}^{-1}$ ,  $4.40 \pm 0.08 \text{ mM}^{-1} \cdot \text{s}^{-1}$

and  $4.60 \pm 0.027 \text{ mM}^{-1} \cdot \text{s}^{-1}$  for Magnevist<sup>®</sup> encapsulated in polyurethane, cross linked dextran and polyurea nanocapsules as shown in Table 3A.1. The non-encapsulated Magnevist<sup>®</sup> solution showed a relaxivity of  $4.08 \pm 0.01 \text{ mM}^{-1} \cdot \text{s}^{-1}$  as shown in Table 3A.3.

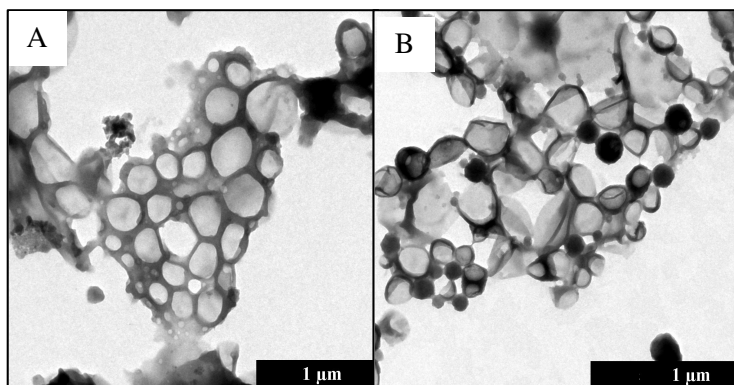


Figure 3A.2: TEM image of (A) Polyurea encapsulated Magnevist<sup>®</sup> nanocapsules in water phase (B) Dextran encapsulated Magnevist<sup>®</sup> nanocapsules in water phase.

It was observed that all polymeric nanocapsules are capable of maintaining the relaxivity of the contrast agent. It can be pointed out that the required sufficient water exchange between the water bound to the contrast agent and free water molecules in the continuous phase is well obtained through these polymeric shells.

### 3A.2.2 Effect of polyurethane encapsulated different contrast agents on relaxivity

Three different types of gadolinium-based contrast agents were loaded in polyurethane-shell nanocapsules (i.e. Magnevist<sup>®</sup> (gadopentate dimeglumine), Gadovist<sup>®</sup> (gadobutrol), and Multihance<sup>®</sup> (gadobenate dimeglumine)). These three contrast agents were chosen because of the differences in their chemical structure and functionalities. Magnevist<sup>®</sup> has a linear structure and is ionic in nature (Fig. 3A.3). Multihance<sup>®</sup> is also linear and ionic in nature, but compared with the gadopentetate chelate structure of Magnevist<sup>®</sup>, the gadobenate chelate of Multihance<sup>®</sup> is characterized by the presence of a (bulky) hydrophobic benzyloxymethyl

substituent (Fig. 3A.4 (A)). This imparts Multihance<sup>®</sup> a markedly higher  $T_1$  relaxivity in plasma compared to other gadolinium based agents, due to the weak, transient interaction with serum albumin [165, 172]. Gadovist<sup>®</sup> is cyclic and non ionic in nature (Fig. 3A.4 (B)) and is the only available contrast agent with 1.0 M formulation which is feasible due to its low viscosity and osmolality [93, 112, 172]. Magnevist<sup>®</sup> and Multihance<sup>®</sup> are available in 0.5 M formulation. Relaxivity values of these encapsulated contrast agents are shown in Table 3A.2 (For detailed  $T_1$  data refer Appendix A, Table A.2).

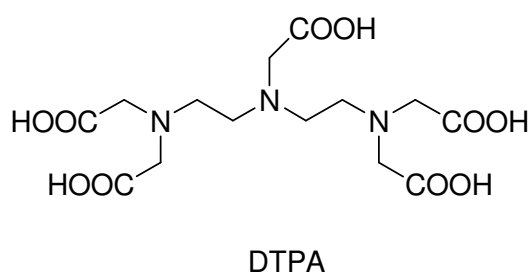


Figure 3A.3: Structure of DTPA moiety of Magnevist<sup>®</sup> contrast agent.

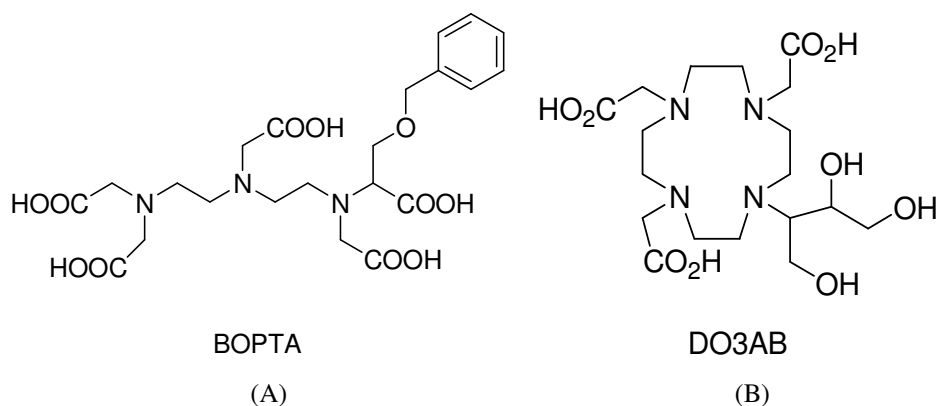


Figure 3A.4: Structure of BOPTA moiety of Multihance<sup>®</sup> contrast agent (A) and DO3AB moiety of Gadovist<sup>®</sup> contrast agent (B).

As shown in Table 3A.2 for nanocapsules loaded with water and NaCl (i.e. control nanocapsules without contrast agent) the average diameter is 105 nm as measured by DLS and 120 nm as measured by TEM. As compared to nanocapsules without contrast agents,

nanocapsules loaded with different contrast agents show an increase in size (Table 3A.2). This may be due to water diffusion from the continuous aqueous phase into the core as there is a higher concentration of the dissolved molecules in the core (NaCl + gadolinium complex) as compared to capsules without contrast agents [88].

Table 3A.2: Effect of polyurethane encapsulated different contrast agents loaded nanocapsules on diameter and relaxivity in water phase.

Polyurethane (PU) nanocapsules	Average size (nm) <sup>*</sup>	PDI	Average Size (nm) <sup>‡</sup>	Average shell thickness (nm) <sup>§</sup>	Relaxivity (mM <sup>-1</sup> ·s <sup>-1</sup> )	R <sup>2#</sup>
without CA <sup>**</sup>	105.00 ± 10.01	0.125	120	14	NA	NA
with Magnevist <sup>®</sup>	301.25 ± 48.45	0.281	170	24	4.35 ± 0.035	0.999
with Gadovist <sup>®</sup>	258.8 ± 11.10	0.308	190	22	4.73 ± 0.035	0.998
with Multihance <sup>®</sup>	217.25 ± 32.25	0.250	170	26	5.64 ± 0.18	0.998

<sup>\*\*</sup> CA- Contrast Agent; <sup>\*</sup> Measured by DLS; <sup>‡</sup> Measured by TEM; <sup>§</sup> Measured by TEM. <sup>#</sup> R<sup>2</sup> is measure of goodness of fit of linear regression.

TEM images show a dark rim on the inner border of the capsule shell for contrast agent-loaded nanocapsules indicating the presence of high density gadolinium on the inner surface of the shell (Fig. 3A.5 (b,c and d and Fig. 3A.10)).

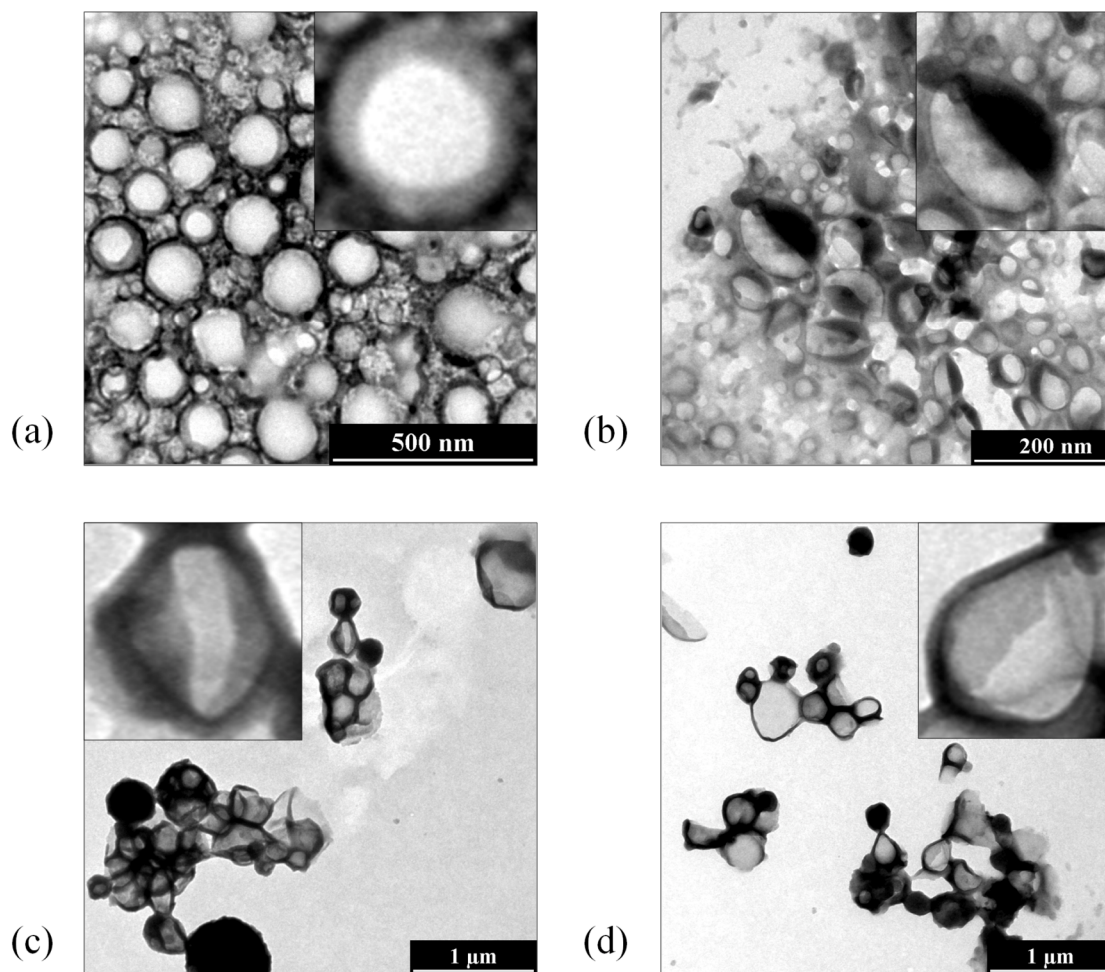


Figure 3A.5: TEM image of (a) polyurethane encapsulated nanocapsules without contrast agents, (inset represents one single capsule magnified from the cluster of capsules) (b) with contrast agent Gadovist<sup>®</sup> (inset represents one single capsule magnified from the cluster of capsules) (c) with contrast agent Multihance<sup>®</sup> (inset represents one single capsule magnified from the cluster of capsules) (d) with contrast agent Magnevist<sup>®</sup> (inset represents one single capsule magnified from the cluster of capsules).

This rim is not present in nanocapsules without contrast agent Fig. 3A.5 (a). The resultant relaxivity values of these polyurethane encapsulated contrast agents are shown in Table 3A.2 (For detail  $T_1$  data refer appendix A, Table A.2). For reference, we measured the relaxivities of non-encapsulated or free contrast agent's solution under the same experimental condition. The results are presented in Table 3A.3 (For detail  $T_1$  data refer appendix A, Table A.3).

Table 3A.3: Relaxivity values of nonencapsulated contrast agents used as reference.

Contrast agents	Relaxivity ( $\text{mM}^{-1}\cdot\text{s}^{-1}$ )	$R^{2\#}$
Magnevist <sup>®</sup>	$4.08 \pm 0.010$	0.999
Gadovist <sup>®</sup>	$4.37 \pm 0.033$	0.999
Multihance <sup>®</sup>	$5.63 \pm 0.088$	0.999

<sup>#</sup> $R^2$  is measure of goodness of fit of linear regression.

The relaxivity values of the encapsulated contrast agents show a slight increase compared to their non-encapsulated counterparts. This observation could be due to the adsorption (or the entrapment) of the contrast agents to the inner surface of the polymeric shell which may have resulted in a slower tumbling rate of the gadolinium complex.

### 3A.2.3 Effect of variation of monomer ratios on relaxivity

For the assessment of the optimal nanocapsule design, shell properties such as monomer ratios and the resulting stiffness and capsule diameters of the shell were investigated. Variation of the amount of monomer 2 (TDI) reveals diameters of the resultant capsule between 100 and 200 nm (Table 3A.4). Main impact of increasing the TDI appears to be increasing stiffness of the shell material. Increasing amount of TDI increases the number of isocyanate groups (NCO), which can react with groups other than the OH of the diol. Reaction sites can either be the dimeglumine containing reactive groups, for instance hydroxyl and amine groups, or water resulting in the formation of urethane and urea, which can significantly increase the stiffness of the formed polymer shell [105]. The crosslinked structure formed will impact the chain flexibility as can be demonstrated by the glass transition temperature ( $T_g$ ) of the nanocapsules, which increase with increasing TDI content (-16.7, -15.9, -8.5 and -2.8 °C for OH:TDI molar ratio from 1:2 to 1:10)\*. There is no substantial influence on the relaxivity values with increase in TDI (Table 3A.4) and the resultant capsules are found to be similar without any obvious change in morphology as shown by TEM images (Fig. 3A.6).

\*Provided by Dr. Umaporn Paiphansiri, (Prof. Katherina Landfester group) MPI Mainz

For vascular applications, the size of the nanocapsules should be in the range of 150 - 280 nm [110, 195]. Thus nanocapsules obtained by varying the ratio of diol:TDI are all within this range and have almost similar relaxivity.

Table 3A.4: Effect of different moles of TDI for a constant mole of Diol on diameter and the relaxivity values of polyurethane encapsulated Magnevist<sup>®</sup> nanocapsules in water phase.

Molar ratio of diol:TDI	Amount of TDI (g)	Average Size (nm) <sup>‡</sup> *	Relaxivity (mM <sup>-1</sup> ·s <sup>-1</sup> )	R <sup>2#</sup>
1:2	0.14	170 ± 25	4.35 ± 0.03	0.999
1:4	0.28	110 ± 20	4.48 ± 0.01	0.999
1:8	0.56	190 ± 40	4.37 ± 0.06	0.999
1:10	0.70	120 ± 20	4.40 ± 0.04	0.999

<sup>‡</sup> Measured by TEM. <sup>#</sup> R<sup>2</sup> is measure of goodness of fit of linear regression.

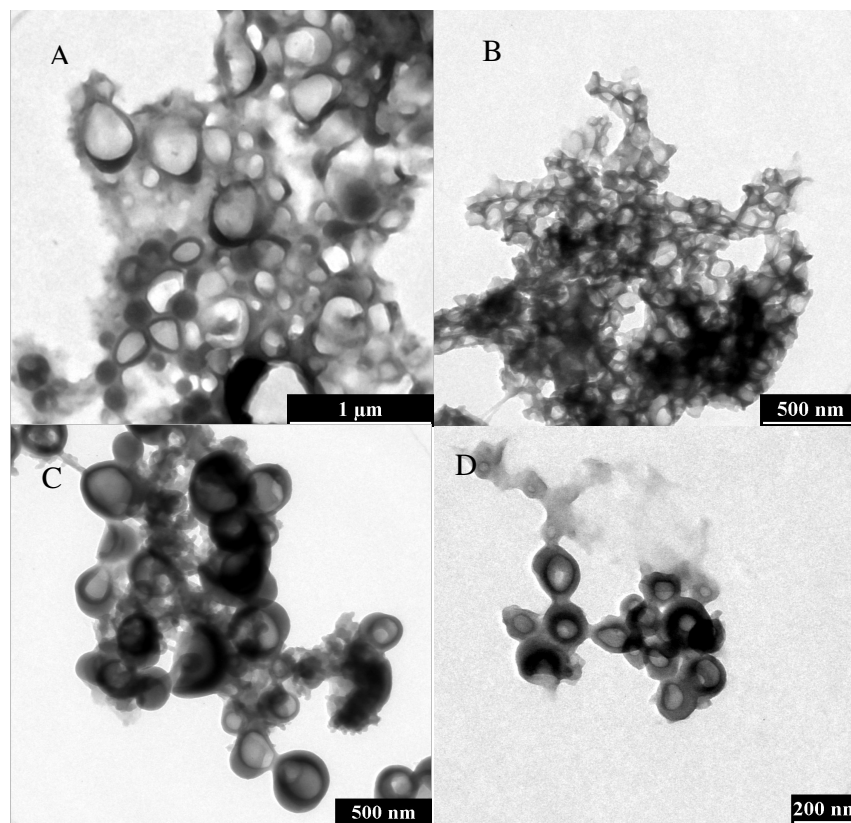


Figure 3A.6: TEM image of polyurethane encapsulated Magnevist® nanocapsules in water phase with diol:TDI molar ratio (A) 1:2 (B) 1:4 (C) 1:8 (D) 1:10.

### 3A.2.4 Distribution of the contrast agent within the nanocapsule

In Magnevist® contrast agent, Gadolinium ion ( $Gd^{3+}$ ) with three positive “unit charges” is trapped in a negatively charged chelate consisting of the dimeglumine salt of diethylene-triamine-pentaacetic acid (DTPA) which has 5 negatively charged carboxyl groups (5 unit charges). The  $Gd$ -DTPA ion has two negative charges ( $+3-5 = -2$ ) and is accompanied by 2 positively charged meglumine ion for electron neutrality. Contrast agent can bind to the polymeric shell either due to the reaction of the DTPA part or due to the dimeglumine part with monomer 2 (TDI) during synthesis. However, in the absence of any direct proof for the above hypothesis (which functional group of contrast agent is reacting), indirect evidences can



be obtained from the FT-IR spectral studies and from the synthesis of nanocapsules using Magnevist® (Gd-DTPA) as monomer 1 and TDI as monomer 2.

FT-IR spectra of Magnevist® + TDI, Diol+ TDI and Magnevist®+Diol+TDI (obtained with cyclohexane as continuous phase before transfer to the water phase) are shown in Fig. 3A.7.

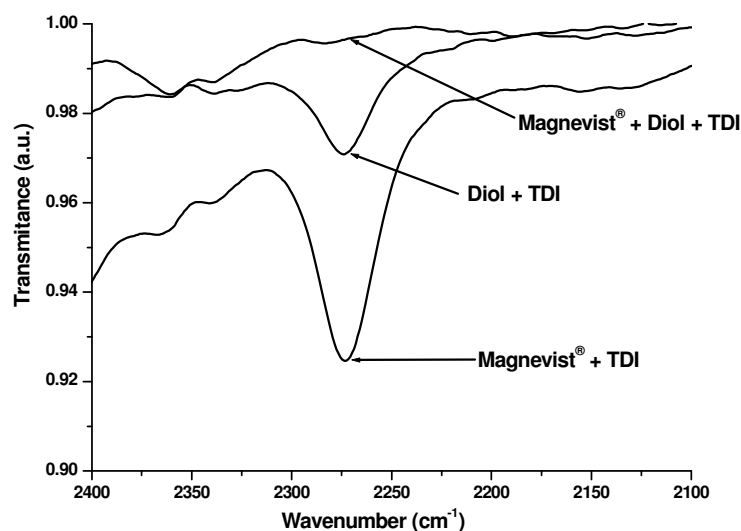


Figure 3A.7: Combined FT-IR Spectra of Magnevist® + TDI, Diol+ TDI & Magnevist®+Diol+TDI.

The peak at  $2230\text{ cm}^{-1}$  is due to the isocyanate group (NCO) present in TDI (monomer-2, and is seen in the resultant polymer when monomer-1 (1, 6-hexanediol) is used during synthesis [166]. This peak is also seen when, instead of monomer 1, Magnevist® (Gd-DTPA) was added in the synthesis. The IR studies and the morphology of the nanocapsules prepared without addition of hexanediol (Magnevist® + TDI) indicate that one of the components present in Magnevist® can participate in the polyaddition reaction with TDI. The presence of the isocyanate peak in the resultant polymer shell indicates that TDI still has some open sites for reaction. But a complete disappearance of  $2230\text{ cm}^{-1}$  peak was observed when both 1, 6-hexanediol and Magnevist® (Gd-DTPA) were added during synthesis. This indicates a complete consumption of binding sites of the reactive isocyanate group of the TDI due to the presence of two reactants.

This binding was further supported by the synthesis of nanocapsules using Magnevist<sup>®</sup> (Gd-DTPA) as “monomer 1” and TDI as monomer 2. TEM images of the resultant nanocapsules are shown in Fig.3A.8. The resulting nanocapsules showed the relaxivity value,  $4.46 \pm 0.040 \text{ mM}^{-1}\cdot\text{s}^{-1}$  (for detail  $T_1$  data refer appendix A, Table A.5) indicating a similar binding of the contrast agent components as in the diol-Magnevist<sup>®</sup>-TDI nanocapsule.

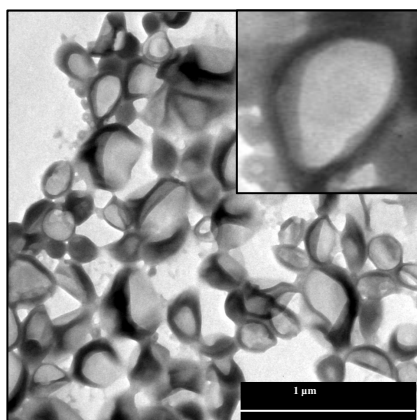


Figure 3A.8: Nanocapsules synthesized by using Magnevist<sup>®</sup> as monomer 1 and TDI as monomer 2. (inset represents one single capsule magnified from the cluster of capsules).

Further, distribution of the contrast agent within these nanocapsules was visualized by energy filtered TEM (EFTEM), scanning TEM (STEM) and energy dispersive x-ray spectroscopy (EDX) studies. The EFTEM image (Fig. 3A.9 (A)) and the complementary STEM image (Fig. 3A.9 (B)) of the Magnevist<sup>®</sup> loaded nanocapsules clearly demonstrate that an element with a high atomic number ( $\text{Gd}^{3+}$ ) forms a thin layer mostly on the inner surface of the shell. The elemental map of  $\text{Gd}^{3+}$  (Fig. 3A.9 (C)) proves the presence of  $\text{Gd}^{3+}$ .

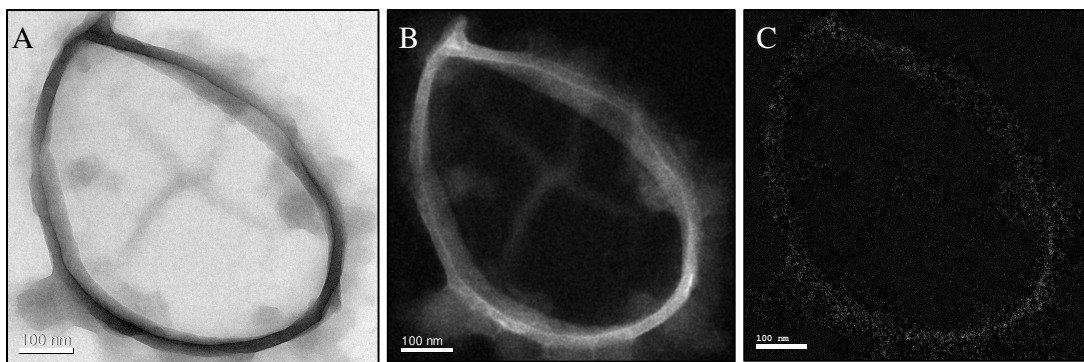


Figure 3A.9: EFTEM image (A) and the complimentary STEM (B) image of an encapsulated Magnevist<sup>®</sup> nanocapsule and elemental mapping of  $Gd^{3+}$  in the same capsule (C).

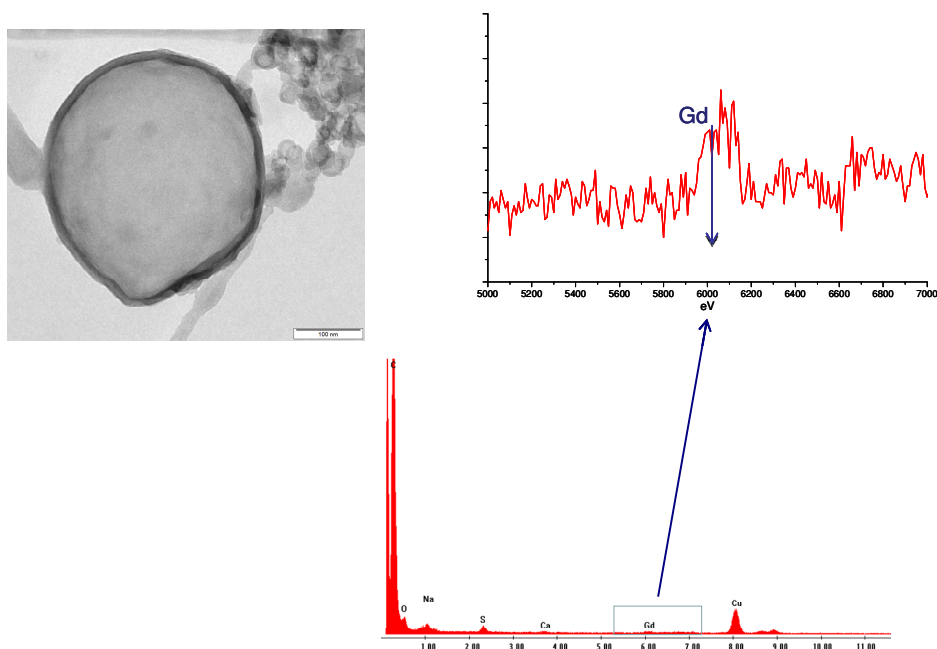


Figure 3A.10: TEM image of encapsulated Magnevist<sup>®</sup> nanocapsule after freeze drying at higher magnification and EDX spectrum.

Further, to avoid diffusion of water during sample preparation, the samples were freeze dried and TEM images along with EDX measurements were obtained (Fig. 3A.10). Analysis of the dark rim section shows the presence of a gadolinium peak at 6.0 kV.

### 3A.2.5 Stability studies

Since the solubility of contrast agent complex in organic solvent is very poor [88], gadolinium complexes stay inside the capsules in the cyclohexane phase. However, during the redispersion of these capsules from cyclohexane phase to the aqueous phase, the complex may leak out of these capsules either by diffusion or by breakage of the capsules. To prove the stability of these encapsulated nanocapsules two different experiments were performed:

- 1) Dialysis experiment (in water medium) for polyurethane-encapsulated Magnevist<sup>®</sup> loaded nanocapsules.
- 2) Stability studies of polyurethane (PU) and dextran shell encapsulated Multihance<sup>®</sup> in the physiological fluid (blood plasma).

Dialysis studies were carried out for polyurethane-encapsulated Magnevist<sup>®</sup> nanocapsules for 5 h and the Gd<sup>3+</sup> content of the dialysed sample was measured by ICP-OES. MRI studies done for the dilution series made from the dialysed samples resulted in a relaxivity value of  $4.33 \pm 0.022 \text{ mM}^{-1} \cdot \text{s}^{-1}$ , indicating a stable encapsulation of the contrast agent.

Furthermore, stability of the nanocapsules was studied in physiological fluid (blood plasma). Multihance<sup>®</sup> encapsulated in two different polymeric shells i.e. polyurethane (PU) and dextran, were redispersed in water and plasma separately and the respective relaxivity values were measured (Table 3A.5). The  $r_1$  relaxivity values of non-encapsulated Multihance<sup>®</sup> in water and plasma were  $5.63 \pm 0.08 \text{ mM}^{-1} \cdot \text{s}^{-1}$  and  $7.18 \pm 0.05 \text{ mM}^{-1} \cdot \text{s}^{-1}$  respectively (For detailed  $T_1$  data refer Appendix A, Table A.7 and A.8). Significant increase in the relaxivity in plasma medium is due to the weak binding of Multihance<sup>®</sup> to the protein serum in human plasma [165, 172]. Because of this weak binding, the relaxivity increases considerably in human blood plasma compared to water. PU-encapsulated Multihance<sup>®</sup> showed relaxivities of  $5.64 \pm 0.18 \text{ mM}^{-1} \cdot \text{s}^{-1}$

in water and  $5.46 \pm 0.038 \text{ mM}^{-1}\cdot\text{s}^{-1}$  in plasma. Relaxivities of dextran-encapsulated Multihance<sup>®</sup> are found to be  $5.42 \pm 0.066 \text{ mM}^{-1}\cdot\text{s}^{-1}$  in water and  $5.58 \pm 0.032 \text{ mM}^{-1}\cdot\text{s}^{-1}$  in plasma. The unpaired TTest yields ( $p>0.05$ ) for relaxivity values measured in water and blood plasma indicating no difference between the values obtained in two different medium. From this it can be concluded that no substantial amount of free Multihance<sup>®</sup> is present in the plasma. Thus the contrast agent is well inside the polymer nanocapsules and stable in the physiological fluid plasma.

Table 3A.5: Relaxivity values of encapsulated Multihance<sup>®</sup> in polyurethane and dextran shell in plasma and water. For reference, relaxivity values of nonencapsulated Multihance<sup>®</sup> in water and plasma are shown.

Sample	Relaxivity ( $\text{mM}^{-1}\cdot\text{s}^{-1}$ )	$R^{2\#}$
Non encapsulated Multihance <sup>®</sup> in water	$5.63 \pm 0.08$	0.999
Non encapsulated Multihance <sup>®</sup> in plasma	$7.18 \pm 0.055$	0.999
PU encapsulated Multihance <sup>®</sup> in water	$5.64 \pm 0.18$	0.999
PU encapsulated Multihance <sup>®</sup> in plasma	$5.46 \pm 0.038$	0.941
Dextran encapsulated Multihance <sup>®</sup> in water	$5.42 \pm 0.066$	0.999
Dextran encapsulated Multihance <sup>®</sup> in plasma	$5.58 \pm 0.032$	0.992

<sup>#</sup> $R^2$  is measure of goodness of fit of linear regression.

### 3A.2.6 Gadolinium content per capsule

For finding the number of gadolinium complex per capsules, two assumptions were made, all the monomers added to the reaction mixture is used for polymer formation and all the  $\text{Gd}^{3+}$  complexes are well inside the capsules (section 3A.1.5). The average diameter of nanocapsules is taken as 200 nm with an average shell thickness of 20 nm (from TEM). the number of capsules obtained from the respective solid content was  $7.6 \cdot 10^{13}$ . The gadolinium mass per capsule resulted as  $0.67 \cdot 10^{-15} \text{ g}$  with respective number of gadolinium complexes per capsules of  $2.5 \cdot 10^6$ . This resulted into capsule based relaxivity of  $10.75 \cdot 10^6 \text{ mM}^{-1}\cdot\text{s}^{-1}$ .

### 3A.3 Conclusion

Polyurethane-, polyurea- and crosslinked dextran-encapsulated contrast agents (Magnevist<sup>®</sup>, Gadovist<sup>®</sup>, and Multihance<sup>®</sup>) were synthesized using an inverse miniemulsion technique. The diameter of the nanocapsules could be adjusted to the range between 200 and 250 nm by proper adjustment of the process parameters. Maintained or even slightly increased relaxivity of the encapsulated contrast agents in the different biodegradable polymeric shells indicates an efficient water exchange through the shells and hence offers flexibility in choosing the shell material for encapsulation. Various characterization techniques were used to locate the contrast agents within these nanocapsules. The EFTEM, STEM, and EDX maps showed a more pronounced Gd<sup>3+</sup> signal at the inner walls of the shell, indicating binding of the complex within the shell. FT-IR results support the binding of the contrast agent complex to the polymer shell as the nanocapsules can be prepared through polyaddition reaction in inverse miniemulsion without addition of hexane 1, 6-diol. Relaxivity values of the dextran- and polyurethane-encapsulated Multihance<sup>®</sup> nanocapsules in the plasma medium further supports that the gadolinium complex is well trapped within the nanocapsules. The high payload contrast agent per nanocapsule in the order of approximately  $2.5 \cdot 10^6$  Gd<sup>3+</sup> complexes per capsule results in a capsule relaxivity in the order  $10.75 \cdot 10^6 \text{ mM}^{-1} \cdot \text{s}^{-1}$  per nanocapsule enabling high payloads of contrast agent per available binding site.

Thus, the simple production process (synthesis of these nanocapsules is a single step process), biocompatible and porous shells, stability in physiological fluid like plasma, the high payload and relaxivity, and the potential for functionalization [136, 218] make these contrast agent loaded nanocapsules a promising versatile vehicle for targeted imaging.

## Part B. Gel Approach<sup>\*</sup>

In the first part of this work we applied the principle of inverse miniemulsion to encapsulate various contrast agents in different polymeric shells by using different kinds of monomer 1 (1, 6-hexanediol, dextran, diethylenetriamine). These nanocapsules showed maintained relaxivity or slightly enhanced relaxivity values compared to the commercially available contrast agents and were stable in physiological fluid, plasma. After successful encapsulation of the contrast agent in a polymeric shell, our next target was to use this strategy of encapsulation to enhance the relaxivity to an appreciable extent. Relaxivity value can be enhanced by reducing or slowing down the rotational motion or tumbling motion of the gadolinium complex [33]. To achieve this, attempt was made to use gels as monomer 1 during synthesis and their impact on the relaxivity of encapsulated contrast agent was studied. The choice of using gels as monomer 1 instead of 1, 6-hexanediol, for polymeric shell synthesis was due to the fact that the resultant polymers might provide an environment where the rotational rate may decrease because of the high molecular weight and very viscous nature of gels. Here we have used two types of polymeric gels: polyacrylic acid (PAA) and Poly acrylamide gels (PAAm). These gels differ in their surface charges, PAA is anionic or negatively charged gel and PAAm is nonionic or neutral gel.

The overall aims of this particular study were: (1) To increase the relaxivity by using long chain, high molecular weight gels as monomer-1 during the synthesis of polymeric shells, to provide highly cross linked shell and a viscous environment. (2) To understand whether the presence of charge on the gel affects the morphology of nanocapsules and finally the relaxivity of encapsulated contrast agents.

<sup>\*</sup> The contrast agent loaded nanocapsules, dilution series samples, TEM and DLS data were provided by Dr. Umaporn Paiphansiri, (Prof. Katherina Landfester group) MPI Mainz, the analyses and interpretation of these data along with detailed MRI characterization and analyses were done by the author.

### 3B.1 Materials and Methods

#### 3B.1.1 Synthesis of cross linked gel core encapsulated gadolinium based contrast agent nanocapsules.

Contrast agent loaded nanocapsules in cross linked gel core were synthesized by the following synthesis procedure: For the dispersed phase a known amount (0.625 mg (UPN-5), 1.25 mg (UPN-6), 1.87 mg (UPN-7), 2.5 mg (UPN-8) and 3.125 mg (UPN-3)) of Polyacrylamide (PAAM,  $M_w = 200,000 \text{ g}\cdot\text{mol}^{-1}$ , Aldrich) or (0.625 mg (UPN-9), 1.25 mg (UPN-10), 2.5 mg (UPN-12) and 3.125 mg (UPN-13)) of polyacrylic acid (PAA,  $M_w = 450,000 \text{ g}\cdot\text{mol}^{-1}$  Aldrich), with 15 mg of NaCl (Fischer), were dissolved in 650 mg of contrast agent solution, i.e. Magnevist<sup>®</sup> (Gd-DTPA, Schering AG Berlin, Germany), containing 0.83 mg of fluorescent marker Sulforhodamine. This mixture was then added to a surfactant solution of P (B/E-b-EO) [poly (butylene-co-ethylene) block ( $M_w = 3700 \text{ g}\cdot\text{mol}^{-1}$ ) and a poly (ethylene oxide) block ( $M_w = 3600 \text{ g}\cdot\text{mol}^{-1}$ ) synthesized by anionic polymerization] in 3.75 g cyclohexane (VWR). After intensive pre-stirring at room temperature for 1 h, the inverse miniemulsion was performed by ultrasonifying the mixture in an ice-cooled bath for 3 min with pulses of 10 s and pauses of 10 s at 70% amplitude (Branson sonifier W450 Digital, tip size 6.5 mm). The interfacial polyaddition reaction was carried out at 25°C for 18 h by the addition of a mixture containing 0.14 g monomer-2 [Tolyene-2, 4-diisocyanate (TDI, Fluka)], surfactant P (B/E-b-EO) and cyclohexane. Redispersion in water phase was done by using CTMACl surfactant. 0.5 g of the obtained nanocapsules in the cyclohexane phase was mixed with 18 g of a 0.25 wt. % cetyltrimethyl ammonium chloride (CTMACl) aqueous solution under vigorous stirring at 25 °C for 1 h. Then the redispersion was subjected to an ultrasonification bath for 5 min to avoid the agglomeration of the nanocapsules before further extensively stirring at 25 °C for 12 h.



### **3B.1.2 Stability studies for cross linked Gel encapsulated Magnevist<sup>®</sup> contrast agent loaded nanocapsules in water.**

To study the stability of nanocapsules in water medium, the redispersed contrast agent loaded nanocapsules, redispersed in water, were dialyzed with Amicon membrane (30,000 MW) against water for 3 h, at 2500 rpm in a centrifuge, during this process the water for dialysis was replaced with fresh water after every 1 h. The concentration of  $Gd^{3+}$  in the resultant solution inside the Amicon membrane after dialysis (supernatant solution) was analyzed using ICP-OES. The known concentration of  $Gd^{3+}$  was used for making series of concentrations of  $Gd^{3+}$  solution and  $T_1$  values were then measured by MRI. Relaxivity values were then obtained from the plot of  $1/T_1$  vs.  $Gd^{3+}$  concentration. Details about MRI measurements and data analysis are explained in section (3A.1.7).

### **3B.1.3 TEM and DLS characterization of the nanocapsules**

Transmission electron microscopy (TEM) experiments were performed on a Philips EM400 microscope operating at 80 kV. A drop of diluted aqueous nanocapsules suspension was mounted on 400 - mesh carbon coated copper grids and dried at room temperature.

The size distribution of the nanocapsules was measured by dynamic light scattering technique (DLS) using a zeta nanosizer (Malvern Instruments, U.K.) at a single scattering angle of  $173^\circ$  and a temperature of  $25^\circ C$ .

## **3B.2 Results and Discussion**

### **3B.2.1 DLS studies of the encapsulated nanocapsules**

Sizes of nanocapsules loaded with Magnevist<sup>®</sup>, synthesized by using PAAm gel and PAA gel were measured by DLS. Results are shown in Table 3B.1 and Table 3B.2.

Table 3B.1: Effect of use of PAAm gel amount during synthesis on the diameter of encapsulated Magnevist®.

Sample	Wt. of PAAm gel (mg)	Wt % of PAAm gel for 0.625 g of Magnevist®	Diameter in water (nm) *	PDI
UPN5	0.625	0.1	157	0.19
UPN7	1.875	0.3	209	0.28
UPN8	2.5	0.4	278	0.40
UPN3	3.125	0.5	314	0.42

\*Measured by DLS

The size of Magnevist® encapsulated in nanocapsules having gel content of 0.625 mg is 157 nm. By increasing the amount of gel content from 0.625 mg (0.1 wt %) to 3.125 mg (0.5 wt %) the diameter of the resultant capsule also increases from 157 nm to 314 nm. This behaviour could be explained by the swelling of the nanocapsules. This swelling occurs during the redispersion process and it is caused by the osmotic pressure difference between the nanocapsules and outside water medium [2, 179]. The extent of swelling is directly proportional to the amount of gel content and thus likely cause the increase in capsule diameter with increase in gel content in the aqueous phase. However, for nanocapsules synthesised by using PAA gel the increase in amount of gel shows a different behaviour. As shown in Table 3B.2 the size of Magnevist® encapsulated in nanocapsules having gel content of 0.625 mg is 303.2 nm. By increasing the amount of gel content from 0.625 mg to 3.12 mg there is slight decrease in diameter from 303.2 nm to 264 nm. Although this decrease is not very substantial, this behaviour is opposite to the behaviour of the nanocapsules synthesized using PAAm gel.

Table 3B.2: Effect of PAA gel amount on the diameter of encapsulated Magnevist®.

Sample	Wt of PAA gel (mg)	Wt % of PAA gel for 0.625 g of Magnevist®	Diameter in water (nm) *	PDI
UPN9	0.625	0.1	303.2	0.391
UPN10	1.25	0.2	333.6	0.378
UPN12	2.5	0.4	294.1	0.391
UPN 13	3.125	0.5	264.5	0.030

\*Measured by DLS

In this case, PAA gel is negatively charged and thus increase in the amount of gel might have led to increased cross linking of polymeric network in gel making them progressively rigid [131, 212] and thus the resulting nanocapsules are compact in structure and smaller in size. Thus use of two different types of gels during synthesis shows significantly different effect on size of the nanocapsules.

### 3B.2.2 TEM analysis of the encapsulated nanocapsules

TEM images of the nanocapsules (both in aqueous phase and cyclohexane phase) show the morphologies of the resultant capsules after encapsulation. TEM images of the aqueous phase capsules were taken after dialysis. TEM image of contrast agent loaded nanocapsules synthesized by using PAAm gel is shown in Fig. 3B.1 (A), in this particular case, the nanocapsules were synthesized by adding 2.5 mg (UPN 8) PAAm gel in cyclohexane phase. These nanocapsules were redispersed in water and were dialysed and the TEM image of the washed capsules in aqueous phase is shown in Fig. 3B.1 (B). From these micrographs, it could be clearly understood that these nanocapsules retain their shapes and morphologies after transferring from the cyclohexane phase to the aqueous phase.

Another important point to be noted is even after applying mechanical stress like centrifuge, they retain their morphologies which show the stability of these nanocapsules in water phase.

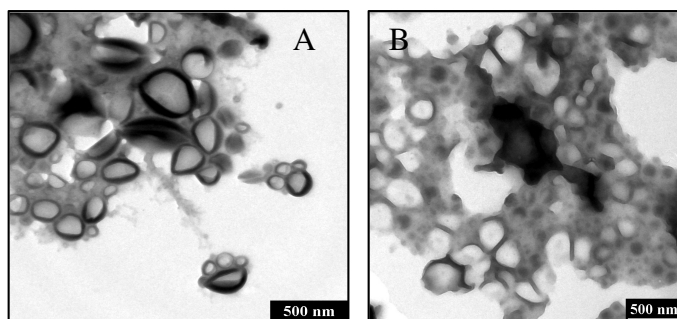


Figure 3B.1: TEM image of Magnevist<sup>®</sup> encapsulated in nanocapsules synthesized by using 2.5 mg of PAAm gel (UPN 8) (A) in cyclohexane phase (B) water phase- *Courtesy Dr.Umaporn Paiphansiri, (Prof. Katherina Landfester group) MPI Mainz.*

TEM image of the nanocapsules synthesized by using PAA gel is shown in Fig. 3B.2. Despite the surface charge difference in these gels, the morphologies and stabilities are found to be similar to the nanocapsules synthesized using PAAm gels. This shows the versatility of this synthesis procedure.

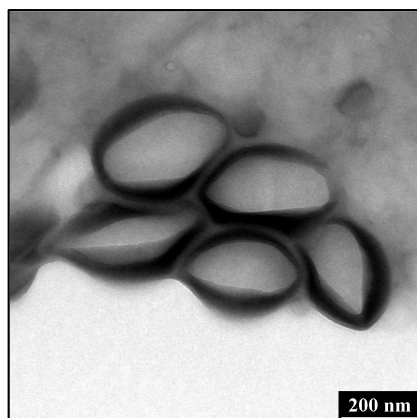


Figure 3B.2: TEM image of Magnevist<sup>®</sup> encapsulated in nanocapsules synthesized by using of 1.25 mg (UPN 10) of PAA gel in cyclohexane phase- *Courtesy Dr.Umaporn Paiphansiri, (Prof. Katherina Landfester group) MPI Mainz.*

### 3B.2.3 MRI Studies of the Magnevist<sup>®</sup> loaded nanocapsules

MRI studies of the Magnevist<sup>®</sup> loaded nanocapsules synthesized by using different gel precursors (PAAm and PAA) were done and the relaxivity values are tabulated in Table 3B.3 and 3B.4 (For detailed data refer appendix A ,Table A.7 and A.8).

Table 3B.3: Relaxivity values of Magnevist<sup>®</sup> encapsulated nanocapsules synthesized by using PAAm gel for synthesis.

Sample	Wt. of PAAm gel (mg)	Relaxivity (mM <sup>-1</sup> ·s <sup>-1</sup> )	R <sup>2</sup>
Magnevist <sup>®</sup>	NA	4.08 ± 0.010	0.999
Encapsulated nanocapsule <sup>*</sup>	NA	4.35 ± 0.035	0.999
UPN5	0.625	8.15 ± 0.023	0.992
UPN7	1.25	7.99 ± 0.05	0.977
UPN8	2.5	7.85 ± 0.030	0.984
UPN3	3.125	8.48 ± 0.05	0.984

<sup>\*</sup> Nanocapsule synthesized using 1, 6 hexanediol as monomer-1.

In the case of PAAm gel, there is clear enhancement in the relaxivity values compared to the non-encapsulated Magnevist<sup>®</sup> solution. The enhancement in the relaxivity value is much more pronounced compared to the Magnevist<sup>®</sup> loaded nanocapsules synthesized using 1, 6 hexanediol. Hexane, 1-6 diol ( $M_w = 118.17 \text{ g}\cdot\text{mol}^{-1}$ ) is a small monomer and PAAm is a long chain polymer ( $M_w = 45,000 \text{ g}\cdot\text{mol}^{-1}$ ). Thus they give different effects. In the case of hexanediol, during synthesis, the active sites are completely consumed resulting in a polyurethane shell having component or components of contrast agent binding on to the inner side of the nanocapsule. But in the case of gels, the aqueous core containing polymer is viscous in nature. Although the polymer can participate in the polyaddition reaction, not every unit reacts with TDI. This could be due to the viscosity and the polymer having many reactive units than the TDI available. This results into polyurethane-co-urea shell surrounding gel core, which is more viscous than that obtained from the first case.

Table 3B.4: Relaxivity values of Magnevist<sup>®</sup> encapsulated nanocapsules synthesized by using PAA gel.

Sample	Wt. of PAA gel(mg)	Relaxivity (mM <sup>-1</sup> ·s <sup>-1</sup> )	R <sup>2</sup>
UPN9	0.625	7.53 ± 0.027	0.972
UPN10	1.25	7.89 ± 0.140	0.975
UPN12	2.5	7.65 ± 0.037	0.981
UPN 13	3.125	7.80 ± 0.031	0.981

Polyacrylamide gels (PAAm) gels are nonionic or neutral gels and have highly cross linked network of polymer chains. PAA is a polyelectrolyte and its characteristic features arise from the electrostatic repulsion between the chains as opposed to the entangled nature of their uncharged counter parts PAAm gel. Each unit of PAA contains carboxylate group, which provides an overall negative surface charge [53, 58, 135]. The total number of charge depends on the number of carboxylate groups.

The presence of gel creates a large number of cross linkages and hydrogen bonding with the water molecules [208] and this might be the reason for the clear enhancement of relaxivity values in the presence of gels. Water molecules travel through the network and are brought in close proximity to the paramagnetic surface. Since PAA [100] contains large number of pendant carboxylate groups, there might be an additional effect of hydrogen bonded water proton to carboxylate groups and contribute to second sphere relaxivity. Thus, by clustering high number of paramagnetic species within small aggregate surrounded by highly crossed network and viscous environment due to the presence of gel may have resulted in enhancement of relaxivity of encapsulated Magnevist<sup>®</sup> contrast agent. Further, gels are macromolecules and some binding of contrast agent and shell of nanocapsules to this macromolecule might have resulted into overall reduction in rotational correlation time ( $\tau_R$ ) and thus might have contributed to increased relaxivity. Thus high molecular weight of gels as compared to diol and more viscous nature may be the reasons for enhancement in relaxivity in later case. However enhancement is seen in both cases i.e. PAA and PAAm gel. Thus charge on gel doesn't seem to have any direct effect on the relaxivity of encapsulated Magnevist<sup>®</sup> contrast agent.

### 3B.3 Conclusion

The use of gels in the synthesis of Magnevist<sup>®</sup> loaded nanocapsules has clearly enhanced the relaxivity values to a very significant extent ( $p < 0.05$ ). These nanocapsules are very stable to mechanical stress and they retain their morphologies even after transferring them to the aqueous phase. The enhancement of relaxivity values is due to the viscous nature of the gels and highly cross linked network of the resultant polymer. Surface charge in the polymers

doesn't seem to affect the relaxivity values. Thus this particular strategy of using gels in the synthesis of polymeric nanocapsules for encapsulating the commercial contrast agents like Magnevist<sup>®</sup> has found to be very effective. However, further characterization is needed to interpret the observed MRI results.

## **Chapter 4**

### **MRI studies of iron-PLLA nanoparticles and iron labeled Mesenchymal stem cells**

Stem cells are a subset of cells that has self-renewing capacity and under appropriate conditions can give rise to several mature cell lineages [191]. There are basically two types of stem cells (A) embryonic stem cells (B) non embryonic stem cells (also called as somatic or adult stem cells). Embryonic stem cells are derived from embryos. Non embryonic stem cell or adult stem cell is thought to be an undifferentiated cell found among the differentiated cells in a tissue or organ that can renew it and can differentiate to yield some or all of the major specialized cell types of the tissue or organ. The primary role of adult stem cells in a living organism is to maintain and repair the tissue in which they are found. In 1950s, researchers discovered that bone marrow contains at least two kinds of stem cells. One population, called hematopoietic stem cells, forms all the types of blood cells in the body. Few years later, a second population, called bone marrow stromal stem cells (also called mesenchymal stem cells) was discovered [81]. In this work we have used MSCs stem cells which are non embryonic in origin. Details about the current research and features of these cells are discussed in the following section.

Mesenchymal stem/stromal cells (MSCs) are multipotent stem cells that have the capability for self-renewal and can differentiate into various mesenchymal tissues, like osteoblasts, myocytes and adipocytes upon appropriate stimulation [43, 73, 80, 141, 186]. Besides bone marrow [81, 59], other sources for obtaining these cells include extra-embryonic tissues such as amniotic membrane [7], placenta [61] and umbilical chord [16, 32]. According to the standard criteria, (set by the International Society for Cellular Therapy, 2004) a specific



phenotype for cultured MSC is marked by the expression of cell surface markers including CD44, CD73, CD90 and CD105 with a concomitant absence of CD45 and CD34 [46]. Isolation of these cells is done by using several methods like ordinary size sieving [85], long term cultivation under specific conditions [142, 193] and fluorescence activated cell sorting (FACS) based approaches [117, 147, 167]. One of the prominent characteristics of MSCs is that they are adherent to tissue culture plastic within 24 to 48 hours. These plastic adherent adult stem cells are routinely used in medical therapies [68, 140]. Recently cellular-based therapies using stem cells are being evaluated as possible treatment options for acute and chronic diseases such as stroke, myocardial infarction, liver diseases, spinal cord injury, Parkinson's disease systems [51, 52, 76, 86, 99, 129, 134, 162, 170]. These cell-based tumor therapies and stem cell-based tissue repair have prompted the need for a high spatial resolution, sensitive imaging tool for the *in vivo* cell tracking [9, 13, 123].

MR imaging has been proven to be an effective tool for the *in vivo* tracking of stem cells because of its non invasive nature and high spatial resolution [11, 13, 87]. In order to detect stem cells using MRI, these cells have to be labeled with MR contrast agents. For this purpose, iron oxide nanoparticles, such as superparamagnetic iron oxide particles (SPIO) have been used, because of their high sensitivity for cell detection and their excellent biocompatibility [18, 51, 92, 96, 198, 199, 203, 213]. SPIO particles are composed of an iron oxide core and a dextran, carboxydextran or starch coat. These iron oxide based contrast agents are easily detectable on  $T_2$ -weighted images, even better on  $T_2^*$ -weighted images due to their susceptibility effects. [10, 14, 183]. Techniques like gradient echo techniques (used for  $T_2^*$ -weighted images), which do not compensate for dephasing are particularly sensitive to detect the presence of iron oxide magnetic nanoparticles in the concentration, as small as  $1\mu\text{M}$ . Also, visualisation of single-cell by using MR micro imaging has been reported by several authors [63]. Other advantages of using iron oxide particles for cell imaging are as follows [30].

- These particles consisting of thousands of iron atoms provide signal change (hypointense) per unit of metal on  $T_2/T_2^*$  weighted images, thus generating contrast even at low concentration ( $\mu\text{mol}$  –  $\text{nmol}$  range), resulting in very high

relaxivities of up to  $200 \text{ mM}^{-1} \cdot \text{s}^{-1}$ . This helps in overcoming the inherent low sensitivity associated with MRI.

- Presence of surface coatings like carboxydextran or dextran, allows the functionalisation of the surface with a wide variety of targeting moieties such as peptides, antibody (derivatives), nucleic acids, or aptamers and thus can be used as a vehicle for target specific binding [118, 137].
- These particles can be easily detected by light and electron microscopy.
- These particles can change their magnetic properties with change in their sizes, so they can be magnetically manipulated. Thus with controllable sizes, their dimensions can match either that of a virus (20– 500 nm), of a protein (5–50 nm) or of a gene (2 nm wide and 10–100 nm long) [24].

The commercially available, clinically approved, iron based SPIO contrast agents for human use include Endorem<sup>®</sup> /Feridex<sup>®</sup>, Resovist<sup>®</sup>, and Combidex<sup>®</sup>. Contrast agents like Feridex<sup>®</sup> and Resovist<sup>®</sup> are mainly used for liver and lymph node imaging. For cell labeling; these SPIO particles can be either bound to the external surface of the cell membrane or internalized into the cytoplasm. Success in the characterization of the iron distribution (cell bound or free) are not widely achieved since mainly  $T_2$ - and  $T_2^*$ -weighted MR images, which enable only qualitative data analysis with signal intensity measurements, are acquired [70, 180, 181]. However studies done by Kuhlpetter et al [103], shows some interesting experiments and results to discriminate free from intracellular /cell bound iron on the basis of  $T_2/T_2^*$  difference. Further, for cell labeling, these contrast agents should combine with different commercially available transfection agents. Complexation of these agents (eg. poly-L-lysine, protamine sulphate etc.) to contrast agents occurs via electrostatic interaction and is an efficient and effective technique for incorporating the SPIO nanoparticles within endosomes, thereby labeling the cells that can be detected by MRI [55, 56]. Several studies have been done to label the cells with these superparamagnetic iron oxide nanoparticles and imaging by MRI. Harald et al. have used MRI for a qualitative and quantitative *in vivo* tracking of injected iron oxide–labeled mesenchymal stem cells (MSC) into rats with acute kidney injury (AKI). Arbab et al. have labeled mesenchymal stem cells (MSCs), hematopoietic (CD34) stem cells and other mammalian cells with ferumoxides–protamine sulfate complexes (Fe-Pro), and have

determined the cellular toxicity, functional capacity, and quantitative cellular iron incorporation using MRI. Amsalem et al. have reported the use of iron-oxide for labeling mesenchymal stem cells in the infarcted myocardium and the effect of SPIO labeling on the MSCs cells [8, 11, 54, 55, 71, 75, 87, 90, 117, 163, 216].

Although, SPIO particles labeled, cell tracking by MRI has several advantages, inability to escape from reticuloendothelial system (RES) and fast clearance rate by phagocytic cells are certain disadvantages. Thus, there is a need to develop advanced magnetic nanoparticle probes for the next-generation molecular MR imaging [91]. Recently, advances have been made in the development of polymeric nanoparticles. These particles are biodegradable, possess good potential for surface modification via chemical transformations, provide excellent pharmacokinetic control, and are suitable for the entrapment and delivery of a wide range of therapeutic agents. Nanoparticles with coating of gelatins, chitosan, poly(lactic-co-glycolic acid) copolymer, polylactic acid, polyglycolic acid, poly(alkylcyanoacrylate), poly(methylmethacrylate), and poly(butyl) cyanoacrylate have been reported in literature [48]. This polymeric coating reduces the immunogenicity, and limits the phagocytosis of nanoparticles by the reticuloendothelial system, resulting in increased blood levels of drug in organs such as the brain, intestines, and kidneys. The US Food and Drug Administration (FDA) have approved biodegradable polymeric nanoparticles, such as PLA and PLGA, for human use [50].

In our present study, attempt has been made to synthesize iron poly-L-lactide nanoparticles (iron-PLLA) by using the miniemulsion technique. The advantage of using miniemulsion process is that it provides the flexibility of controlling the sizes of polymeric nanoparticles, narrow size distribution and surface, potential for functionalization [108, 109, 120]. It has also been reported in literature that these nanoparticles show a favorable cell uptake depending on the toxicity profile of the type of polymer and surfactant used and the available functional group on the surface for functionalization [167]. Polymeric poly-L-lactide, used for the synthesis of these nanoparticles, is biocompatible, biodegradable, and possesses low toxicity *in vivo*. Thus, it is widely used as a drug carrier for the controlled release of

pharmacologically active substances and also used for screws, plates and soft-tissue implants [42, 78, 116, 130, 174, 202].

The overall aims of this study were: (1) To study the MR properties of iron – PLLA nanoparticles and comparison of their relaxivity values with the commercially available contrast agent Resovist<sup>®</sup>. (2) To study the MR properties of Mesenchymal stem cells labeled with Resovist<sup>®</sup> and iron particle MU 119-5zd N3+N4.

## 4.1 Materials

### 4.1.1 Resovist<sup>®</sup>

Ferucarbotran (Resovist<sup>®</sup>, SH U 555 A, Schering AG, Berlin, Germany) is a liver-specific MRI contrast agent. It is the SPIO particle (magnetite-Fe<sub>3</sub>O<sub>4</sub>/maghemite-Fe<sub>2</sub>O<sub>3</sub>) coated with carboxy dextran ( $r_1$  is  $19.4 \pm 0.3 \text{ mM}^{-1}\cdot\text{s}^{-1}$  and  $r_2$  is  $185.8 \pm 9.3 \text{ mM}^{-1}\cdot\text{s}^{-1}$ ). The size of ferucarbotran is 4.2 nm and its hydrodynamic diameter is 62 nm. The carboxydextran coating (27-35 mg/ml with an iron to carboxydextran ratio of 1:1 (w/w)) ensures the aqueous solubility of these micro particles and prevents them from aggregation. It is an aqueous suspension containing 0.5 mol/l of iron, 40 mg/ml mannitol and 2 mg/ml of lactic acid that is adjusted to a pH of 6.5 [150, 173]. For experimental purposes, sample from Batch: 71048C, (Expiry Date 01.2010) was used. 0.9 ml of the sample was used for filtering the sample (Resovist<sup>®</sup> forms cluster during storage, therefore it has to be injected in man through a filter) before preparation of dilution series [167].

### 4.1.2 Phantoms in Agarose gel for MR studies

The sample preparation and design of experiments in agarose gel were done by Ms Gerlinde Schmidtke-Schrezenmeier (Clinic of Dermatology and Allergology of the University Hospital Ulm). A summary of observations from other analytical techniques like FACS, confocal lens microscopy was provided by Ms. Gerlinde Schmidtke-Schrezenmeier. Relevant information is attached in the appendix of this thesis and details of the biological aspect of this work can

be looked in the dissertation titled: “Iron Labeling of Mesenchymal Stem/Stromal Cells for Magnetic Resonance Imaging: Studies on Poly-L-Lactic Acid-Iron Nanoparticles” submitted by Ms Gerlinde Schmidtke-Schrezenmeier.

## 4.2 Methods

### 4.2.1 MRI Experiments

All MRI imaging experiments were performed on a 3T clinical whole body MR unit (Intera; Philips Medical Systems, Best, The Netherlands) by using sense flex M coil.  $T_2$  maps were obtained by using spin echo sequence (TR /Echoes / Flip angle: 1500 ms /8 /90°) and  $T_2^*$  maps were obtained by using gradient echo sequence (TR / Echoes / Flip angle: 500 ms /16 /55°). Basic sequence design and principles of these sequences are explained in chapter-1 (section 1.6.1 and 1.6.2) in a greater detail. For detailed MRI protocol used for  $T_2$  (spin echo) and  $T_2^*$  (gradient echo) measurement refer Appendix C, Table C.1 and C.2.

#### 4.2.1.1 Data Analysis

Signal intensity (SI) and quantitative MR experimental values were determined by using region of interest (ROI). The iron concentration was plotted against  $R_2$  ( $1/T_2$ ) or  $R_2^*$  ( $1/T_2^*$ ). Relaxivity values ( $r_2$ ,  $r_2^*$ ) were obtained from the slopes of the above straight line plots. By visual inspection of the  $T_2$  and  $T_2^*$  maps of the samples, iron labeled cells in the agarose gel were qualitatively and then quantitatively tested. For getting a single value, three experimental values were recorded and mean of these values was taken. All the data presented here are the mean values  $\pm$  standard deviations. These data (both for gradient and spin echo sequence) were acquired with 0.25 mm resolution to get a better signal to noise ratio and were compared with 0.5 mm resolution to confirm the reproducibility of the data.

### 4.3 DLS, ICP and TEM analysis of iron –PLLA nanoparticles

Iron-PLLA particles coated with Poly-L-lactide and loaded with iron oxide and fluorescent dye (PMI) were synthesized using direct miniemulsion technique\* (Detailed synthesis procedure has been given in the Appendix C, section C.1). These iron loaded polymeric nanoparticles were characterized by ICP, DLS and TEM for their iron concentration, particle size and spatial distribution of iron respectively. Table 4.3 gives the details of the different particles and their respective particle sizes and iron content. The values in the table show substantial variation of iron content at almost constant particle size.

Table 4.1: Sample codes and their respective particle sizes and iron content.

Sample	$D_z^*$ [nm]	Amount of iron <sup>**</sup> [mg/ml]
MU119-1zd N2	115	1.01
MU119-5zdz	113	2.35
MU119-5zdz N2	112	2.68
MU128-1zd	149	0.40
MU130-5zdz	113	2.57
MU 119-5zdz N3+N4	134	2.73

\*Determined by DLS; \*\* Determined by ICP

Fig. 4.1 shows the TEM images of these particles, the dark spots within a single particle represents the location of iron oxide particles. From these images, the difference in the spatial distribution of iron particles becomes obvious. These particles with different iron content and distribution were subjected to MRI analysis.

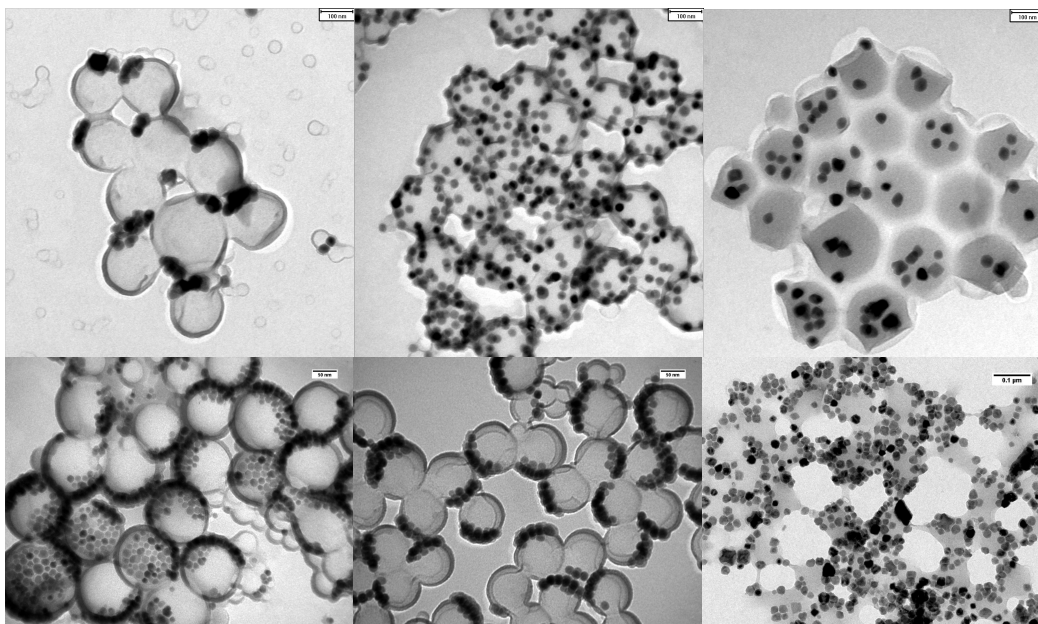


Figure 4.1: TEM images of iron-PLLA nanoparticles with different amount of iron oxide: (A) MU119-1zd N2 (B) MU119-5zdz (C) MU 128-1zd (D) MU 130-5zdz (E) MU 119-5zdzN2 (F) MU 119-5zdz N3+N4 - courtesy Markus Urban.

For the sake of clarity this chapter will be discussed separately under 4 sub-headings.

A: MR studies of iron loaded nanoparticles and Resovist<sup>®</sup>.

B: MR studies of Resovist<sup>®</sup>/PLL labeled cells.

C: Study of kinetic behavior of Resovist<sup>®</sup>/PLL labeled cells by MRI.

D: Study of kinetic behavior of MU 119-5zdz N3+N4 labeled cells by MRI.

## **A: MR studies of different types of iron –PLLA nanoparticles and Resovist<sup>®</sup>**

The main aim of this study is to compare the MR properties of iron–PLLA nanoparticles with that of the commercially available contrast agent Resovist<sup>®</sup>. Another aspect is to understand the effect of iron content, spatial distribution and composition of iron on the MR signal of the iron-PLLA nanoparticles.

### **4A.1 Agarose phantom preparation**

Different iron loaded polymeric nanoparticles were embedded in an iron normalized (phantom samples containing identical amount of iron. Iron concentrations were obtained from ICP-OES) agarose phantom. For comparison, Resovist<sup>®</sup> (as positive reference) was also embedded in a similar way to the agarose phantom. (For detailed procedures for the preparation of these phantoms refer appendix C, Table C.3 and Table C.4). In brief, each phantom was doped with different concentration of iron oxide (0, 6.6, 3.3, 1.66 and 0.833  $\mu\text{g Fe/ml}$ ). Six different particles were imaged in two batches. In the first batch, the agarose phantom was doped with Resovist<sup>®</sup> along with particles MU 119-5zdz, MU 128-zd and MU 119-1zd N2. In the second batch agarose phantom was doped with particles MU 130-5zdz, MU 119-5zdz N3+N4 and MU 119-5zd N2. Particle MU 130-5zdz was loaded with magnetite. All other particles were loaded with wustite. MR images of the phantoms were obtained on a 3T MRI system.

### **4A.2 Results and Discussion**

MRI studies of the iron-PLLA nanoparticles with different iron content and iron composition were done to understand their effect on the relaxation times  $T_2$  and  $T_2^*$ . Table 4A.1 gives the  $T_2$  and  $T_2^*$  values of these particles (including the dilution series with different iron concentration) along with Resovist<sup>®</sup>.



Table 4A.1:  $T_2$  and  $T_2^*$  values of Resovist<sup>®</sup> and Fe loaded particles.

Sample	$T_2^*$ Mean value	$T_2$ Mean value
Resovist <sup>®</sup> 6.6 $\mu\text{g Fe/ml}$	$22.80 \pm 1.25$	$21.93 \pm 0.275$
Resovist <sup>®</sup> 3.3 $\mu\text{g Fe/ml}$	$35.45 \pm 1.52$	$33.61 \pm 0.245$
Resovist <sup>®</sup> 1.66 $\mu\text{g Fe/ml}$	$47.70 \pm 0.62$	$45.88 \pm 2.04$
Resovist <sup>®</sup> 0.833 $\mu\text{g Fe/ml}$	$57.69 \pm 0.44$	$59.02 \pm 1.21$
MU 119-5zdz 6.6 $\mu\text{g Fe /ml}$	$17.46 \pm 0.544$	$60.72 \pm 2.56$
MU 119-5zdz 3.3 $\mu\text{g Fe/ml}$	$29.11 \pm 1.148$	$67.23 \pm 1.11$
MU 119-5zdz 1.66 $\mu\text{g Fe/ml}$	$44.02 \pm 3.42$	$71.42 \pm 0.59$
MU 119-5zdz 0.833 $\mu\text{g Fe/ml}$	$58.42 \pm 4.68$	$69.88 \pm 4.64$
MU 128-zd 6.6 $\mu\text{g Fe/ml}$	$23.31 \pm 1.61$	$24.51 \pm 1.62$
MU 128-zd 3.3 $\mu\text{g Fe /ml}$	$35.30 \pm 2.20$	$39.29 \pm 0.54$
MU 128-zd 1.66 $\mu\text{g Fe /ml}$	$47.16 \pm 2.90$	$55.51 \pm 0.66$
MU 128-zd 0.833 $\mu\text{g Fe /ml}$	$53.29 \pm 0.56$	$69.57 \pm 1.88$
MU 119-1zd N2 6.6 $\mu\text{g Fe/ml}$	$14.02 \pm 1.56$	$55.98 \pm 1.16$
MU 119-1zd N2 3.3 $\mu\text{g Fe /ml}$	$26.03 \pm 2.10$	$69.59 \pm 4.57$
MU 119-1zd N2 1.66 $\mu\text{g Fe /ml}$	$40.87 \pm 0.45$	$75.78 \pm 5.68$
MU 119-1zd N2 0.833 $\mu\text{g Fe /ml}$	$51.02 \pm 6.04$	$79.32 \pm 5.46$
Negative control Agarose 2%	$59.31 \pm 4.01$	$79.55 \pm 13.61$

From the values in Table 4A.1 it can be seen that Resovist<sup>®</sup> along with the three different particles i.e. MU 119-5zdz, MU 128-zd and MU 119-1zd N2 show strong  $T_2^*$  effect. However,  $T_2$  effect is observed only in the cases of Resovist<sup>®</sup> and particle MU 128-zd and is hardly

observed in the cases of particles MU 119-5zdz and MU 119-1zd N2. These observations are supported by  $T_2$  (Fig. 4A.1 (a)) and  $T_2^*$  (Fig. 4A.1 (b)) maps of these phantoms.

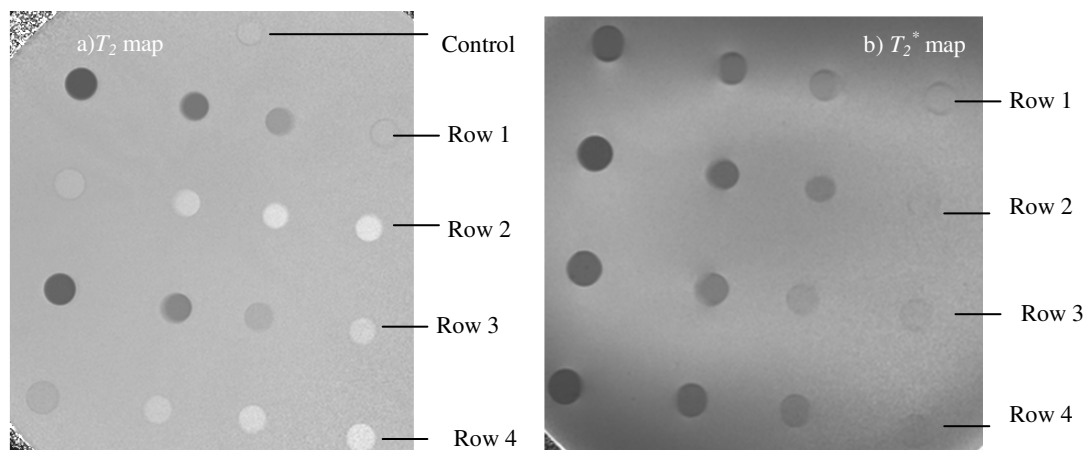


Figure 4A.1: (a)  $T_2$  and (b)  $T_2^*$  map of Resovist® and iron-PLLA nanoparticles in agarose phantom measured at 3T. Row 1: Resovist®; Row 2: MU 119-5zdz; Row 3: MU 128-1zd; Row 4: MU 119-1zd N2. Concentrations used were 6.6  $\mu\text{g Fe/ml}$ ; 3.3  $\mu\text{g Fe/ml}$ ; 1.66  $\mu\text{g Fe/ml}$ ; 0.83  $\mu\text{g Fe/ml}$  from left to right.

As shown in Fig. 4A.1(b), Resovist® (Row 1), particle MU 119-5zdz (Row 2), MU128-1zd (Row 3) and MU 119-1zd N2 (Row 4) show strong  $T_2^*$  effect resulting into significant reduction in signal and thus seen as signal void or dark spots in the map. Besides strong  $T_2^*$  effect, Resovist® and particle MU128-1zd show strong  $T_2$  effect, that can be seen as dark spots in their  $T_2$  maps. However,  $T_2$  map for particle MU119-5zdz (Row 2) and MU 119-1zdz (Row 4) show bright spots (less signal reduction) indicating less  $T_2$  effect. Relaxivity ( $r_2$  and  $r_2^*$ ) of these particles were obtained by plotting relaxation rates ( $R_2$  and  $R_2^*$ ) against their iron concentrations. Graphs showing  $r_2$  and  $r_2^*$  relaxivities are shown in Fig. 4A.2 and Fig. 4A.3 respectively. From Fig. 4A.2, it is observed that the highest relaxivity is shown by particle MU 119-1zdz N2 ( $8.55 \mu\text{g}^{-1} \cdot \text{s}^{-1} \cdot \text{ml}$ ) followed by particle MU 119-5zdz ( $6.39 \mu\text{g}^{-1} \cdot \text{s}^{-1} \cdot \text{ml}$ ).

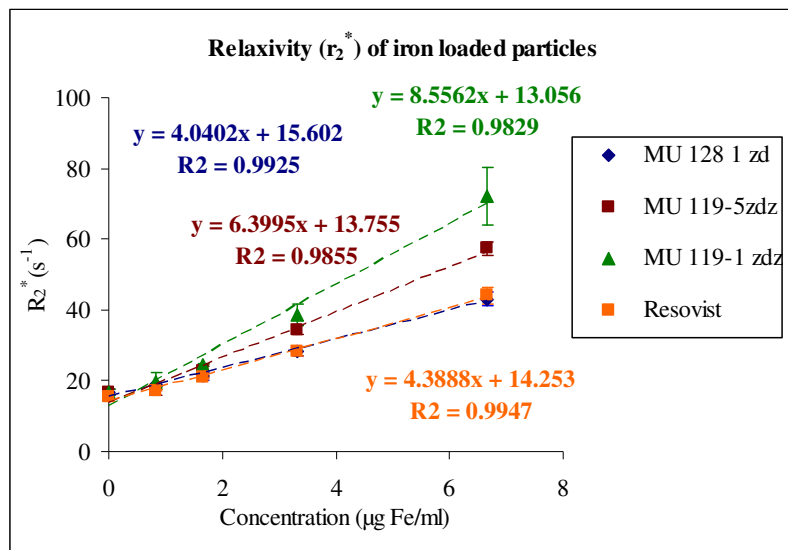


Figure 4A.2: Relaxivity  $r_2^*$  of iron loaded particles. Plot of  $R_2^*$  ( $s^{-1}$ ) against concentration of iron ( $\mu g$  Fe/ml).

The  $r_2^*$  relaxivity of particle MU 128-1zd ( $4.04 \mu g^{-1} \cdot s^{-1} \cdot ml$ ) is close to the relaxivity value of Resovist<sup>®</sup> ( $4.38 \mu g^{-1} \cdot s^{-1} \cdot ml$ ). Fig. 4A.3 show  $r_2$  relaxivity of Resovist<sup>®</sup> and different iron loaded particles. Here the trend is different, relaxivity values of particle MU 119-1zd N2 ( $0.8276 \mu g^{-1} \cdot s^{-1} \cdot ml$ ) and the particle MU 119-5zdz ( $0.507 \mu g^{-1} \cdot s^{-1} \cdot ml$ ) are much lower than that of Resovist<sup>®</sup> ( $4.93 \mu g^{-1} \cdot s^{-1} \cdot ml$ ). However, particle MU 128-1zd ( $4.35 \mu g^{-1} \cdot s^{-1} \cdot ml$ ) shows a relaxivity value that is comparable to that of Resovist<sup>®</sup>.

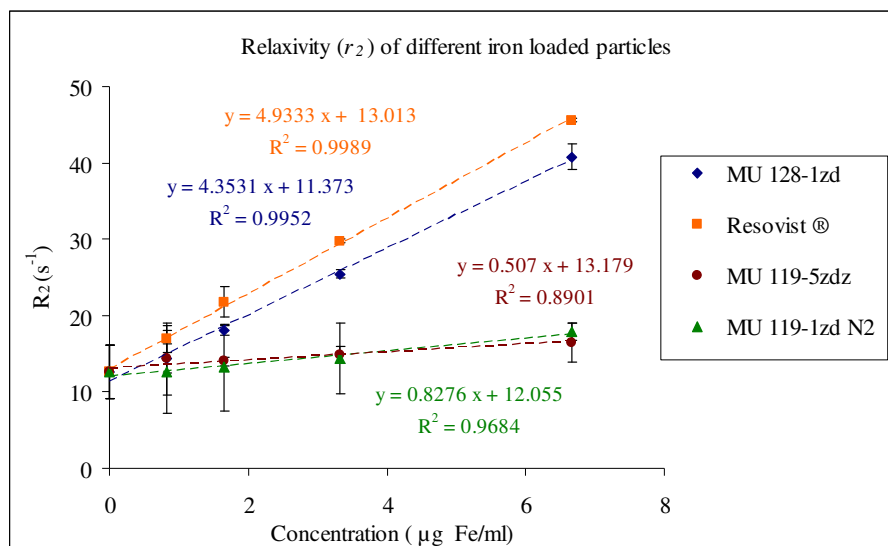


Figure 4A.3: Relaxivity  $r_2$  of iron loaded particles. Plot of  $R_2$  ( $s^{-1}$ ) against concentration of iron ( $\mu g$  Fe/ml).

For MR studies of the remaining 3 particles, similar phantom preparations were done (for details refer appendix C, Table C.4). Resovist® along with the particles MU 130-5zd, MU 119 5zd N3+N4, and MU 119-5zd N2 were embedded in agarose.  $T_2$  and  $T_2^*$  mean values for these particles along with their corresponding standard deviation are shown in Table 4A.2 and values for Resovist® are shown in Table 4A.1.

Table 4A.2:  $T_2$  and  $T_2^*$  values of the second batch of Fe loaded particles.

	$T_2^*$ Mean value	$T_2$ Mean value
MU 130-5zdz 6.6 $\mu\text{g Fe/ml}$	$11.35 \pm 0.65$	$53.01 \pm 1.69$
MU 130-5zdz 3.3 $\mu\text{g Fe/ml}$	$19.65 \pm 1.30$	$58.51 \pm 2.33$
MU 130-5zdz 1.66 $\mu\text{g Fe/ml}$	$32.84 \pm 0.47$	$62.60 \pm 1.87$
MU 130-5zdz 0.833 $\mu\text{g Fe/ml}$	$43.94 \pm 3.14$	$63.42 \pm 3.89$
MU 119 5zdz N3+N4 6.6 $\mu\text{g Fe/ml}$	$19.31 \pm 1.32$	$59.03 \pm 1.82$
MU 119 5zdz N3+N4 3.3 $\mu\text{g Fe/ml}$	$31.87 \pm 1.86$	$63.44 \pm 2.22$
MU 119 5zdz N3+N4 1.66 $\mu\text{g Fe/ml}$	$45.89 \pm 2.11$	$66.31 \pm 2.13$
MU 119 5zdz N3+N4 0.833 $\mu\text{g Fe/ml}$	$54.03 \pm 0.477$	$67.71 \pm 2.23$
MU 119-5zd N2 6.6 $\mu\text{g Fe/ml}$	$18.53 \pm 6.56$	$58.09 \pm 3.63$
MU 119-5zdN2 3.3 $\mu\text{g Fe/ml}$	$29.85 \pm 8.25$	$62.68 \pm 3.44$
MU 119-5zdN2 1.66 $\mu\text{g Fe/ml}$	$43.34 \pm 7.2$	$65.70 \pm 3.45$
MU 119-5zd N2 0.833 $\mu\text{g Fe/ml}$	$53.77 \pm 6.4$	$70.29 \pm 4.67$
Negative Control Agarose 2%	$53.19 \pm 2.3$	$70.42 \pm 4.01$

All these particles show strong  $T_2^*$  but very weak  $T_2$  effect. Particle MU 130-5zdz show the strongest  $T_2^*$  effect.  $T_2$  map of the particles MU 130-5zdz and MU 119 5zdz along with Resovist<sup>®</sup> are shown in Fig. 4A.4(A,B) and  $T_2^*$  map are shown in Fig. 4A.4 (C,D) respectively. Further the  $T_2$  and  $T_2^*$  map acquired for particle MU 119 5zdz N3+N4 along with MU 130-5zdz and MU 119-5zdz are shown in Fig. 4A.5 (A) and Fig. 4A.5 (B) respectively. The signal void (dark spots) as seen in  $T_2^*$  maps are in agreement with the quantitative values shown in Table 4A.2.

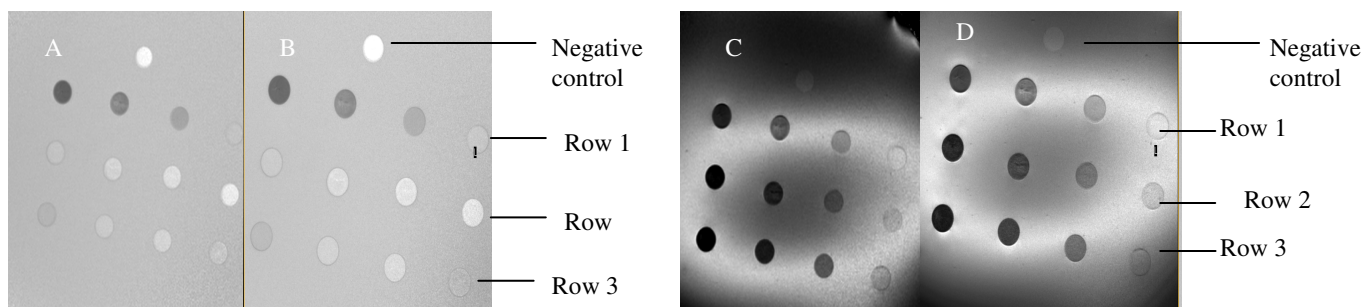


Figure 4A.4:  $T_2^*$  and  $T_2$  maps of Resovist® and iron-PLLA nanoparticles in agarose phantom at 3T (A, C).  $T_2$  and  $T_2^*$  map with 0.5 mm resolution & (B, D)  $T_2$  and  $T_2^*$  map with 0.25 mm resolution. Row 1: Resovist®; Row 2: MU119-5zdz N2; Row 3: MU 130-5zdz.

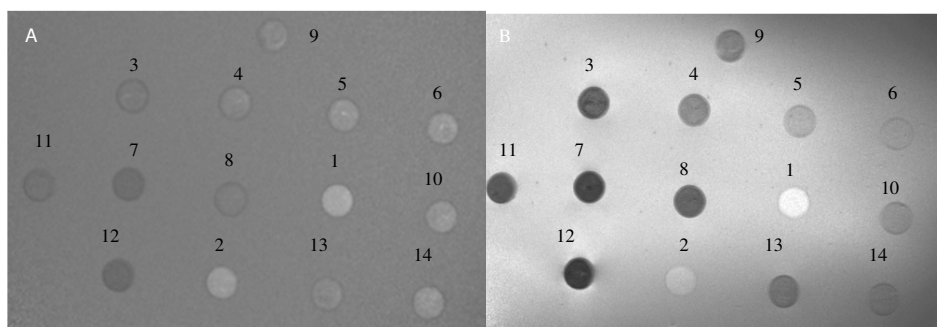


Figure 4A.5: (A)  $T_2$  map (B)  $T_2^*$  map of iron-PLLA nanoparticles with high (>2mg/ml) iron content in agarose phantom at 3T. 1, 2 are signals from negative control. 3, 4, 5, 6 are signal from particle MU 119-5zdz N3+N4 (concentrations used are 6.6, 3.3, 1.66, 0.83  $\mu\text{g Fe/ml}$ ). 7, 8, 9, 10 are signals from particle MU 119-5zdz N2 (concentrations used are 6.6, 3.3, 1.66, 0.83  $\mu\text{g Fe/ml}$ ) and 11, 12, 13, 14 are signals from particle MU 130-5zdz (concentrations used are 6.6, 3.3, 1.66, 0.83  $\mu\text{g Fe/ml}$ ).

Fig. 4A.6 shows the  $r_2^*$  relaxivity of these particles. Particle MU 130 5zdz shows highest  $r_2^*$  relaxivity ( $10.84 \mu\text{g}^{-1}\cdot\text{s}^{-1}\cdot\text{ml}$ ) followed by MU 119-5zdz N2 ( $8.39 \mu\text{g}^{-1}\cdot\text{s}^{-1}\cdot\text{ml}$ ) and MU 119-5zdz N3+N4 ( $5.25 \mu\text{g}^{-1}\cdot\text{s}^{-1}\cdot\text{ml}$ ). The  $r_2^*$  relaxivity values of all these particles are higher than that of Resovist® ( $4.38 \mu\text{g}^{-1}\cdot\text{s}^{-1}\cdot\text{ml}$ , refer Fig. 4A.5). The  $r_2$  relaxivity of these particles are shown in Fig. 4A.7. It can be seen that all the particles show very weak  $T_2$  effect resulting in very low relaxivity values. Particle MU 130-5zdz shows a relaxivity value of  $0.64 \mu\text{g}^{-1}\cdot\text{s}^{-1}\cdot\text{ml}$  followed by MU 119-5zdz N2, and MU 119-5zdz N3+N4 having relaxivity values of  $0.48 \mu\text{g}^{-1}\cdot\text{s}^{-1}\cdot\text{ml}$  and  $0.39 \mu\text{g}^{-1}\cdot\text{s}^{-1}\cdot\text{ml}$  respectively.

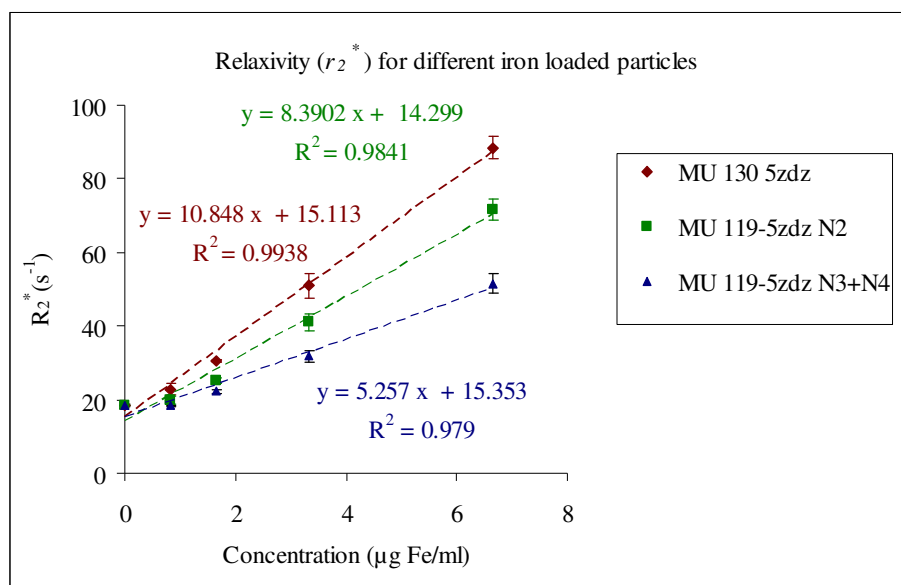


Figure 4A.6: Relaxivity  $r_2^*$  of iron loaded particles. Plot of  $R_2^* (s^{-1})$  against concentration of iron ( $\mu g Fe/ml$ ).

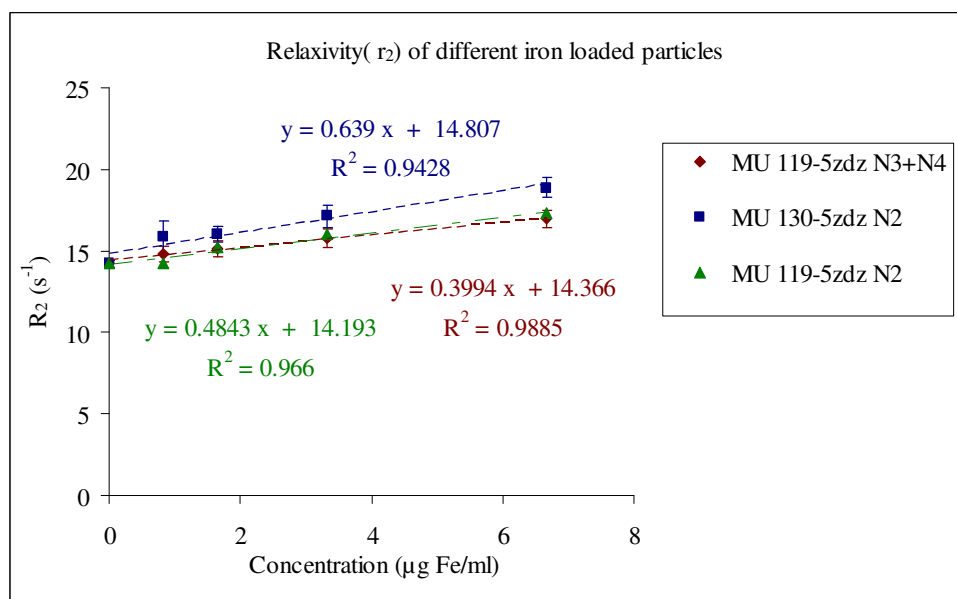


Figure 4A.7: Relaxivity  $r_2$  of iron loaded particles. Plot of  $R_2 (s^{-1})$  against concentration of iron ( $\mu g Fe/ml$ ).

Summary of the relaxivity values for all the six particles along with that of Resovist<sup>®</sup> are shown in Table 4A.3. Here the unit for relaxivity has been converted from  $\mu\text{g}^{-1}\cdot\text{s}^{-1}\cdot\text{ml}$  to  $\text{mmol}^{-1}\cdot\text{s}^{-1}\cdot\text{L}$  or  $\text{mM}^{-1}\cdot\text{s}^{-1}$ . The conversion was carried out by multiplying the relaxivity value in  $\mu\text{g}^{-1}\cdot\text{s}^{-1}\cdot\text{ml}$  by 56 g/mol (atomic mass of Fe).

Table 4A.3: Summary of all the relaxivity values.

Particles	$r_2$ relaxivity( $\text{mM}^{-1}\cdot\text{s}^{-1}$ )	$r_2^*$ relaxivity( $\text{mM}^{-1}\cdot\text{s}^{-1}$ )
MU 130-5zdz	35.78	607.4
MU 119-5zdz N2	27.04	469.84
MU 119-1zd N2	46.25	478.8
MU 119-5zdz	28.39	357.84
MU 119-5zdz N3+N4	22.4	294
MU 128-1zd	243.6	226.2
Resovist <sup>®</sup>	276.08	245.28

In order to understand the MR behavior of these particles and their effect on  $T_2$  and  $T_2^*$  relaxation times it is important here to discuss in brief about  $T_2$  and  $T_2^*$  relaxation times and effect of superparamagnetic particles on these relaxation times (Details can be seen in section 1.2.2).  $T_2$  or spin-spin relaxation time includes only irreversible causes of a loss of phase coherence (dephasing) of the net magnetisation vectors which add up to make  $M_{xy}$ . These spin-spin interactions are at the atomic and molecular levels, in which spins affect each other by their individual oscillating magnetic fields. This changes their frequency of precession (according to the Larmor equation (section 1.1), and they move out of phase.  $T_2^*$  is like  $T_2$ , but with an extra dephasing effects.  $T_2^*$  includes dephasing caused by magnetic field inhomogeneities and susceptibility effects as well. These also cause variations in the magnetic field experienced by proton spins. This changes their frequency of precession even more, and they move out of phase much faster resulting in a faster loss of signal. The  $T_2^*$  relaxation time is always shorter than the  $T_2$  relaxation time (see Table 4A.1 and 4A.2). Dephasing effects included in  $T_2^*$  (not in  $T_2$ ) are reversible in some circumstances by the spin echo pulse sequence [84]. The presence of superparamagnetic particles introduces local magnetic field



inhomogeneties in the system. As protons diffuse through the microscopic magnetic field inhomogeneties, the protons loose phase coherence due to their Brownian random walks through the inhomogeneous magnetic field. This, in turn, dramatically shortens  $T_2$  relaxation time. Owing to the predominant  $T_2$  effect, these “ $T_2$  agents” usually create hypointense contrast on conventional spin-echo MR sequences. In addition, even without the movement of water, the magnetic field inhomogeneties and therefore heterogeneity of frequencies within an imaging voxel can affect the signal intensity (in gradient echo images) by causing intravoxel dephasing. On gradient-echo images, where  $T_2^*$  effects dominate, these particles induces an even larger hypointense contrast effect (see Fig 4A.1 (b), 4A.4 (C, D) & 4A.5 (B)). The microscopic inhomogeneities in the magnetic field induce a rapid dephasing of diffusing water protons, including those diffusing some distance away. This in turn leads to a “blooming effect,” that is, an amplification of signal changes. Also it has been reported that  $T_2$  relaxation effect of SPIO particles depends on its spatial distribution: sparsely distributed iron oxide shows a decreased  $T_2$  relaxation [47, 181].

Following the above discussion, behavior of these particles and difference in their effect on the relaxation rates and hence on the relaxivity could be explained on the basis of their iron content and the difference in their iron composition. On the basis of iron content, these particles can be divided into 3 categories: (1) Iron content < 1mg iron/ml (2) Iron content = 1mg iron/ml (3) Iron content > 1mg iron/ml. Particle belonging to the first category i.e. MU 128-1zd with an iron content of 0.40 mg Fe/ml show MR properties similar to Resovist<sup>®</sup> which can be seen from its relaxivity values in Table 4A.3. Thus this particle shows strong  $T_2$  and  $T_2^*$  effect. Particle belonging to the second category, MU 119-1zd N2, with an iron loading of 1 mg Fe/ml show strong  $T_2^*$  effect and less pronounced  $T_2$  effect. Particles belonging to the third category i.e. iron content varying from 2.35 to 2.73 mg Fe/ml show very strong  $T_2^*$  effect, with particle MU130-5zdz showing the highest relaxivity among all the particles. Besides being the particle with highest iron content, the other factor that makes MU130-5zdz different from the other particles is that this particle is loaded with magnetite instead of wustite [167]. Magnetite seems to have better magnetic properties compared to wustite. Thus the composition of iron oxide also appears to affect the MR properties of these particles. However,  $T_2$  effect in case of all these particles is less pronounced.

### 4A.3 Conclusion

From the MRI studies of different iron loaded PLLA particles, it is clear that the, iron content along with iron composition seems to be effective parameter to influence these relaxivity values. Although, a relationship between the MR properties and the particle characteristics has been established, further detailed studies under more controlled conditions are needed to understand this relationship more clearly. Further, detail experiments are needed to understand the effect of spatial distribution of iron on the relaxation rates.

## B: MR Imaging of Resovist<sup>®</sup>/PLL labeled MSCs cells

The aim of this particular study is to detect the lowest possible number of Resovist<sup>®</sup> labeled cells which can give distinguishable MR signal as compared to the unlabeled cell.

### 4B.1 Agarose phantom preparation

MSCs (Sark02p11) were incubated for 24 h with Resovist<sup>®</sup>/PLL (50 µg Fe and 0.75 µg Poly-L-Lysine (PLL) per ml of incubation medium). MSCs were then trypsinated, washed, stained with trypanblue, and counted in a Neubauer chamber. Defined cell numbers were dissolved in 0.5 ml of PBS then added and homogenized in 2 ml agarose at about 42°C. The agarose sample was then poured into the holes of the mother phantom. Different samples were prepared in concentrations of 250 000, 125 000, 625 00, 31 250, 15 600 and 7800 cells/ml of agarose along with negative control of 250 000 unlabeled cells and positive control of Resovist<sup>®</sup> [167] (for detailed procedure for the preparation of this phantom, refer appendix C, Table C.5).

Further to test the sensitivity of the method, an experiment with focus on low cell number was done. In this case phantom setting was generated by using sample hole with bigger diameter. For phantom preparation, Resovist<sup>®</sup> was used as positive control. Concentrations of Resovist<sup>®</sup>/PLL labeled cells used were 32 000, 16 000, 8 000 and 4 000 cells /ml and negative

control consisting of 32 000 unlabeled cells (for detailed procedure for the preparation of this phantom, refer appendix C, Table C.6).

## 4B.2 Results and Discussion

MR measurements were done on a 3T instrument as explained in section 4.2.1. Resovist<sup>®</sup> (without cells) show strong  $T_2/T_2^*$  effect which can be confirmed by the dark spots seen in  $T_2^*$  (Fig. 4B.1 (B)) and  $T_2$  (Fig. 4B.1 (C)) maps. For Resovist<sup>®</sup>/PLL labeled cells, strong  $T_2^*$  effect can be seen for the cells from 250 000 down to 15 600 cells/ml. Discrete  $T_2$  effect is also seen for cell samples till 15 600 cells/ml.

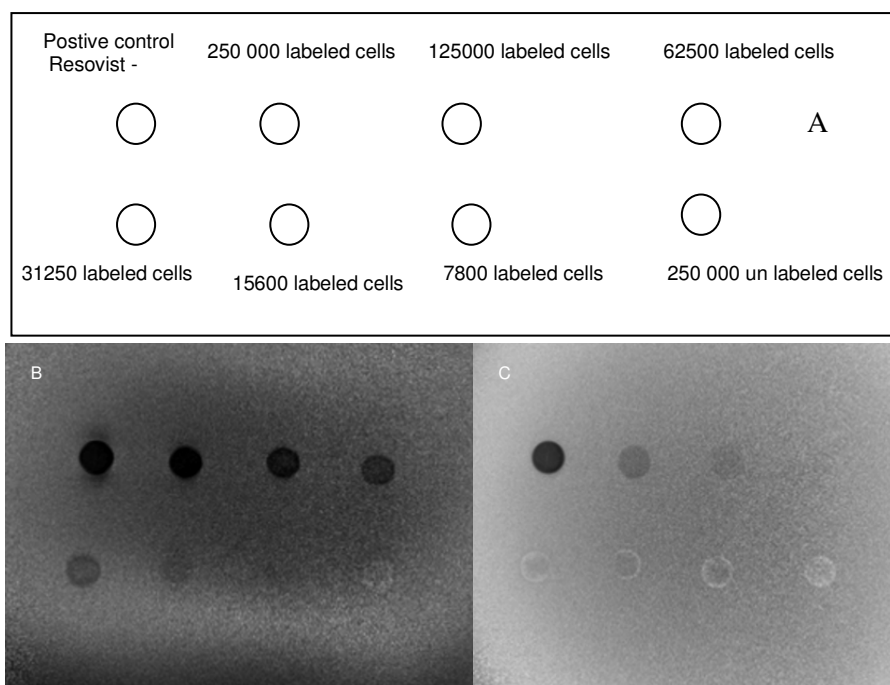


Figure 4B.1: (A) Phantom setting (B)  $T_2^*$  map (C)  $T_2$  map of Resovist<sup>®</sup>/PLL labeled MSC cells at 3T in concentration of 250 000, 125 000, 62 500, 31 250, 15 600 and 7 800 cells per ml agarose.

The value of  $T_2^*$  increases with decrease in cell number as shown in Fig. 4B.2. A very strong  $T_2^*$  effect can be seen for the cell number from 250 000 down till 15 600.  $T_2$  values also follow the same trend i.e. decrease in signal with increase in cell number for the cells from 250 000 down till 312 500 cells/ml. However in case of lower cell numbers of 15 600 and 7 800 this

trend was not observed. Also in case of negative control and probes with 15 600 and 7800 cells,  $T_2$  values are lower than  $T_2^*$  [84]. This observation could be because of other factors, as according to MR physics  $T_2$  values are always higher than  $T_2^*$  values. Further in case of  $T_2^*$ , lower cell number probe appear quite homogeneous on  $T_2^*$  map in contrast to  $T_2$  where they look cloudy or inhomogeneous in appearance.

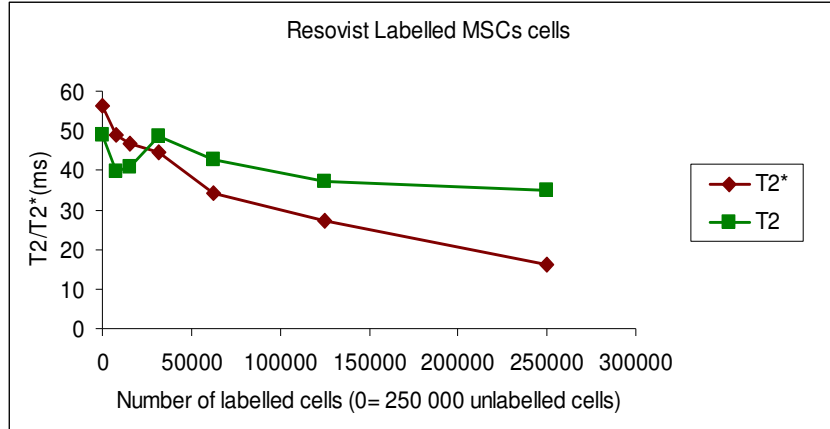


Figure 4B.2: Graph of  $T_2$  and  $T_2^*$  (ms) versus Resovist<sup>®</sup>/PLL labeled cells in concentration of 7800-250 000 per ml agarose 2%. 0 indicates negative control of 250 000 unlabeled cells.

$T_2$  and  $T_2^*$  map for the phantom with lower cell numbers are shown in Fig. 4B.3 (B, C). The cluster pattern can be seen for the labeled cells. However this pattern is not observed in the case of negative control with unlabeled cells. Further, signals from Resovist<sup>®</sup> also show inhomogeneous distribution indicating a “cluster pattern”. It is known that Resovist<sup>®</sup> forms cluster during storage so it has to be injected through filter only [167].

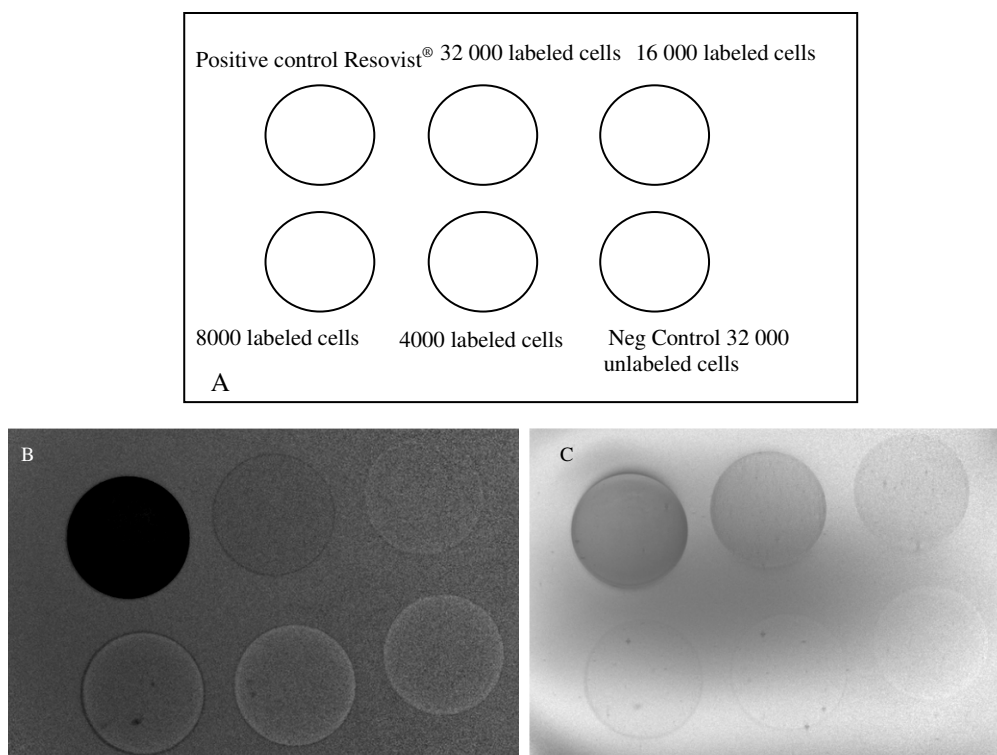


Figure 4B.3:  $T_2$  and  $T_2^*$  map of Resovist<sup>®</sup>/PLL labeled cells measured at 3T (A) phantom setting (B)  $T_2$  map with 0.25 mm resolution and (C)  $T_2^*$  map with 0.25 mm resolution.

### 4B.3 Conclusion

MR studies of Resovist<sup>®</sup>/PLL labeled cells show that cells as low as 15 600 cells/ml can be detected by MRI and these cells show strong  $T_2^*$  effect and distinguishable  $T_2$  effect. Distribution of iron in the cells was found to be inhomogeneous and cell cluster were seen down to 4000 cells/ml in the labeled cells.

### C: Study of kinetic behavior of Resovist<sup>®</sup>/PLL labeled cells by MRI

Aim of this study was to know whether the intracellular iron particles can create a MR signal distinguishable from unlabeled cells after particle removal (particle removal means removal of iron source from the medium. For this purpose everyday 1/3 of the incubation medium was substituted to remove free iron for this experiment). Further test was done to distinguish MR

signal difference between high (lower cell division rate) and low (higher cell division rate) density seeded cells after particle removal.

#### 4C.1 Phantom preparation in agarose

For phantom preparation, 200 000 and 50 000 MSCs cells/ml were incubated with Resovist<sup>®</sup>/PLL for 24 h. The cells were dissolved in 0.5 ml PBS and then added to 1 ml of 2% agarose. Agarose sample was then poured into the holes of the “phantom mother”. For positive control Resovist<sup>®</sup> (7 µg iron/ml) and for negative control 200 000 unlabeled MSCs cells were used (detailed procedure for the preparation of this phantoms is available in the appendix C, Table C.7). This phantom of 0 h was characterized by MRI. Further these 200 000 and 50 000 cells were then subjected to different stimuli for division resulting into high density seeded cell (HDS) and low density seeded cell (LDS) seeded cells. Test phantom samples of 200 000 and 50 000 cells were created for both low and high density cells and were characterized by MRI at time intervals 24, 48 and 96 h (for detailed procedure on preparation of these phantoms, refer appendix C, Table C.8 and C.9). At 144 h, samples with only low density seeded cells were available and thus only these samples were characterized by MRI.

#### 4C.2 Results and Discussion

$T_2$  and  $T_2^*$  maps obtained from the MR measurements of phantom at 0 h are shown in Fig. 4C.1. Strong  $T_2^*$  effect can be seen for both 200,000 labeled cells and 50,000 labeled cells as compared to the negative control (unlabeled cells). Further 200,000 labeled shows stronger effect than 50 000 labeled cells. This can be more clearly seen from the values shown in Table 4C.2.  $T_2^*$  values for the 200,000 labeled cells is 25.00 ms while for the 50 000 labeled cells it is 53.75 ms. Further 200,000 labeled cells show similar  $T_2^*$  effect as shown by positive control Resovist<sup>®</sup> (22.54 ms). These observations suggest that there is an exponential relationship between concentration and intensity.

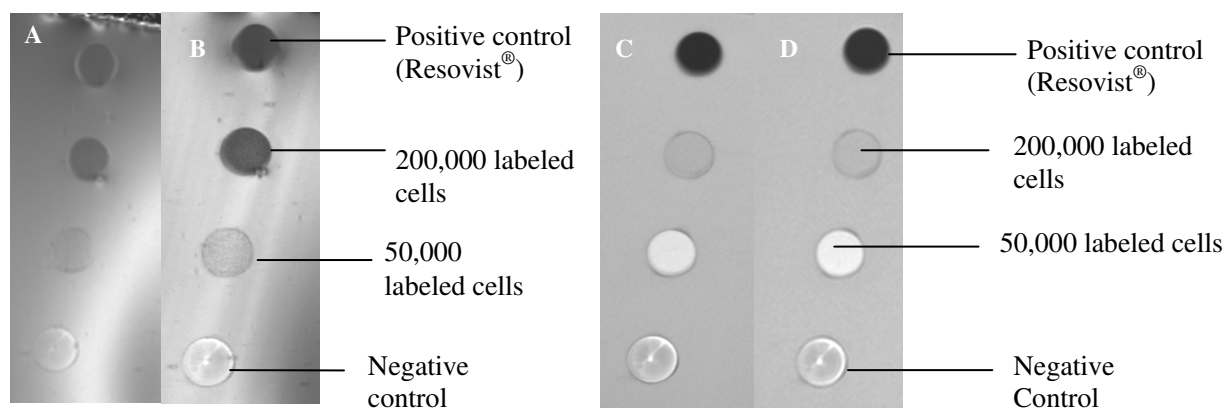


Figure 4C.1:  $T_2^*$  map (A) 0.5 mm (B) 0.25 mm resolution and  $T_2$  map (C) 0.5 mm (D) 0.25 mm for phantom at 0 h.

$T_2$  effect can be seen in case of 200 000 labeled cells (56.16 ms) whereas  $T_2$  effect in case of 50 000 cells is undistinguishable from the unlabeled cells ( $T_2$  values 69.16 ms & 70.81 ms respectively).  $T_2$  and  $T_2^*$  maps for the cell phantom after 24, 48, 96 and 144 h are shown in Fig. 4C.2, 4C.3 & 4C.4 respectively.

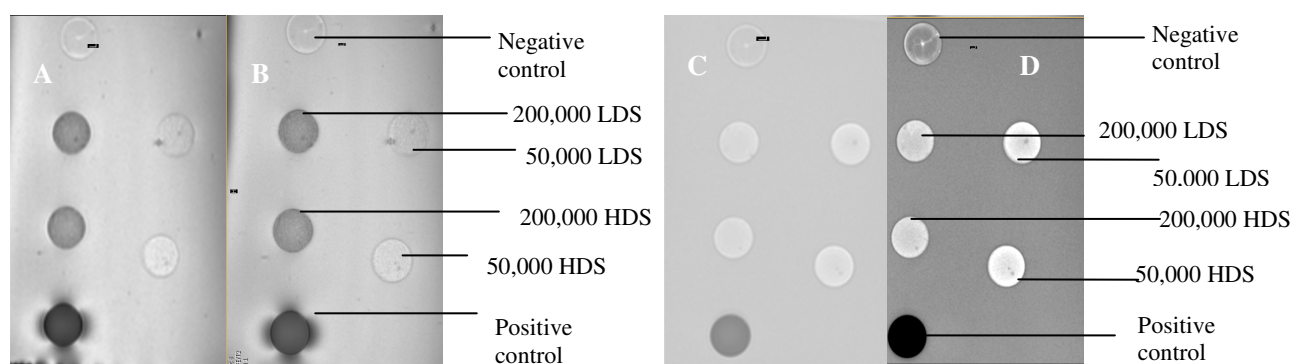


Fig. 4C.2:  $T_2^*$  map (A) 0.5 mm (B) 0.25 mm resolution and  $T_2$  map (C) 0.5 mm (D) 0.25 mm for phantom at 24 h.

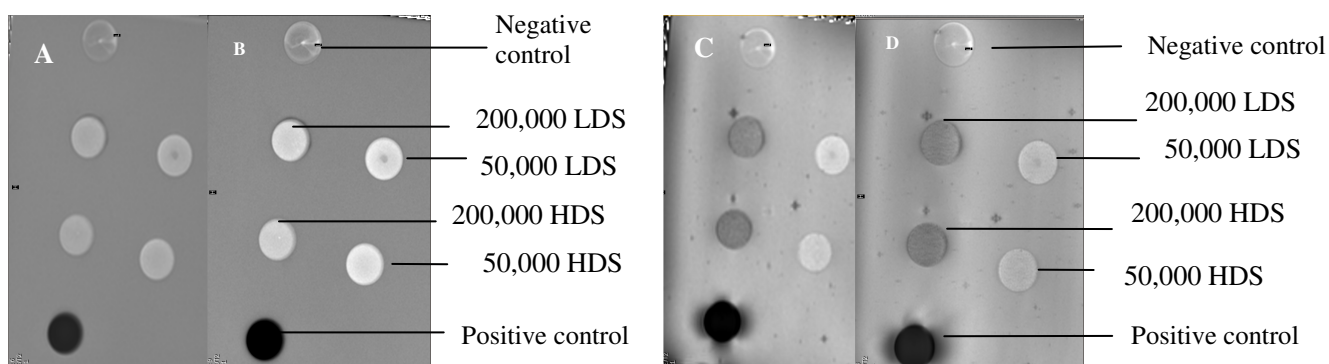


Figure 4C.3:  $T_2$  map (A) 0.5 mm (B) 0.25 mm resolution and  $T_2^*$  map (C) 0.5 mm (D) 0.25 mm for phantom at 48 h

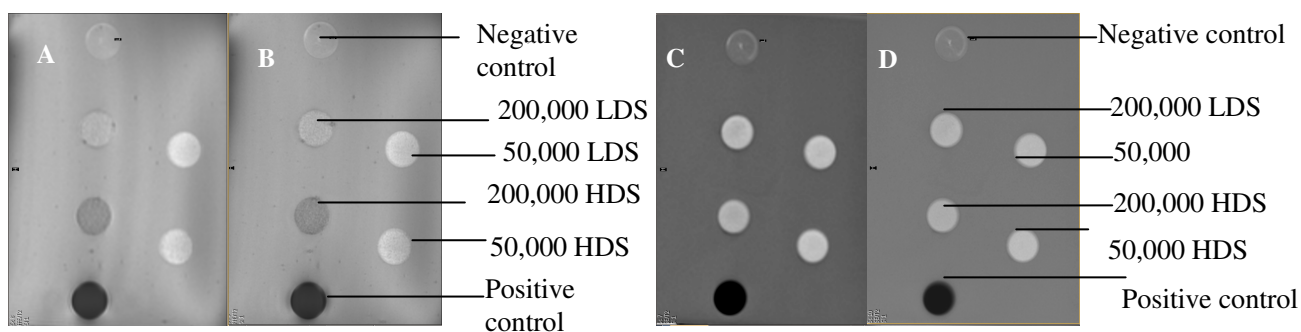


Figure 4C.4:  $T_2^*$  map (A) 0.5 mm (B) 0.25 mm resolution and  $T_2$  map (C) 0.5 mm (D) 0.25 mm for phantom at 96 h.



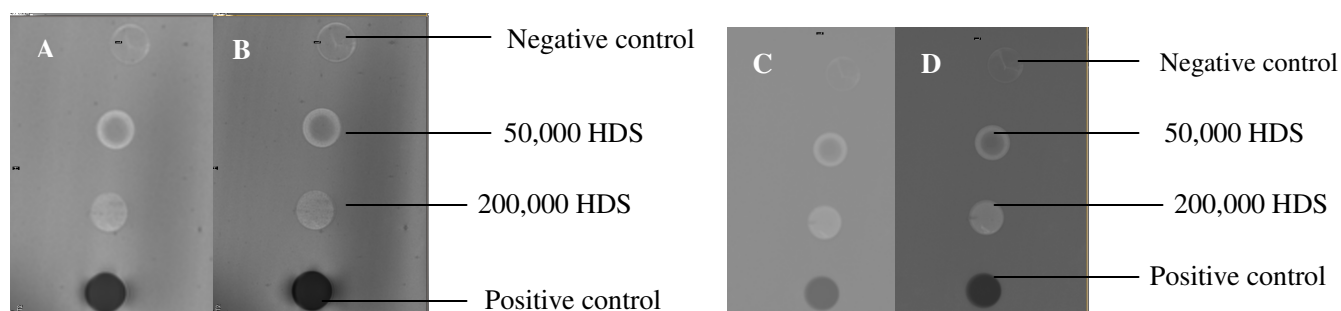


Figure 4C.5:  $T_2^*$  map (A) 0.5 mm (B) 0.25 mm resolution and  $T_2$  map (C) 0.5 mm (D) 0.25 mm for phantom at 144 h.

Table 4C.1 shows quantitative  $T_2^*$  values from 0 h to 144 h along with their standard deviations. From the quantitative values shown in Table 4C.1 for  $T_2^*$ , it is clear that  $T_2^*$  effect is seen until 96 h after particle removal in case of 200 000 labeled cells. Signal difference between high density and low density seeded 200 000 cells becomes significant for the 94 h sample. However, no difference in the signal and hence in the quantitative values, is observed in the case of 50 000 low and high density seeded cells. For the 144 h sample, only samples with low density were available and there was clear  $T_2^*$  effect for the cell numbering 200 000 even at 144 h of particle removal. Further,  $T_2^*$  values of labeled cells were always lower than that of the unlabeled cells (negative control) for 200 000 cells till 144 h and for 50 000 cells till 96 h after Resovist<sup>®</sup>/PLL particle removal. However,  $T_2$  data does not show much deviation from the negative control values and also did not show any trend with time. Thus,  $T_2^*$  can be used as parameter for tracking these Resovist<sup>®</sup> labeled cells for further in vivo studies.

Table 4C.1:  $T_2^*$ (ms) values for Resovist<sup>®</sup> /PLL labeled MSCs. Kinetic study was done at regular time intervals after particle removal.

	0 h	24 h	48 h	96 h	144 h
Positive control (Resovist <sup>®</sup> )	22.5 ± 0.2	24.2 ± 0.7	12.5 ± 0.3	17.0 ± 0.1	19.5 ± 0.7
200 000 HDS	25.0 ± 0.5	43.91 ± 0.3	43.49 ± 0.5	49.5 ± 0.1	64.09 ± 0.1
200 000 LDS	25.0 ± 0.5	41.24 ± 0.1	47.62 ± 0.1	60.8 ± 1.5	NA
200 000 unlabeled cells	66.8 ± 5.1	61.1 ± 3.8	66.79 ± 5.3	69.9 ± 7.7	67.9 ± 8.0
50 000 HDS	50.8 ± 2.8	60.9 ± 0.2	62.93 ± 0.7	74.0 ± 1.0	77.7 ± 0.2
50 000 LDS	50.8 ± 2.8	57.5 ± 0.5	65.02 ± 0.2	75.8 ± 1.5	NA

Table 4C.2:  $T_2$  (ms) values for Resovist<sup>®</sup> /PLL labeled MSCs. Kinetic study was done at regular intervals after particle removal.

	0 h	24 h	48 h	96 h	144 h
Positive control (Resovist <sup>®</sup> )	24.7 ± 0.2	23.0 ± 2.4	11.05 ± 0.9	17.1 ± 0.1	18.4 ± 0.5
200 000 HDS	56.1 ± 1.1	66.8 ± 3.8	74.8 ± 2.8	80.9 ± 2.9	79.5 ± 3.5
200 000 LDS	56.1 ± 1.1	66.5 ± 3.5	76.7 ± 2.7	83.4 ± 3.4	NA
200 000 unlabeled cells	70.8 ± 8.1	63.8 ± 3.1	70.7 ± 7.2	69.5 ± 4.5	64.6 ± 3.3
50 000 HDS	69.1 ± 2.1	70.6 ± 3.6	77.4 ± 4.4	86.2 ± 4.2	77.7 ± 5.7
50 000 LDS	69.1 ± 2.1	71.1 ± 3.1	78.1 ± 2.1	86.4 ± 4.4	NA

Summary of the trend observed during kinetic studies of Resovist<sup>®</sup> /PLL labeled MSCs cells after particle removal are shown in Fig. 4C.6 for  $T_2^*$  and Fig. 4C.7 shows for  $T_2$ .

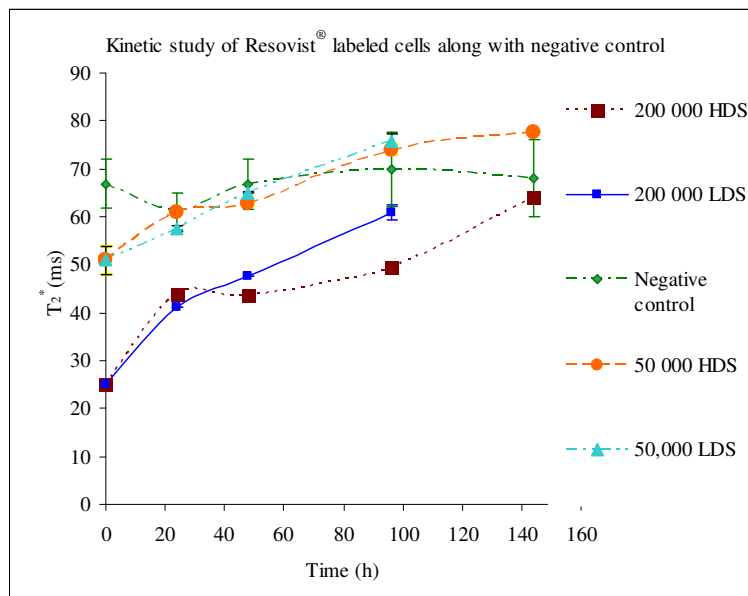


Figure 4C.6: Graph showing summary of  $T_2^*$  behavior of kinetic study of labeled and unlabeled cells at different time interval.

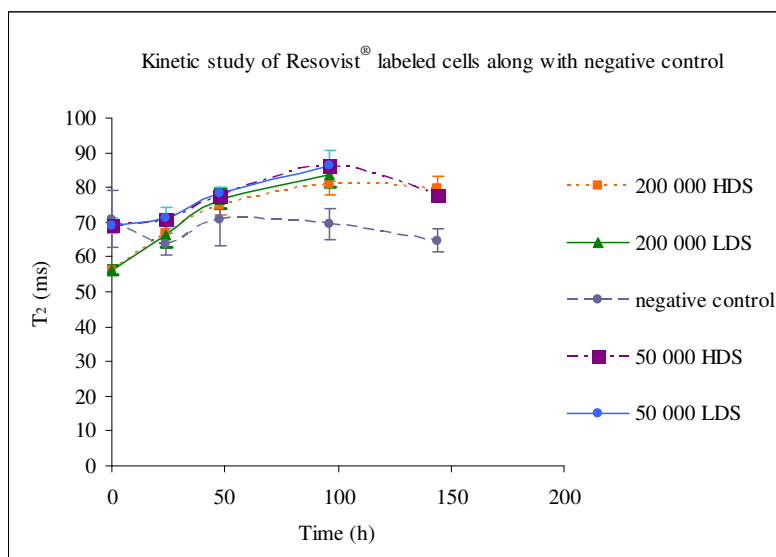


Figure 4C.7: Graph showing summary of  $T_2$  behavior of kinetic study of labeled and unlabeled cells along with Resovist<sup>®</sup> at different time interval after particle removal.

### 4C.3 Conclusion

From the above kinetic studies, we can conclude that the cells labeled with Resovist<sup>®</sup> /PLL particles can be easily detectable by MRI even at 144 h after particle removal. However, signals and quantitative values obtained from  $T_2^*$  measurements are more specific and clearly distinguishable from the unlabeled cells. Thus,  $T_2^*$  can be used as parameter for tracking these Resovist<sup>®</sup> labeled cells for further in vivo studies.

### D: Study of kinetic behavior of MU 119-5zdz N3+N4 labeled MSCs cells by MRI

Among several different particles (explained in section 4A.1), initial cell studies done with particle MU119-1zdN2 resulted into no change in MR signal intensities as compared to unlabeled cells. Cell studies done with particle MU119-5zdz generated decent  $T_2$  and  $T_2^*$  effect but only a little amount of this particle was available. These encouraging results initiated the synthesis of a bigger batch (MU 119-5zdzN3+N4) with particle specifications in the same range sufficient for multiple experiments [167]. In this study, the aim is to test the imaging properties of MU 119-5zdz N3+N4 labeled MSCs at 0 h, 24 h and 96 h after removal of the iron particle containing medium in order to see whether intracellular iron is still sufficient to give a MR signal. MR signal from unlabeled cells was used for comparison. Further, from fluorescent study, it was found that difference in the fluorescent activity when seeding in high density (lower cell division rate) and low cell density (higher cell division rate) can be seen at 96 and 144 h and not before that. Thus MR signal between high and low density seeded cells after particle removal was also tested at 96 h by MRI.

#### 4D.1 Agarose Phantom preparation

For time points 0 h and 24 h, agarose phantoms were created with a negative control (200 000 unlabeled MSC cells and 50 000 unlabeled MSC cells), and samples with 200 000 and 50 000 labeled cells. At time point 96 h, phantom samples of 200 000 and 50 000 cells were created

for both high density and low density seeded cells (for detailed procedures for the preparation of these phantoms, refer Appendix C.10)

## 4D.2 Results and Discussion

$T_2^*$  values obtained for these samples at different time intervals after particle removal are shown in Table 4D.1 and  $T_2$  values are shown in Table 4D.2.

Table 4D.1:  $T_2^*$  values (ms) of MU 119-5zdz N3+N4 particle labeled MSCs at different time intervals after particle removal.

	0 h	24 h	96 h HDS	96 h LDS
200 000 labeled cells	10.36	22.04	34.61	41.92
50 000 labeled cells	32.68	51.72	56.83	60.82
200 000 unlabeled cells	69.84	68.92	NA	NA
50 000 unlabeled cells	51.66	70.18	NA	NA

From the Table 4D.1 it has been observed that there is reduction in  $T_2^*$  values after 24 h as compared to the 0 h for both 200 000 labeled cells and 50 000 labeled cells. Further reduction in  $T_2^*$  value for 50 000 is less than 200 000 cells. Between high and low density seeded cells at 96 h, 200 000 HDS show more reduction in  $T_2^*$  values (stronger signal) as compared to 200 000 LDS cells. Similar trend was observed for 50 000 HDS and LDS cells. Further, signal reduction was more for 200 000 cells in both HDS and LDS condition as compared to 50 000 cells. Negative control at 0 and 24 h for 200 000 cells show similar effect but some difference is seen for negative control of 50 000 cells for 0 h and 24 h. However the reasons for not getting reproducible values in case of negative controls are not very clear but it is assumed that in case of unlabeled cells, water protons are the only source of signal, thus slight variation in amount of aqueous solution (water or phosphate buffer (PBS)) during preparation can affect signal and hence  $T_2$  and  $T_2^*$  values. (Further studies are needed to understand this discrepancy).

Table 4D.2:  $T_2$  values of Iron / PLLA Particle labeled MSCs at different time intervals ( $T_2^*$  value of Agarose is 68.89 ms and  $T_2$  value of agarose is 91.77 ms).

	0 h	24 h	96 h HDS	96 h LDS
200 000 labeled cells	13.90	40.65	63.69	72.46
50 000 labeled cells	36.49	68.49	79.36	84.74
200 000 unlabeled cells	94.33	86.95	NA	NA
50 000 unlabeled cells	62.89	94.33	NA	NA

From the Table 4D.2 it can be seen that  $T_2$  effect also follow the similar trend as observed in case of  $T_2^*$  effect.  $T_2$  effect shown by 200 000 and 50 000 labeled cells decrease with time. Also the quantitative values obtained from high density seeded cells (HDS) and low density seeded cells (LDS) at 96 h are distinguishable. However, this effect is stronger in the case of  $T_2^*$ .

Summary of kinetic behavior of cells labeled with particle MU119-5zdzN3+N4 is shown in Fig. 4D.1. From the Fig. 4D.1 a clear quantitative difference can be seen between 200 000 cells/ml and 50 000 cells/ml for both  $T_2$  and  $T_2^*$  and a time dependent signal decrease i.e strongest signal or lower  $T_2$  and  $T_2^*$  values at 0 h and weakest signal or higher  $T_2$  and  $T_2^*$  values at 96 h.

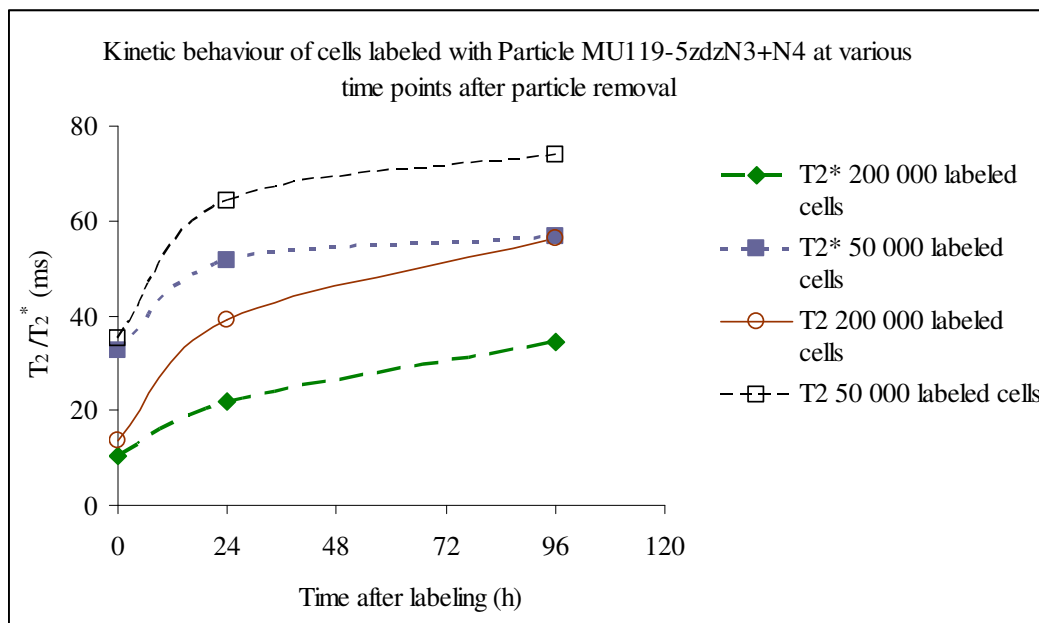


Figure 4D.1: Graph showing summary of  $T_2/T_2^*$  behavior of kinetic study of cells labeled with particle MU119-5zdzN3+N4 at different time interval after particle removal.

$T_2$  and  $T_2^*$  maps of above discussed phantom are shown in Fig. 4D.2. The quantitative trends as discussed before are in agreement with the signal intensities seen on these maps. Signals obtained from 200 000 labeled cells are stronger than those obtained for 50 000 labeled cells (Fig. 4D.2: row 3 sample 1 & 4; row 2 sample 2 & 3; row 1 sample 1 & 2). Further at 96 h high density seeded cells (row 1: sample 1 (200 000 cells) & sample 2 (50 000 cells) shows stronger signal than low density seeded cells (row 1: sample 3 (200 000 cells) & sample 4 (50 000 cells)). Also signals from negative control i.e. unlabeled cells are weak (bright spots on  $T_2$  and  $T_2^*$  map) for both 200 000 and 50 000 cells as compared to their labeled counter part (dark spots on  $T_2$  and  $T_2^*$  map).

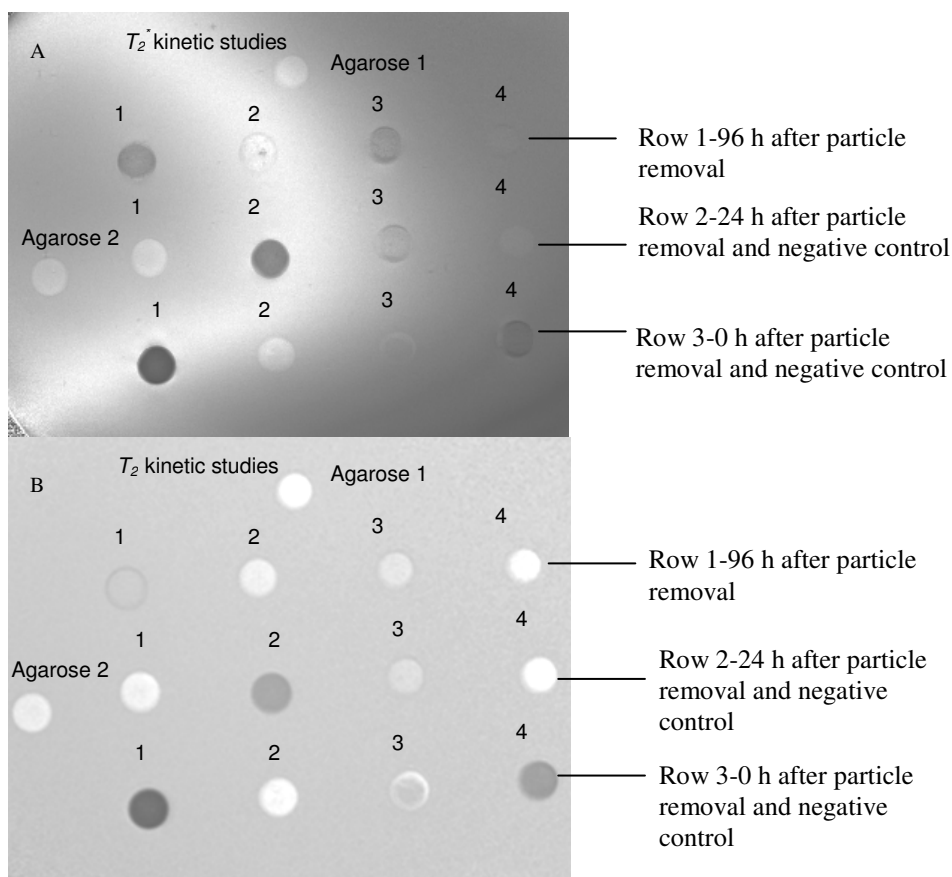


Figure 4D.2:  $T_2^*$  map (A)  $T_2$  map (B) of particle MU 119-5zdz N3+N4 loaded in cells along with negative control at 3T showing kinetic behavior. Row 1 sample 1-4: 200 000 HDS 50 000 cells HDS, 200 000 LDS and 50,000 LDS respectively. Row 2 sample 1-4: 200 000 unlabeled cells, 200 000 labeled cells, 50 000 labeled cells, 50 000 unlabeled cells respectively. Row 3 sample 1-4: 200 000 labeled, 200 000 unlabeled, 50 000 unlabeled, 50 000 labeled cells respectively.

### 4D.3 Conclusion

From the above results it has been observed that cells labeled with MU119-5zdzN3+N4 can be easily detectable even at 96 h after particle removal. Further, difference between signal intensity and quantitative values are significant for 200 000 cells and 50 000 cells in case of both  $T_2$  and  $T_2^*$  and these values were also distinguishable from negative control values. Thus the particle MU119-5zdz N3+N4 having iron content of 2.73 mg Fe/ml with  $r_2^*$  relaxivity of  $294 \text{ mM}^{-1} \cdot \text{s}^{-1}$  and  $r_2$  relaxivity of  $22.4 \text{ mM}^{-1} \cdot \text{s}^{-1}$  shows  $T_2$  as well as  $T_2^*$  effect. However  $T_2^*$



effect is more pronounced at 96 h after particle removal. Thus this particle can be used for further in vivo studies.

### 4.3 Model for correcting $T_2^*$

Problem associated with  $T_2^*$  quantification is that it is suffering from superimposed magnetic field distortions  $\Delta B_0$ , causing a more rapid decay of the MRI signal  $S(t)$ , which results in an underestimation of the resulting  $T_2^*$  value (signal modulation can be clearly seen in Fig. 4D.1A). To overcome this issue a correction model was developed by Prof. Dr. rer. nat. Volker Rasche, details of which are attached in chapter 2 (section I). All the  $T_2^*$  values in the above work were corrected according to that model and were then analyzed accordingly. Fig. 4.2: is one example to show how the  $T_2^*$  data changes after correction.

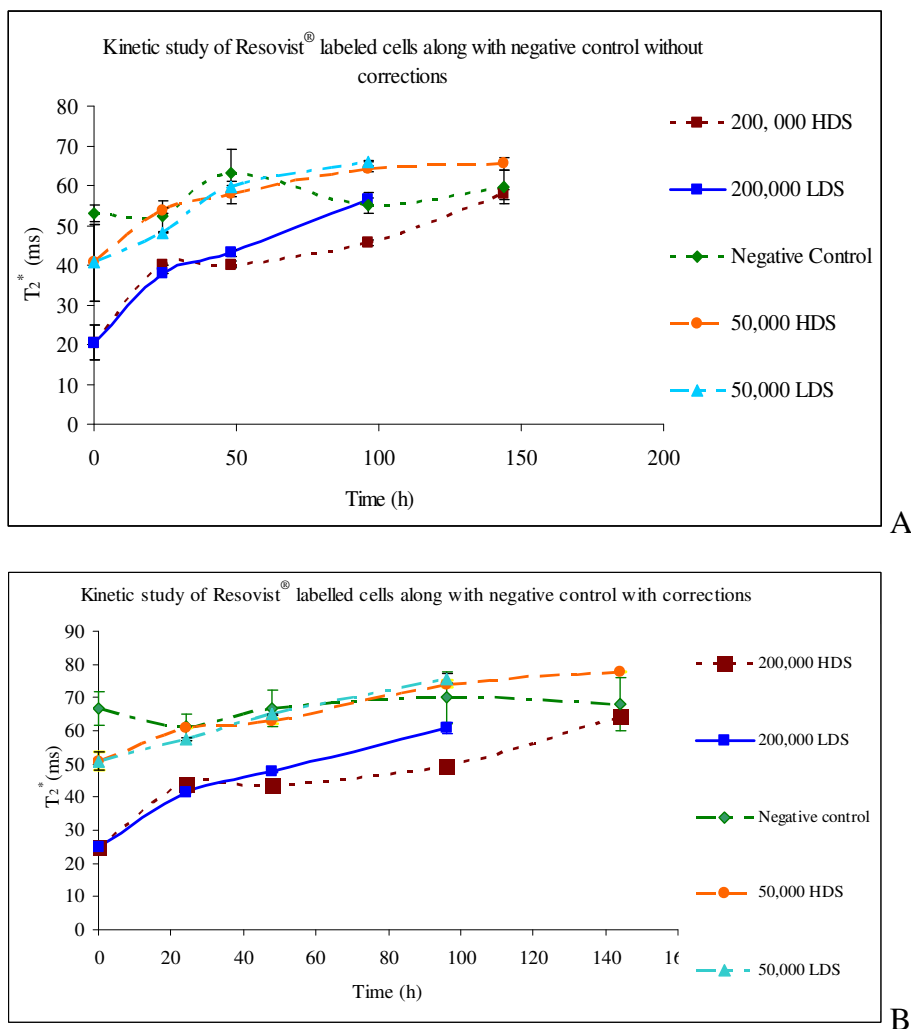


Figure 4.2: Comparison of  $T_2^*$  data for kinetic study of Resovist® labeled cells after particle removal (A) before and (B) after implementation of correction factor

#### 4.4 Overall summary

MR properties of iron-PLLA nanoparticles in agarose were studied.  $T_2$  and  $T_2^*$  values were obtained by using spin echo and gradient echo sequences.  $r_2$  and  $r_2^*$  relaxivity values of these particles were obtained by plotting  $T_2$  and  $T_2^*$  values vs. iron concentration. Particle MU128-1zd showed  $r_2$  ( $243.6 \text{ mM}^{-1} \cdot \text{s}^{-1}$ ) and  $r_2^*$  ( $226.2 \text{ mM}^{-1} \cdot \text{s}^{-1}$ ) relaxivity comparable to Resovist®. However highest  $r_2^*$  relaxivity was shown by particle MU 130-5dz ( $607.4 \text{ mM}^{-1} \cdot \text{s}^{-1}$ ). Iron

content along with iron compositions seems to effective parameter to influence these relaxivity values. MR studies of Resovist<sup>®</sup>/PLL labeled cells suggested that as down to 15 600 cells/ml can be detected by MRI. These cell exhibited strong  $T_2^*$  effect as compared to  $T_2^*$  effect of unlabeled cells.  $T_2$  effect was also distinguishable from the  $T_2$  effect of unlabeled cells. Kinetic studies of Resovist<sup>®</sup>/PLL labeled cells showed distinguishable MR effect at 144 h after particle removal. Also cells labeled with particle MU 119 5zdz N3+N4 showed strong  $T_2^*$  effect at 96 h after particle removal. Thus this particle with  $r_2^*$  relaxivity of  $294 \text{ mM}^{-1} \cdot \text{s}^{-1}$  can be used for further in vivo studies.  $T_2^*$  correction was implemented on all the measured values to overcome the problem of superimposed magnetic field distortion.

## Chapter 5

### **Quantification of Calcifications in Endarterectomy Samples by means of High – Resolution Ultra-short echo time (UTE) Imaging.**

Calcification is an active, regulated process and is probably involved in the very early development of atherosclerotic lesions [101, 102]. Potential links between calcification and atherosclerosis have been proposed [200] and the presence and density of calcium in the plaques are known to impact the plaque vulnerability.

Quantification of vascular calcifications has been shown by Computed tomography (CT) [144, 159] and the resulting calcium score has been proven as an independent risk factor [1]. The current gold standard for the assessment of calcifications by means of imaging is high resolution volume CT, which has proven reliable quantification of the size of calcium lesions with less than 1% error in phantom studies [17].

However, for enabling assessment of the vulnerability of a certain lesion, further data on its morphology, composition, local molecular processes and likely local stress factors are required [194]. A variety of different imaging modalities including invasive techniques such as Intravascular ultrasound (IVUS) and Optical coherence tomography (OCT) as well as non-invasive techniques such as CT angiography (CTA), MRI, and Ultrasound imaging has been applied for the assessment of the different relevant parameters [40, 197, 31, 44].

Its versatile image contrast, possible high spatial resolution, potential for assessing local functional parameter [60], and the ongoing developments of sophisticated contrast agents [178] offers tremendous promise for MRI to contribute for the non-invasive assessment of

plaque vulnerability. However, a major obstacle in MRI imaging of atherosclerotic lesions may arise from calcified segments. The very short  $T_2$  relaxation times of solid calcifications in the order of few  $\mu\text{s}$  [77] causes almost complete signal cancellation and the local change in susceptibility and the rapid signal decay may cause significant overestimation of the calcified region. In conventional gradient echo based MRI with TEs in the 1-2 ms range, calcified tissues cannot be detected [77] and the different densities of the calcium in a certain lesion can not be assessed. Spin echo based techniques may be applied for reduction of the susceptibility induced blur, but due to excessive acquisition times its application is limited in case of high-resolution volumetric imaging.

Ultra-short echo time (UTE) sequences [77, 145, 154] have been recently reported as promising tool for imaging of short  $T_2$  tissues by MRI [64, 148, 149, 153, 190, 196]. The main advantage of UTE rises from its FID approach, in which the center of k-space is measured directly after the excitation. Using a non-selective excitation pulse in combination with a low flip angle excitation, the possible minimal echo time TE is only limited by the switch time of the RF frontend from transmit to receive mode. It has been shown that switch times down to few  $\mu\text{s}$  can be achieved even on clinical MRI systems [26]. Initial application of UTE imaging to the assessment of calcified lesions indicated its potential in the visualization of calcified lesion as well as the reduction of the related image blur [171 and references therein].

The objective of this work is to investigate the feasibility of the UTE technique for the assessment of calcification in atherosclerotic lesions. The UTE technique was applied to the imaging of thirty five carotid endarterectomy samples and the respective areas of the calcifications and the resulting normalized image intensities were quantified. Results were compared with high-resolution volume CT (VCT) and histology to validate the area and density of the calcium.

## 5.1 Materials and Methods

### 5.1.1 Sample Preparation

Thirty five endarterectomy samples were preserved in 10% formalin directly after resection. In order to decrease the susceptibility artifacts and to mimic the biological conditions the samples were embedded in agarose gel. 0.10 g of agarose (Serva, Heidelberg, Germany) was added to 83 ml of distilled water. The sample was then stirred for 2 minutes on a magnetic stirrer and then heated in a microwave oven till the agarose got completely dissolved. These samples were then poured into a petri dish (size 50 mm, Becton Dickson Heidelberg) and the endarterectomy samples were embedded.

### 5.1.2 MRI imaging sequence and protocol

For the presented work 3D UTE sequence was used to for the assessment of calcium in endarterectomy samples. UTE sequence is based on 3D technique and uses a non selective RF excitation pulse with 3D radial FID sampling, yielding image data with isotropic resolution. The basic pulse diagram for UTE sequence is shown in Fig. 5.1.

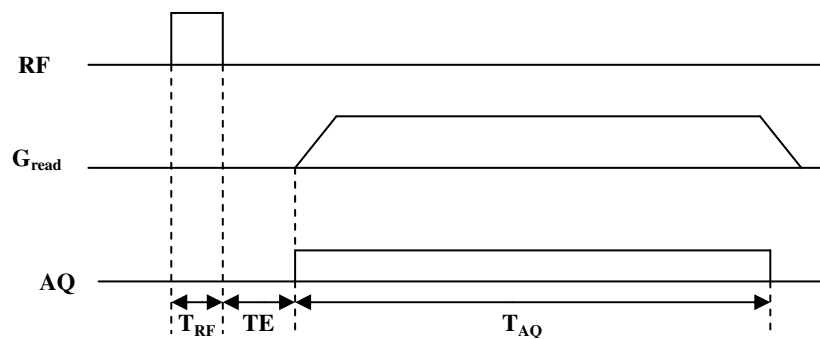


Figure 5.1: 3D UTE sampling scheme. A hard block pulse RF excitation of duration  $T_{RF}$  is followed by 3D radial FID sampling during  $T_{AQ}$  using the read out gradient  $G_{read}$ . The echo time  $TE$  is defined as the interval between the end of excitation pulse (RF) and the beginning of the acquisition window [145].

A hard radiofrequency (RF) pulse is used for excitation and ramp sampling is used in acquisition. Radial profiles are arranged with isotropic angular spacing to cover a sphere in k-space. The echo time (TE) is defined as the interval between the end of the RF pulse and the beginning of the sampling window, although alternative, but less practical definitions of TE exist [145]. To minimize  $T_2$  induced signal loss, the duration of the RF excitation pulse and the echo time must be minimized. Using low tip angle excitations, the RF pulse can be kept much shorter than 100  $\mu$ s. After the pulse, the energy stored in the transmit coil must ring down to allow safe tuning of the receive coils. While ring down typically takes only a few  $\mu$ s, tuning of the coil can be more time consuming. Fast switching coils ensure minimal TE below 100  $\mu$ s and minimize signal decay prior to acquisition. Sampling is started simultaneously with the rising slope of the readout gradient, i.e., k-space is traversed radially from  $k = 0$  outward. Due to limitations in the strength and slew rate of the read out gradient, the sampling window duration ( $T_{AQ}$ ) will usually be on the order of several hundred  $\mu$ s and therefore much longer than the RF pulse and TE. Consequently, the minimal resolvable  $T_2$  will be mainly determined by the duration of the acquisition window  $T_{AQ}$ . Although the sampled FID signal underlies  $T_2^*$  decay but for fast relaxing components,  $T_2^*$  decay often is mainly determined by homogeneous  $T_2$  relaxation, and  $T_2^* \approx T_2$  holds [145].

For experimental purpose all the measurements were done on a 3T whole-body system (Achieva, Philips Medical Systems, Best, The Netherlands) with gradient hardware capable of max gradient amplitude of (40 mT / m) using a maximum slew rate of 200 mT / ms. Data was received by a single 65 · 50 mm element of a dedicated two times two-element carotid artery coil sized 120 · 50 mm (Philips, Research Europe, Hamburg, Germany). All samples underwent the following MR protocol:

- Gradient echo acquisition (FFE)

TE/TR = 5.7/15 ms,  $\alpha = 10^\circ$ , 0.25 mm<sup>3</sup> spatial resolution, FOV = 80 mm<sup>3</sup>, NSA = 6, scan duration 2 h 43 min.

- UTE acquisition

TE/TR = 0.05 / 15 ms,  $\alpha = 10^\circ$ , 0.25 mm<sup>3</sup> spatial resolution, FOV = 80 mm<sup>3</sup>, NSA = 8, scan duration 6 h 33 min.

### 5.1.3 Volume CT

After MRI data acquisition, the samples underwent high-resolution three-dimensional rotational X-ray data acquisition (VCT) on an interventional flat panel X-ray system (Allura FD, Philips Medical Systems, Best, The Netherlands). Since calcium is a high-density object, a conventional three-dimensional high-resolution protocol was used. Data was acquired over an angular range of 220° at approximately 1° angular spacing. Detector pixel size was 180<sup>2</sup>  $\mu\text{m}^2$  and the tube current was chosen as 70 kV. Prior to the acquisition, the complete system calibration has been performed to ensure optimal reconstruction accuracy. The data was reconstructed applying a modified Feldkamp algorithm making full use of the priory acquired calibration parameter. The applied technique has proven high geometrical accuracy [146].

### 5.1.4 Histology

In order to avoid loss of calcification during section cutting (which is common for paraffin embedded and frozen sections) after MRI and X-Ray analysis the samples were embedded in plastic. For plastic embedding, the samples were first removed from the agarose gel and then fixed in 4% formalin. After fixation, the carotids samples were dehydrated in a graded series of ethanol washes and then embedded in methyl methacrylate. After polymerization, thin sections (60  $\mu\text{m}$ ) were prepared and stained with Kossa and Kernechtrot for calcium and nucleus staining respectively. The stained samples were then viewed under light microscope. Embedding of the tissue in plastic helps to prevent loss of calcification during sectioning while retaining stain and antibody reactivity.



### 5.1.5 Data Analysis

Registration of the MRI and VCT data was achieved by careful positioning of the sample in the iso-center of either system. The orientation of the sample was well aligned with the patient support so that variation of the subject orientation could be limited to a rotation around the anterior-posterior axis, which was addressed manually during data analysis. Since the orientation and shape of the samples changed during the histology process, the alignment of the histological cuts with the imaging data was obtained manually by rotation of the isotropic imaging volumes.

All statistical analysis was performed by a two-tailed paired students' T-test. Values below 0.05 were assumed statistically significant.

#### 5.1.5.1 Area measurements

For the area measurement, contours of major calcified regions were drawn manually in the different imaging data sets in a blinded fashion. The appearing size of the calcified sections was compared amongst the different imaging approaches. Bland-Altman analyses were performed for comparing the area obtained by UTE, conventional FFE, and the VCT approach.

#### 5.1.5.2 Measurement of signal intensity

For direct comparison of the UTE and conventional FFE technique for calcium classification, regions showing different levels of calcification were selected qualitatively by visual inspection of the histology cuts. The mean intensity value of an ellipsoid ROI located in the identified region was obtained in either MRI image. To avoid influence of different amplifier settings, the intensities were normalized with the signal intensity value obtained in the agarose gel. The normalized signal intensity  $I_{UTE}$  from the UTE technique was used for forming four classes:  $I_{UTE} < 0.2$ ,  $0.2 \leq I_{UTE} < 0.4$ ,  $0.4 \leq I_{UTE} < 1$  and  $I_{UTE} > 1$ . The mean signal intensity

value of each class was compared for the two MRI techniques and compared with the visual appearance in the histological cuts.

## **5.2 Results**

A summary of the resulting image quality for the different imaging techniques and the respective histological cuts is presented in Fig. 5.2 and Fig. 5.3 respectively. For a better appreciation of the appearance of the calcifications, the MRI images are additionally displayed with inverted contrast. From the images, in comparison to the UTE and VCT images, a substantial enlargement of the calcified lesions becomes apparent in the FFE images. The shape of the calcification in the UTE images correlates well with histology and the VCT images. Furthermore, different densities of calcium (gray shades) can be appreciated in the UTE images, which correlate well with non-solid calcifications visible in histology.

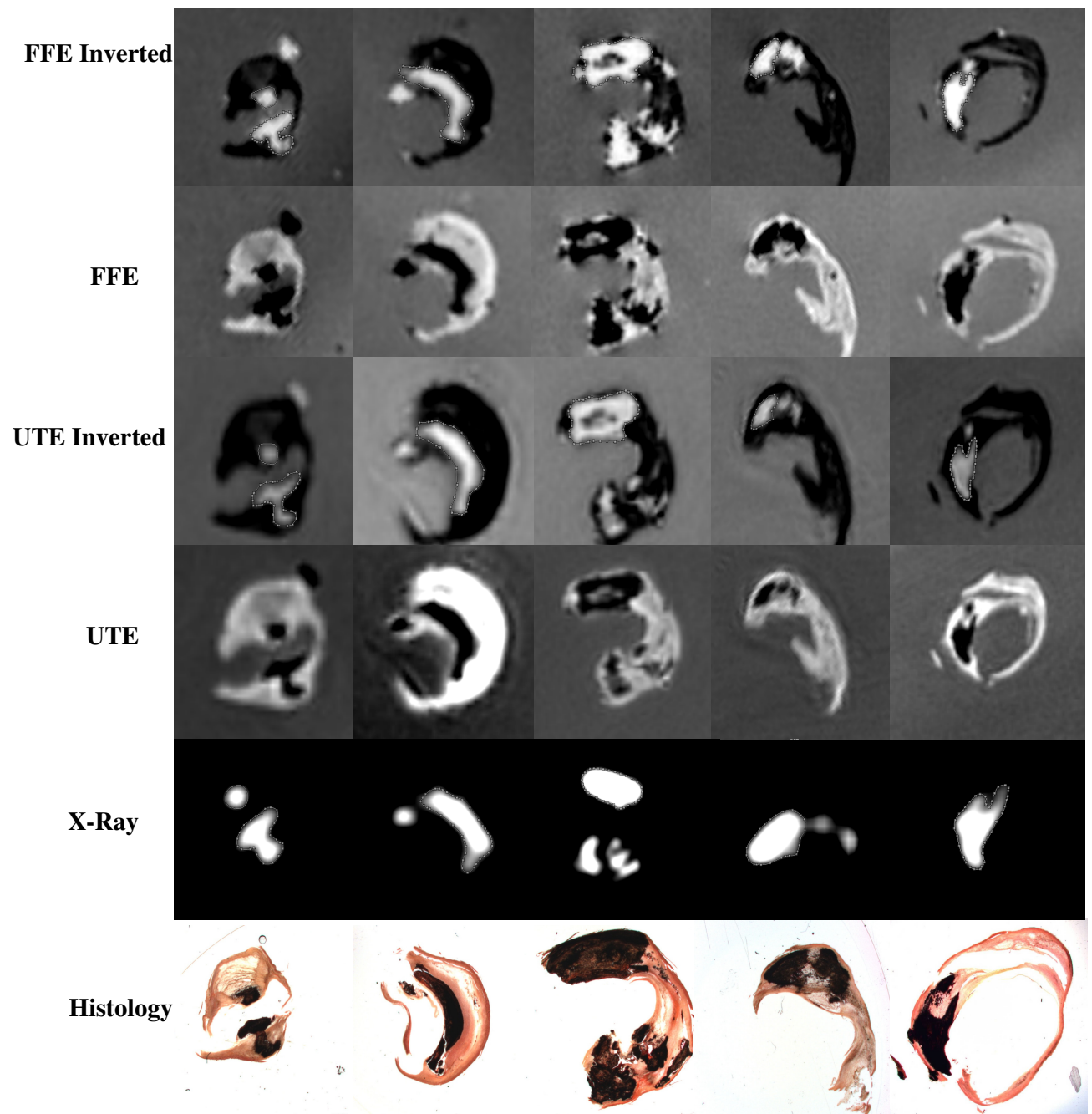


Figure 5.2: Appearance of a major calcification in FFE, UTE, Histology and X-Ray.

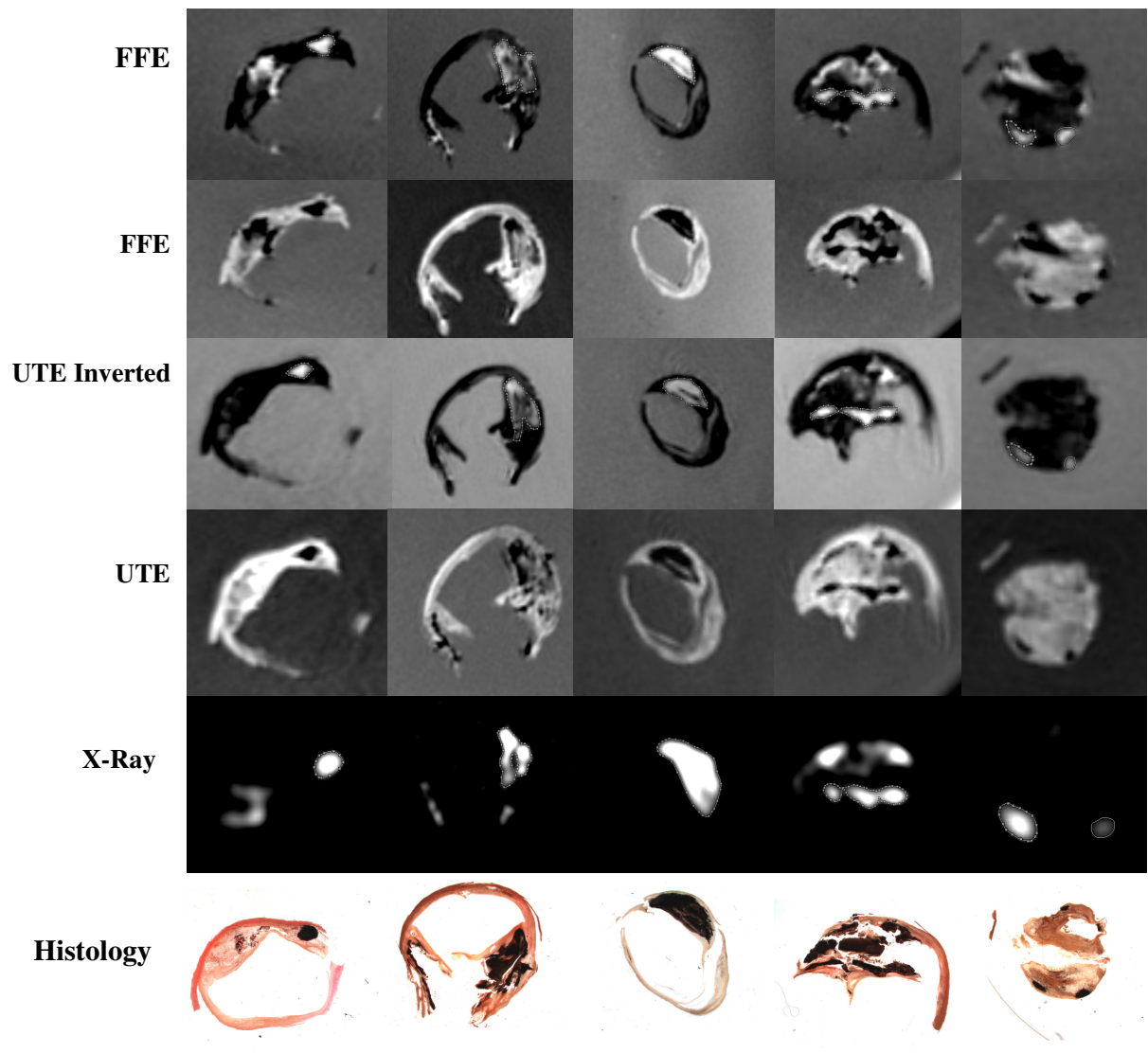


Figure 5.3: Appearance of a major calcification in FFE, UTE, Histology and X-Ray.

Bland-Altman plots comparing the areas of the calcifications derived by the FFE and UTE technique with the VCT results are shown in Fig. 5.4.

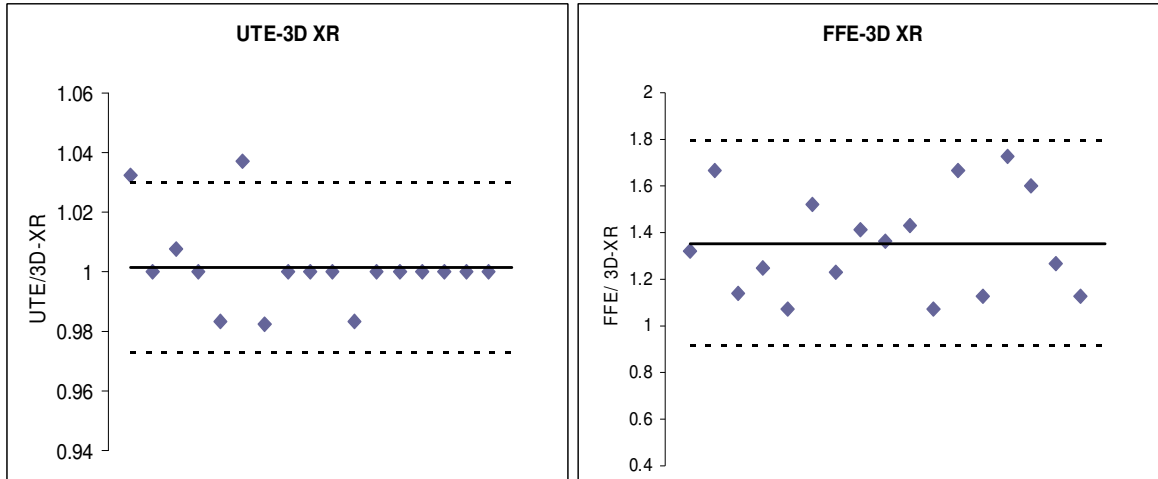


Figure 5.4: Bland-Altman plots comparing the calcified areas in UTE and FFE with 3D XR.

The Bland-Altman plots reveal an excellent agreement between the UTE and the VCT technique with no significant difference. For the FFE technique, a highly statistical difference ( $p < 0.001$ ) overestimation of the calcifications in the order of 35% was observed (Table 5.1).

Table 5.1: The table shows the respective bias (dA) and standard deviation ( $\sigma$ ) for calcified areas in FFE and UTE as compared with 3D XR.

	UTE	FFE
dA [ %]	+ 1	+ 35
$\sigma$ [%]	1.4	21

14 samples showed lesions with substantial differences in the calcium density and were selected for further quantitative analysis of the resulting signal intensities in the UTE and FFE technique. Among these samples 11 regions were classified as highly calcified (signal intensity value  $< 0.2$ ), 11 regions were moderately calcified (value  $\geq 0.2 < 0.4$ ), 7 regions

were less calcified (value  $\geq 0.4 < 1$ ) and 10 regions were very less calcified (value  $> 1$ ). Fig. 5.5 show three representative images to show this classification and their normalised intensity values are shown in Table 5.2.

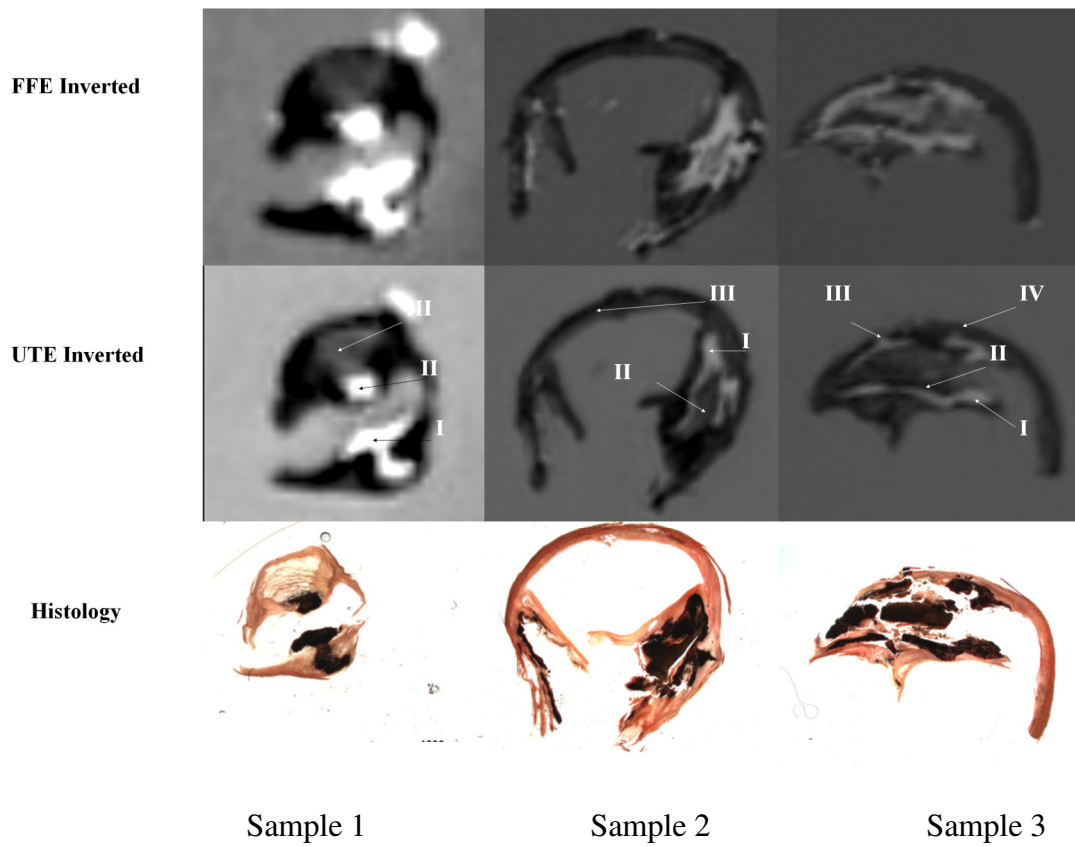


Figure 5.5: Three representative images to show different calcified regions in FFE and UTE images. Their respective histology images are shown below for comparison.

Table 5.2: Normalised intensity values for different calcified regions for three representative samples shown in Fig. 5.5

		I	II	III	IV
Sample 1	UTE	0.397	0.464	1.80	
	FFE	0.167	0.166	1.477	
Sample 2	UTE	0.76	1.39	1.908	
	FFE	0.49	0.55	1.616	
Sample 3	UTE	0.536	0.632	1.137	1.936
	FFE	0.339	0.238	0.380	1.57

Fig. 5.6 show the mean value of the signal intensity obtained in the different classes for the UTE and the FFE technique. As expected from the very short TE, the UTE technique yields significantly ( $p < 0.01$ ) higher signal intensities for classes I-III and a trend for higher signal intensities ( $p < 0.1$ ) for class IV.

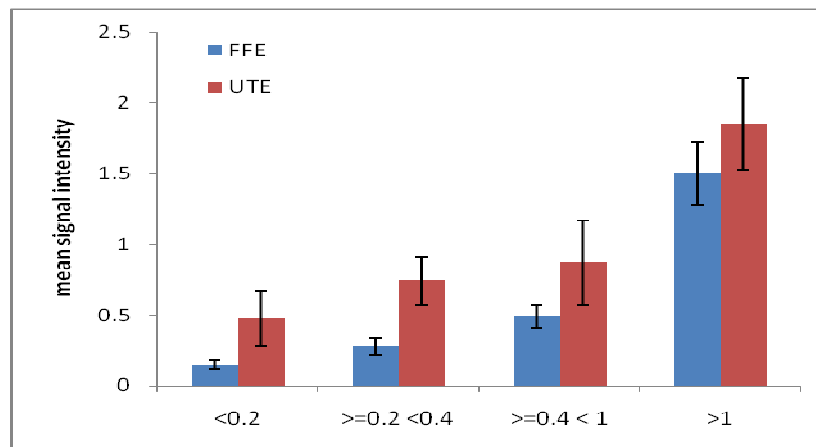


Figure 5.6: Plot of mean signal intensities obtained from UTE and FFE sequence against different level of calcification.

The ratio of normalised intensities  $I_{UTE}$  and  $I_{FFE}$  and hence the possible gain in signal intensity is shown in Fig. 5.7. It clearly shows the increasing gain in relative signal intensity with increasing amount of calcium in the lesion.

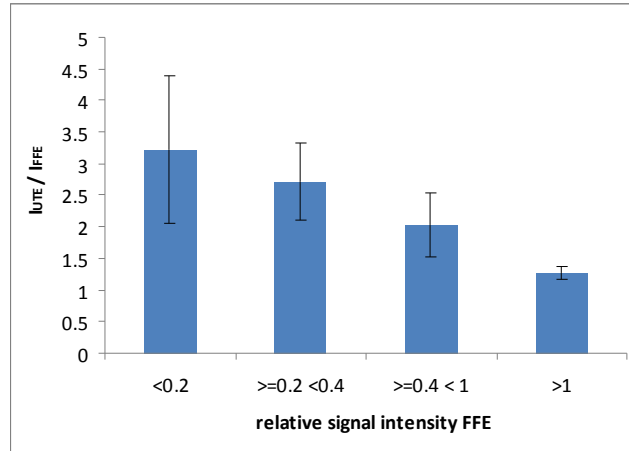


Figure 5.7: Plot of ratio of normalised intensity  $I_{UTE}$  vs.  $I_{FFE}$  against level of calcification.

### 5.3 Discussion

This work demonstrates the applicability of high-resolution ultra-short TE (UTE) MRI for accurate quantification of the volume of atherosclerotic calcifications. The direct comparison of UTE to conventional gradient echo techniques (FFE) reveals a significant overestimation of the calcium volume by the conventional techniques. The good agreement of the UTE images with the gold-standard VCT and histology implies a similar performance of this technique for plaque volume quantification.

Furthermore, it could be shown that by application of the UTE technique, the signal from calcified sections of the plaque can be significantly enhanced. This may in future applications facilitate delineation of different degrees of calcifications, which can not be clearly delineated in FFE due to its poor signal intensity levels.



Extension of the current MRI protocols for plaque quantification by the UTE technique may provide additional insights into the local calcium distribution and density, which have up to now only been assessable by CT. Whether the precise knowledge of the volume of the calcified area and the qualitative assessment of the calcium density will add significant new information for the classification of atherosclerotic lesions and especially the respective vulnerability, however, remains to be proven.

A limitation of the study rises from the transferability of the results into clinical routine. All data were acquired at very high isotropic resolution, which causes unacceptable long scan times for in-vivo application. For the reduction of the scan time, however, compromises in the spatial resolution will have to be made, which are supposed to cause less accurate quantification of the calcium volume. Furthermore, in its current implementation, the UTE technique comprises a non-selective excitation for minimizing echo-times down to some  $\mu\text{s}$ . Non-selective excitation will cause limitations in clinical routine, since the investigated ROI can only be controlled by adequate selection of the receive coil, the sensitivity pattern of which will finally define the ROI to be covered by the actual acquisition. This may limit the application of UTE to the assessment of lesions of superficial arteries such as the carotids. For wider application of the UTE technique, more sophisticated excitation techniques such as suggested by Josan et al [89] might be required to enable additional slice selection.

## **5.4 Conclusion**

This work demonstrates the potential of ultra short echo time imaging (UTE) with isotropic 3D spatial resolution for imaging of calcified atherosclerotic lesions. The UTE technique enables accurate quantification of plaque volumes as well as a qualitative assessment of the local calcium density. Incorporation of the UTE technique in today MRI protocols for plaque classification holds the potential to add the missing important information on plaque volume and density solely based on MRI data.

## Summary

The objective of the study done in this thesis was to facilitate targeted plaque imaging in future. For targeted MR imaging, contrast agents (CA), which can carry high payload and specifically bind to a certain target molecules are required. Thus in the first part of this work the principle of inverse miniemulsion applied to encapsulate different gadolinium based commercially available contrast agents like Magnevist<sup>®</sup>, Gadovist<sup>®</sup> and Multihance<sup>®</sup> resulted into high payload of about  $2.5 \cdot 10^6 \text{ Gd}^{3+}$  complexes per nanocapsule resulting in relaxivity of  $10.75 \cdot 10^6 \text{ mM}^{-1} \cdot \text{s}^{-1}$  per nanocapsule. Maintained or even slightly increased relaxivity values of different contrast agents after encapsulation in combination with high payloads and the possibility of functionalization of the capsules facilitate the application of the nanocapsules as promising targeted contrast agents for MRI. A slightly modified strategy of using gels in the synthesis of polymeric nanocapsules for encapsulating the commercial contrast agents like Magnevist<sup>®</sup> was found to be very effective but further study is needed to understand this system.

In the second part of the work, MR properties of biodegradable iron-poly-L-lactic (PLLA) nanoparticles synthesized via the miniemulsion process were tested in both chemical and biological environment using 3T MRI system. Relaxivity values of different particles were compared with the relaxivity values of the commercially available contrast agent, Resovist<sup>®</sup>. Among several particles tested, particle MU128-1zd showed relaxivity comparable to Resovist<sup>®</sup>. Further, MR studies done on the MSCs cells labeled with MU 119 5zdz N3+N4 show a intracellular persistence of particle in MSCs cell up to 144 h after particle removal (i.e. iron source was removed from the medium after incubating the cells). Thus, strong  $T_2^*$  effect, even at 144 h after particle removal, and having high  $T_2^*$  relaxivity made this innovative iron-PLLA particle a suitable candidate for further in vivo studies. Model used for correcting the measured  $T_2^*$  correction gave better results to overcome the problem of superimposed magnetic field distortion.

So far studies done in this thesis have resulted in suitable carriers for gadolinium and iron based contrast agents for site specific delivery. Another major problem in MR imaging is that the negative contrast obtained using conventional  $T_2/T_2^*$  weighted sequences can be mixed up with the signal loss caused by other sources like presence of calcium in plaque. Thus in the last part of this work UTE sequence was used to visualize and quantify calcification in carotid endarterectomy (CEA). Images were acquired using UTE sequence ( $TE = 50 \mu s$ ) and comparison was made between those obtained from  $T_1W$  gradient echo sequence ( $TE = 5.7 ms$ ), high-resolution volume CT (VCT) and histology. The UTE technique yielded accurate quantification of the volume of the calcification as well as enabled qualitative assessment of the calcium density according to the resulting relative signal intensity. In comparison, the FFE technique yielded an average overestimation of the lesion size by about 35% and the low signal intensity did not allow a clear delineation of the different calcium densities. In conclusion, incorporation of the UTE technique in today MRI protocols for plaque classification holds the potential to add the missing important information on calcium volume and density solely based on MRI data.

## References

- 1 Achenbach S, Daniel WG: Current role of cardiac computed tomography. *Herz* 32: 97-107 (2007).
- 2 Ahern AM, Garrell RL: Characterization of polyacrylamide gel formation and structure by surface-enhanced Raman spectroscopy. *Langmuir* 4: 1162-1168 (1988).
- 3 Aime S, Castelli DD, Crichton SG, Gianolio E, Terreno E. Pushing the sensitivity envelope of lanthanide based magnetic resonance imaging (MRI) contrast agents for molecular imaging applications. *Accounts of Chemical Research*. (Article in press) (2009).
- 4 Aime S, Crichton SG, Gianolio E, Giovenzana GB, Tei L, Terreno E: High sensitivity lanthanide (III) based probes for MR-medical imaging. *Coordination Chemistry Reviews* 250: 1562-1579 (2006).
- 5 Aime S, Frullano L, Crichton SG: Compartmentalization of a gadolinium complex in the apoferritin cavity: A route to obtain high relaxivity contrast agents for magnetic resonance imaging. *Angewandte Chemie-International Edition* 114: 1059-1061 (2002).
- 6 Alain R, Muller RN, Gillis P: Theory of proton relaxation induced by superparamagnetic particles. *Journal of Chemical Physics* 110: 5403-5411 (1999).
- 7 Alviano F, Fossati V, Marchionni C, Arpinati M, Bonsi L, Franchina M, Lanzoni G, Cantoni S, Cavallini C, Bianchi F, Tazzari PL, Pasquinelli G, Foroni L, Ventura C, Grossi A, Bagnara GP: Term amniotic membrane is a high throughput source for multipotent mesenchymal stem cells with the ability to differentiate into

- endothelial cells in vitro. *BMC Development Biology* 7: 15-21 (2007).
- 8 Amsalem Y, Mardor Y, Feinberg MS, Landa N, Miller L, Daniels D, Ocherashvilli A, Holbova R, Yosef O, Barbash IM, Leor J: Iron-oxide labeling and outcome of transplanted mesenchymal stem cells in the infarcted myocardium. *Circulation* 116: I-38-I-45 (2007).
  - 9 Anderson SA, Glod J, Arbab AS, Noel M, Ashari P, Fine HA, Frank JA: Noninvasive MR imaging of magnetically labeled stem cells to directly identify neovasculature in a glioma model. *Blood* 105: 420-425 (2005).
  - 10 Arbab AS, Bashaw LA, Miller BR, Jordan EK, Lewis BK, Kalish H, Frank JA: Characterization of biophysical and metabolic properties of cells labeled with superparamagnetic iron oxide nanoparticles and transfection agent for cellular MR imaging. *Radiology* 229: 838-846 (2003).
  - 11 Arbab AS, Jordan EK, Wilson LB, Yocum GT, Lewis BK, Frank JA: In vivo trafficking and targeted delivery of magnetically labeled stem cells. *Human Gene Therapy* 15: 351–360 (2004).
  - 12 Arbab AS, Pandit SD, Anderson SA, Yocum GT, Bur M, Frenkel V, Khuu HM, Read EJ, Frank JA: Magnetic resonance imaging and confocal microscopy studies of magnetically labeled endothelial progenitor cells trafficking to sites of tumour angiogenesis. *Stem Cells* 24: 671–678 (2006).
  - 13 Arbab AS, Yocum GT, Kalish H, Jordan EK, Anderson SA, Khakoo AY, Read EJ, Frank JA: Efficient magnetic cell labeling with protamine sulfate complexed to ferumoxides for cellular MRI. *Blood* 104: 1217-1223 (2004).
  - 14 Arbab AS, Yocum GT, Rad AM, Khakoo AY, Fellowes V, Read EJ, Frank JA: Labeling of cells with ferumoxides–protamine sulfate complexes does not inhibit

- function or differentiation capacity of hematopoietic or mesenchymal stem cell. *NMR in Biomedicine* 18: 553–559 (2005).
- 15 Bach-Gansmo T: Ferrimagnetic susceptibility contrast agents. *Acta Radiologica Supplement* 387: 5-30 (1993).
  - 16 Baksh D, Yao R, Tuan RS: Comparison of proliferative and multilineage differentiation potential of human mesenchymal stem cells derived from umbilical cord and bone marrow. *Stem Cells* 25: 1384-1392 (2007).
  - 17 Begemann PG, van Stevendaal U, Koester R, Mahnken AH, Koops A, Adam G, Grass M, Nolte-Ernsting C. Evaluation of the influence of acquisition and reconstruction parameters for 16-row multidetector CT on coronary calcium scoring using a stationary and dynamic cardiac phantom. *European Radiology* 17: 1985-1994 (2007).
  - 18 Benderbous S, Bonnemain B: Superparamagnetic nanoparticles as blood-pool contrast agents. Contribution to MRI preclinical investigations. *Radiology* 35: S248–S252 (1995).
  - 19 Bennett HF, Brown DR, Koenig HS, Swartz MH: Effects of nitroxides on the magnetic field and temperature dependence of  $1/T_1$  of solvent water protons. *Magnetic Resonance in Medicine* 4: 93-111 (1987).
  - 20 Berne BJ and Pecora R: *Dynamic light scattering: with applications to chemistry, biology and physics*. Dover Publications, Mineola, New York (2000).
  - 21 Bernstein MA, King KF, Zhou XJ: *Handbook of MRI Pulse Sequences*. Academic Press (2004).
  - 22 Bianchi A, Calabi L, Corana F, Fontana S, Losi P, Maiocchi A, Paleari L, Valtancoli B: Thermodynamic and structural properties of Gd (III) complexes with

- polyamino polycarboxylic ligands: basic compounds for the development of MRI contrast agents. *Coordination Chemistry Reviews* 204: 309-393 (2000).
- 23 Bloembergen N: Proton relaxation times in paramagnetic solutions. *Journal of Chemical Physics* 27: 572-573 (1957).
- 24 Bomati-Miguel O, Morales MP, Tartaj P, Ruiz-Cabello J, Bonville P, Santos M, Zhao X, Veintemillas-Verdaguer S: Fe-based nanoparticulate metallic alloys as contrast agents for magnetic resonance imaging. *Biomaterials* 26: 5695–5703 (2005).
- 25 Bottrill M, Nicholas LK, Long NJ: Lanthanides in magnetic resonance imaging. *Chemical Society Reviews* 35: 557-571 (2006).
- 26 Brittain JH, Shankaranarayanan A, Ramanan V, Shimakawa A, Cunningham CH, Hinks S, Francis R, Turner R, Johnson JW, Nayak KS, Tan S, Pauly JM, Bydder GM: Ultrashort TE imaging with single-digit (8  $\mu$ s) TE. In *Proceedings of the 12th Annual Meeting of ISMRM, Kyoto, Japan*, 629 (2004).
- 27 Brix G, Schad RL, Deimling M, Lorenz JW: Fast and precise  $T_1$  imaging using a TOMROP sequence. *Magnetic Resonance Imaging* 8: 351-356 (1990).
- 28 Brown MA, Semelka RC: MR imaging abbreviations, definitions and descriptions a review. *Radiology* 213: 647-662 (1999).
- 29 Bryant LH, Brechbiel MW, Wu C, Bulte JWM, Herynek V, Frank JA: Synthesis and relaxometry of high-generation (G = 5, 7, 9, and 10) PAMAM dendrimer-DOTA- gadolinium chelates. *Journal of Magnetic Resonance Imaging* 9: 348-352 (1999).
- 30 Bulte JWM, Kraitchman DL: Iron oxide MR contrast agents for molecular and cellular imaging. *NMR in Biomedicine* 17: 484–499 (2004).

- 31 Cademartiri F, La Grutta L, Palumbo A, Malagutti P, Pugliese F, Meijboom WB, Baks T, Mollet NR, Bruining N, Hamers R, de Feyter PJ. Non-invasive visualization of coronary atherosclerosis: state-of-art. *Journal of Cardiovascular Medicine (Hagerstown)* 8: 129-37 (2007).
- 32 Can A, Karahuseyinoglu S: Concise review: human umbilical cord stroma with regard to the source of fetus-derived stem cells. *Stem Cells* 25: 2886- 2895 (2007).
- 33 Caravan P: Strategies for increasing the sensitivity of gadolinium based MRI contrast agents. *Chemical Society Reviews* 35: 512-523 (2006).
- 34 Chen HH, Visage CL, Qiu B, Du X, Ouwerkerk R, Leong KM, Yang X: MR imaging of biodegradable polymeric microparticles: A potential method of monitoring local drug delivery. *Magnetic Resonance in Medicine* 53: 614-620 (2005).
- 35 Cheng Z, Tsourkas A: Paramagnetic porous polymersomes. *Langmuir* 24: 8169-8173 (2008).
- 36 Chrysikopoulos HS: *Clinical MR Imaging and Physics: A tutorial*. Springer Verlag Berlin, Germany (2009).
- 37 Clement O, Luciani A: Imaging the lymphatic system, possibilities and clinical applications. *European Radiology* 8: 1198-1507 (2004).
- 38 Crawle AP, Henkelman RM: A comparison of one-shot and recovery methods in  $T_1$  imaging. *Magnetic Resonance in Medicine* 7: 23-34 (1988).
- 39 Crespy D, Stark M, Richter CH, Ziener U, Landfester K: Polymeric nanoreactors for hydrophilic reagents synthesized by interfacial polycondensation on



- miniemulsion droplets. *Macromolecules* 40: 3122-3135 (2007).
- 40 Crouse JR: Thematic review series: patient-oriented research. Imaging atherosclerosis: state of the art. *Journal of Lipid Research* 47: 1677-1699 (2006).
  - 41 Daniel MR, Aleksandra R, Sebastian K, David HM, Mohan SU, John RP: Modified Look-Locker Inversion Recovery (MOLLI) for high-resolution  $T_1$  mapping of the heart. *Magnetic Resonance in Medicine* 52: 141-146 (2004).
  - 42 Dausend J, Musyanovych A, Dass M, Walther P, Schrezenmeier H, Landfester K, Mailänder V: Uptake mechanism of oppositely charged fluorescent nanoparticles in Hela cells. *Macromolecular Bioscience* 8: 1135-1143 (2008).
  - 43 Deans RJ, Moseley AB: Mesenchymal stem cells: biology and potential clinical uses. *Experimental Hematology* 28: 875-884 (2000).
  - 44 Desai MY, Lima JA: Imaging of atherosclerosis using magnetic resonance: state of the art and future directions. *Current Atherosclerosis Reports* 8: 131-139 (2006).
  - 45 Doble DMJ, Melchior M, O'Sullivan B, Siering C, Xu J, Pierre VC, Kenneth RN: Toward optimized high-relaxivity MRI agents: The effect of ligand basicity on the thermodynamic stability of hexadentate Hydroxypyridonate/Catecholate Gadolinium (III) complexes. *Inorganic Chemistry* 42: 4930-4937 (2003).
  - 46 Dominici M, Le Blanc K, Mueller I, Slaper-Cortenbach I, Marini F, Krause D, Deans R, Keating A, Prockop DJ, Horwitz E: Minimal criteria for defining multipotent mesenchymal stromal cells. The International Society for Cellular Therapy position statement. *Cytotherapy* 8: 315-317 (2006).
  - 47 Donahue KM, Weisskoff RM, Burstein D: Water diffusion and exchange as they influence contrast enhancement. *Journal of Magnetic Resonance Imaging* 7: 102-

- 110 (1997).
- 48 Elizabeth H, Graeme M, Ting LY, Brian RK: A fast 3D Look-Locker method for volumetric  $T_1$  mapping. *Magnetic Resonance Imaging* 17: 1163–1171 (1999).
- 49 Elster AD, Burdette JH: Questions and answers in magnetic resonance Imaging. Mosby Publication (2001).
- 50 Faraji HA, Wipf P: Nanoparticles in cellular drug delivery. *Bioorganic & Medicinal Chemistry* 17: 2950–2962 (2009).
- 51 Ferrucci JT, Stark DD: Iron oxide-enhanced MR imaging of the liver and spleen: Review of the first 5 years. *American Journal of Roentgenology* 155: 943–950 (1990).
- 52 Fisher M: Stem cell transplantation for stroke: does it work, and if so, how? *Stroke* 34: 2085-2083 (2003).
- 53 Flory PJ: Principles of Polymer Chemistry. Cornell University Press (1953).
- 54 Frank JA, Anderson SA, Kalsih H, Jordan EK, Lewis BK Yocum GT, Arbab AS: Methods for magnetically labeling stem and other cells for detection by in-vivo magnetic resonance imaging. *Contrast Media & Molecular Imaging* 3: 223-232 (2008).
- 55 Frank JA, Miller BR, Arbab AS, Zywicke HA, Jordan EK, Lewis BK, Bryant LH Jr, Bulte JWM: Clinically applicable labelling of mammalian cells and stem cells by combining (FDA)-approved superparamagnetic iron oxides and commonly available transfection agents. *Radiology* 228: 480-487 (2003).
- 56 Frank JA, Zywicke H, Jordan EK, Mitchell J, Lewis BK, Miller B, Bryant LH,

- Bulte JWM: Magnetic intracellular labelling of mammalian cells by combining (FDA-approved) superparamagnetic iron oxide MR contrast agents and commonly used transfection agents. *Academic Radiology* 9: S484-S487 (2002).
- 57 Freed JH: Dynamic effects of pair correlation functions on spin relaxation by translational diffusion in liquids. II. Finite jumps and independent  $T_1$  processes. *Journal of Chemical Physics* 68: 4034- 4037 (1978).
- 58 Fried JR: *Polymer Science and Technology*. Prentice Hall PTR (1995).
- 59 Friedenstein AJ, Chailakhjan RK, Lalykina KS: The development of fibroblast colonies in monolayer cultures of guinea-pig bone marrow and spleen cells. *Cell & Tissue Kinetics* 3: 393-403 (1970).
- 60 Frydrychowicz A, Stalder AF, Russe MF, Bock J, Bauer S, Harloff A, Berger A, Langer M, Hennig J, Mark M: Three-dimensional analysis of segmental wall shear stress in the aorta by flow-sensitive four-dimensional-MRI. *Journal of Magnetic Resonance Imaging* 30: 77-84 (2009).
- 61 Fukuchi Y, Nakajima H, Sugiyama D, Hirose I, Kitamura T, Tsuji K: Human placenta-derived cells have mesenchymal stem/progenitor cell potential. *Stem Cells* 22: 649-658 (2004).
- 62 Ganter C: Analytical solution to the transient phase of steady-state free precession sequences. *Magnetic Resonance in Medicine* 62: 149-164 (2009).
- 63 Gareau PF, Heyn C, Alejsk A, Rutt KB: Imaging single mammalian cells with 1.5T clinical MRI scanner. *Magnetic Resonance in Medicine* 49: 968-971 (2003).
- 64 Gold GE, Thedens DR, Pauly JM, Fechner KP, Bergman G, Beaulieu CF, Macovski A: MR imaging of articular cartilage of the knee: new methods using

- ultrashort TEs. American Journal of Roentgenology 170: 1223-1226 (1998).
- 65 Gowland AP, Leach OM: Fast and accurate measurements of  $T_1$  using a multi readout single inversion-recovery sequence. Magnetic Resonance in Medicine 26: 79-88 (1992).
  - 66 Haacke EM, Thomson MR, Brown RW, Venkatesan R: Magnetic Resonance Imaging: Physical Principles and Sequence Design. Wiley & Sons (1999).
  - 67 Haase A: Snapshot FLASH MRI, applications to  $T_1$ ,  $T_2$  and chemical-shift imaging Magnetic Resonance in Medicine 13: 77-89 (1990).
  - 68 Hauger O, Frost EE, Heeswijk VR, Deminie`re. C, Xue R, Delmas Y, Combe C, Moonen WTC, Grenier N, Bulte WMJ: MR Evaluation of the glomerular homing of magnetically labled mesenchymal Stem Cells in a rat model of nephropathy. Radiology 238: 200-210 (2006).
  - 69 He T, Gatehouse PD, Smith GC, Mohiaddin RH, Pennell DJ, Firmin DN. Myocardial  $T_2^*$  measurements in iron-overloaded thalassemia: An in vivo study to investigate optimal methods of quantification. Magnetic Resonance in Medicine 60: 1082-1089 (2008).
  - 70 Henning TD, Wendland MF, Golovko D, Sutton EJ, Sennino B, Malek F, Jan S. Bauer JS, McDonald DM, Daldrup-Link H: Mesenchymal stem cells at 1.5T and 3T: Discrimination of viable from lysed cells. Magnetic Resonance in Medicine 62: 325-332 (2009).
  - 71 Hill JM, Dick AJ, Raman VK, Thompson RB, Yu ZX, Hinds KA, Pessanha BS, Guttman MA, Varney TR, Martin BJ, Dunbar CE, McVeigh ER, Lederman RJ: Serial cardiac magnetic resonance imaging of injected mesenchymal stem cells. Circulation 108: 1009-1014 (2003).

- 72 Hinson HW, Sobol TW: A new method of computing spin-lattice relaxation maps in magnetic resonance imaging using fast scanning protocols. *Medical Physics* 15: 551–561 (1988).
- 73 Histoche F: Mesenchymal Stem cells: Characteristics and clinical applications. *Cytobiology* 44: 215-30 (2006).
- 74 Hobbie RK, Roth, BJ: Magnetic resonance imaging: Intermediate physics for medicine and biology. Wiley & Sons, New York (1988).
- 75 Hoehn M, Kustermann E, Blunk J, Wiedermann D, Trapp T, Wecker S, Focking M, Arnold H, Hescheler J, Fleischmann BK, Schwindt W, Buhrle C: Monitoring of implanted stem cell migration in vivo: A highly resolved in vivo magnetic resonance imaging investigation of experimental stroke in rat. *Proceeding of National Academy of Sciences USA* 99: 16267-16272 (2002).
- 76 Hofstetter CP, Schwarz EJ, Hess D, Widenfalk J, Manira A El, Prockop DJ, Olson L: Marrow stromal cells form guiding strands in the injured spinal cord and promote recovery. *Proceeding of National Academy of Sciences USA* 99: 2199-2204 (2002).
- 77 Holmes JE, Bydder GM: MR imaging with ultrashort TE (UTE) pulse sequence: Basic Principles. *Radiography* 11: 163-174 (2005).
- 78 Holzapel V, Lorenz M, Weiss KC, Schrezenmeier H, Landfester K, Mailänder V: Synthesis and biomedical applications of functionalized fluorescent and magnetic dual reporter nanoparticles as obtained in the miniemulsion process. *Journal of Physics Condensed Matter* 18: 2585-2594 (2006).
- 79 Horowitz AL: MRI physics for Physician. Springer-Verlag, New York (1989).

- 80     [http://en.wikipedia.org/wiki/Mesenchymal\\_stem\\_cell](http://en.wikipedia.org/wiki/Mesenchymal_stem_cell).
- 81     <http://stemcells.nih.gov/info/basics/basics5.asp>
- 82     <http://www.abdn.ac.uk/emunit/tem.htm>
- 83     <http://www.geos.ed.ac.uk/facilities/chem/ICP.html>
- 84     <http://www.revisemri.com/questions/basicphysics/t2star>
- 85     Hung SC, Chen NJ, Hsieh SL, Li H, Ma HL, Lo WH: Isolation and characterization of size-sieved stem cells from human bone marrow. *Stem Cells* 20: 249-258 (2002).
- 86     Ishikawa F, Drake CJ, Yang S, Fleming P, Minamiguchi H, Visconti RP, Crosby CV, Argraves W S, Harada M, Key LL Jr, Livingston AG, Wingard JR, Ogawa M: Transplanted human cord blood cells give rise to hepatocytes in engrafted mice. *Annals of the New York Academy of Sciences* 996: 174-185 (2003).
- 87     Ittrich H, Lange C, Togel F, Zander AR, Dahnke H, Westenfelder C, Adam G, Nolte-Ernsting C: In vivo magnetic resonance imaging of iron oxide-labeled, arterially-injected mesenchymal stem cells in kidneys of rats with acute ischemic kidney injury: Detection and monitoring at 3T. *Journal of Magnetic Resonance Imaging* 25: 1179-1191 (2007).
- 88     Jagielski N, Sharma S, Hombach V, Mailänder V, Rasche V, Landfester K: Nanocapsules synthesized by miniemulsion technique for application as new contrast agent material. *Macromolecular Chemistry and Physics* 208: 2229-2241 (2007).

- 89 Josan S, Pauly JM, Daniel BL, Pauly KB: Double half RF pulses for reduced sensitivity to eddy currents in UTE imaging. *Magnetic Resonance in Medicine* 61: 1083-1089 (2009).
- 90 Josephson L, Tung CH, Moore A, Weissleder R: High-efficiency intracellular magnetic labeling with novel superparamagnetic-Tat peptide conjugates. *Bioconjugate Chemistry* 10: 186-191 (1999).
- 91 Jun YW, Jang JT, Cheon J: Magnetic nanoparticle assisted molecular MR imaging. NMR in biomedicine. *Advances in Experimental Medicine and Biology* 620: 85-106 (2007).
- 92 Jung CW, Jacobs P: Physical and chemical properties of superparamagnetic iron oxide MR contrast agents: ferumoxides, ferumoxtran, ferumoxsil. *Magnetic Resonance Imaging* 13: 6610-674 (1995).
- 93 Karabulut N, Elmas N: Contrast agents used in MR imaging of the liver. *Diagnostic and Interventional Radiology* 12: 22-30 (2006).
- 94 Kay I, Henkelman RM: Practical implementation and optimization of one-shot  $T_1$  imaging. *Magnetic Resonance in Medicine* 22: 414-424 (1991).
- 95 Kenneth RN, Valerie PC: Next generation, High relaxivity Gadolinium MRI agents. *Bioconjugate Chemistry* 16: 3-8 (2005).
- 96 Kent TA, Quast MJ, Kaplan BJ, Lifsey RS, Eisenberg HM: Assessment of a superparamagnetic iron oxide (AMI-25) as a brain contrast agent. *Magnetic Resonance in Medicine* 13: 434-443 (1990).
- 97 Kerker M. Scattering of light and other electromagnetic radiation. Academic Press, New York (1969).

- 98 Koenig SH, Kellar KE: Theory of proton relaxation in solutions of magnetic nanoparticles, including the superparamagnetic size range. *Academic Radiology* 3 Suppl 2: S273-S276 (1996).
- 99 Korbliing M, Estrov Z, Champlin R: Adult stem cells and tissue repair. *Bone Marrow Transplant* 32: S23–S24 (2003).
- 100 Kostic A, Adnadjevic B, Popovic A and Jovanovic J: Comparison of the swelling kinetics of a partially neutralized poly acrylic acid hydrogel in distilled water and physiological solution. *Journal Serbian Chemical society* 72: 1139-1153 (2007).
- 101 Kramsch DM, Aspen AJ, Rozler LJ: Atherosclerosis: prevention by agents not affecting abnormal levels of blood lipids. *Science* 213: 1511–1512 (1981).
- 102 Kramsch DM, Chan CT: The effect of agents interfering with soft tissue calcification and cell proliferation of calcific fibrous-fatty plaques in rabbits. *Circulation Research* 42: 562-571 (1978).
- 103 Kuhlpete R, Dahnke H, Matuszewski L, Persigehl T, Wallbrunn AV, Allkemper T, Heindel WL, Schaeffter T, Bremer C:  $R_2$  and  $R_2^*$  Mapping for sensing cell-bound superparamagnetic nanoparticles: in vitro and murine in vivo testing. *Radiology* 245: 449-457 (2007).
- 104 Kuperman V: *Magnetic Resonance Imaging: Physical Principles and Applications*. Academic Press, San Diego, CA (2000).
- 105 Lamba NMK, Woodhouse KA, Cooper S L, Lelah MD: *Polyurethanes in Biomedical Applications*. CRC Press, US (1997).
- 106 Landfester K, Tiarks F, Hentze HP, Antonietti M: Polyaddition in miniemulsions:



- A new route to polymer dispersions. *Macromolecular Chemical Physics* 201: 1-5 (2000).
- 107 Landfester K, Willert M, and Antonietti M: Preparation of polymer particles in nonaqueous direct and inverse miniemulsions. *Macromolecules* 33: 2370-2376 (2000).
- 108 Landfester K. Generation of nanocapsules by miniemulsion processes. *Controlled Release Society Newsletter* 23: 10-11 (2006).
- 109 Landfester K: Synthesis of colloidal particles in miniemulsions. *Annual Reviews of Material Research* 36: 235-279 (2006).
- 110 Lanza GM, Lamerichs R, Caruthers S, Wickline SA: Molecular Imaging in MR with targeted paramagnetic nanoparticles. *MedicaMundi* 47: 35-39 (2003).
- 111 Lauffer RB: Paramagnetic Metal Complexes as water proton relaxation agents for NMR Imaging: Theory and Design. *Chemical Review* 87: 905-927 (1987).
- 112 Laurent S, Elst LV, Muller RN: Comparative study of the physicochemical properties of six clinical low molecular weight gadolinium contrast agents. *Contrast Media & Molecular Imaging* 1: 128-137 (2006).
- 113 Liney G: *MRI in Clinical Practice*. Springer-Verlag, London Limited (2006).
- 114 Livramento JB, Tóth E, Sour A, Borel A, Merbach AE, Ruloff R: High relaxivity confined to a small molecular space: A metallostear-based, potential MRI contrast agent. *Angewandte Chemie-International Edition* 44: 1480 -1484 (2005).
- 115 Look DC, Locker DR: Time saving in measurement of NMR and EPR relaxation times. *Review of Scientific Instruments* 41: 250-251 (1970).

- 116 Lorenz MR, Holzapfel V, Musyanovych A, Nothelfer K, Walther P, Frank H, Landfester K, Schrezenmeier H, Mailänder V: Uptake of functionalized Fluorescent-labelled polymeric particles in different cell lines and stem cells. *Biomaterials* 27: 2820-2828 (2006).
- 117 Majore I, Moretti P, Hass R, Kasper C: Identification of subpopulations in mesenchymal stem cell-like cultures from human umbilical cord. *Cell Communication and Signaling* 7: 6-14 (2009).
- 118 McCarthy JR, Weissleder R: Multifunctional magnetic nanoparticles for targeted imaging and therapy. *Advanced Drug Delivery Reviews* 60: 1245-1251 (2008).
- 119 McRobbie DW, Moore EA, Graves MJ, Prince MR: *MRI From Picture To Proton*. Cambridge University Press (2006).
- 120 Mehta CR, Jeyanthi R, Calis S, Thanoo CB, Burton WK, DeLuca PPJ: Biodegradable microspheres as depot system for parenteral delivery of peptide drugs. *Controlled Release* 29: 375-384 (1994).
- 121 Meng Y, Lei H. A single-scan  $T_2^*$  mapping method based on two gradient-echo images with compensation for macroscopic field inhomogeneity. *Magnetic Resonance in Medicine* 60: 1388-1395 (2008).
- 122 Merbach AE, Toth E: *The Chemistry of Contrast Agents in Medical Magnetic Resonance Imaging*. John Wiley & Sons, Ltd., New York (2001).
- 123 Mitchell, DG: *MRI Principles*. W.B.Saunders Company, Philadelphia (1999).
- 124 Modo MMJ, Bulte JWM: *Molecular and Cellular MR Imaging*. CRC Press Taylor & Francis Group, Danvers, MA (2007).

- 125 Morawski AM, Winter PM, Crowder KC, Caruthers SD, Fuhrhop RW, Scott MJ, Robertson JD, Abendschein DR, Lanza GM, Wickline SA: Targeted nanoparticles for quantitative imaging of sparse molecular epitopes with MRI. *Magnetic Resonance in Medicine* 51: 480-486 (2004).
- 126 Mornet S, Vasseur S, Grasset F, Duguet E: Magnetic nanoparticle design for medical diagnosis and therapy. *Journal of Materials Chemistry* 14: 2165-2175 (2004).
- 127 Mulder WJM, Strijkers GJ, Van TGAF, Griffioen AW, Nicolay K: Lipid-based nanoparticles for contrast-enhanced MRI and molecular imaging. *NMR in Biomedicine* 19: 142-164 (2006).
- 128 Muller RN, Gillis P, Moyny F, Roch A: Transverse relaxivity of particulate MRI contrast media: from theories to experiments. *Magnetic Resonance in Medicine* 22: 178-182 (1991).
- 129 Muraro PA, Ingoni RC, Martin R: Hematopoietic stem cell transplantation for multiple sclerosis: current status and future challenges. *Current Opinion in Neurology* 16: 299-305 (2003).
- 130 Musyanovych A, Schmitz-Wienke J, Mailänder V, Walther P, Landfester K: Preparation of biodegradable polymer nanoparticles by miniemulsion technique and their cell interactions. *Macromolecular Bioscience* 8: 127-139 (2008).
- 131 Muta H, Kawauchi S, Satoh M: Ion-specific swelling behaviour of uncharged poly (acrylic acid) gel. *Colloid and Polymer Science* 282: 149-155 (2003).
- 132 Nakamoto K. *Infrared and Raman Spectra of Inorganic and Coordination Compounds, Part I: Theory and Applications in Inorganic Chemistry*: Wiley, New

York (1997).

- 133 Okuhata Y: Delivery of diagnostic agents for magnetic resonance imaging  
Advanced Drug Delivery Reviews 37: 121-137 (1999).
- 134 Orlic D: Adult bone marrow stem cells regenerate myocardium in ischemic heart  
disease. Annals of the New York Academy of Sciences 996: 152-157 (2003).
- 135 OsadaY, Khokhlov AR: Polymer Gels and Networks. Marcel Dekker, INC. New  
York (2002).
- 136 Paiphansiri U, Dausend J, Musyanovych A, Mailänder V, Landfester K:  
Fluorescent polyurethane nanocapsules prepared via inverse miniemulsion: Surface  
functionalization for use as Biocarriers. Macromolecular Bioscience 9: 575-584  
(2009).
- 137 Peng XH, Qian X, Mao H, Wang AY, Chen ZG, Nie S, Shin DM: Targeted  
magnetic iron oxide nanoparticles for tumour imaging and therapy. International  
Journal of Nanomedicine 3: 315-321 (2008).
- 138 Peter C: Protein-Targeted Gadolinium-Based Magnetic Resonance Imaging (MRI)  
Contrast Agents: Design and Mechanism of Action Accounts of chemical  
Research. (Article in press) (2009).
- 139 Pfeifer H. Der Translationsanteil der Protonenrelaxation in wäßrigen Lösungen  
paramagnetischer Ionen Annalen der Physik (Leipzig) 463: 5-8 (1961).
- 140 Phinney DG, Prockop DJ: Mesenchymal stem/multipotent stromal cells: The state  
of trans differentiation and modes of tissue repair—Current Views. Stem Cells 25:  
2896-2902 (2007).
- 141 Pittenger MF, Mackay AM, Beck SC, Jaiswal RK, Douglas R, Mosca JD,

- Moorman MA, Simonetti DW, Craig S, Marshak DR: Multilineage potential of adult human mesenchymal stem cells. *Science* 284: 143-147 (1999).
- 142 Pochampally RR, Smith JR, Ylostalo J, Prockop DJ: Serum deprivation of human marrow stromal cells (h MSCs) selects for a subpopulation of early progenitor cells with enhanced expression of OCT-4 and other embryonic genes. *Blood* 103: 1647-1652 (2004).
- 143 Prasad PV: *Magnetic Resonance Imaging: Methods and Biologic Applications*. Humana press Totowa, New Jersey (2006).
- 144 Raggi P, Khan A, Arepali C, Stillman AE: Coronary artery calcium scoring in the age of CT angiography: what is its role? *Current Atherosclerosis Reports* 10: 438-443 (2008).
- 145 Rahmer J, Bornert P, Groen J, Bos C: Three-dimensional radial ultrashort echo-time imaging with T<sub>2</sub> adapted sampling. *Magnetic Resonance in Medicine* 55: 1075-1082 (2006).
- 146 Rasche V, Schreiber B, Graeff C, Istel T, Schomberg H, Grass M, Koppe R, Klotz E and Rose G. Performance of image intensifier-equipped X-ray systems for three-dimensional imaging. *International Congress Series* 1256: 187-192 (2003).
- 147 Ratajczak MZ, Zuba-Surma EK, Machalinski B, Ratajczak J, Kucia M: Very small embryonic-like (VSEL) stem cells: purification from adult organs, characterization, and biological significance. *Stem Cell Reviews and Reports* 4: 89-89 (2008).
- 148 Reichert IL, Benjamin M, Gatehouse PD, Chappell KE, Holmes J, He T, Bydder GM: Magnetic resonance imaging of periosteum with ultrashort TE pulse sequences. *Journal of Magnetic Resonance Imaging* 19: 99-107 (2004).

- 149 Reichert IL, Robson MD, Gatehouse PD, He T, Chappell KE, Holmes J, Girgis S, Bydder GM: Magnetic resonance imaging of cortical bone with ultrashort TE pulse sequences. *Magnetic Resonance Imaging* 23: 611-618 (2005).
- 150 Reimer P, Balzer T: Ferucarbotran (Resovist<sup>®</sup>): a new clinically approved RES-specific contrast agent for contrast enhanced MRI of the liver: properties, clinical development and application. *European Radiology* 13: 1266-1276 (2003).
- 151 Reimer P, Tombach B: Hepatic MRI with SPIO, detection and characterization of focal liver lesions. *European Radiology* 8:1198-1204 (1998).
- 152 Reynolds CH, Annan N, Beshah K, Huber JH, Shaber SH, Lenkinski RE, Wortman JA. Gadolinium-loaded nanoparticles: new contrast agents for magnetic resonance imaging. *Journal of American Chemical Society* 122: 8940-8945 (2000).
- 153 Robson MD, Benjamin M, Gishen P, Bydder GM: Magnetic resonance imaging of the achilles tendon using ultrashort TE (UTE) pulse sequences. *Clinical Radiology* 59: 727-735 (2004).
- 154 Robson MD, Gatehouse PD, and Bydder M, Bydder GM: Magnetic resonance: an introduction to ultrashort echo-time imaging. *Journal of Computer Assisted Tomography* 27: 1-22 (2003).
- 155 Roch A, Muller RN, Gillis P: Theory of proton relaxation induced by superparamagnetic particles. *Journal of Chemical Physics* 110: 5403-5411 (1999).
- 156 Rocklage SM, Watson AD, Carvlin MJ: Contrast agents in magnetic resonance imaging. In: *Magnetic resonance imaging*. St. Louis: Mosby Year Book, 372- 437 (1992).
- 157 Rodríguez AO: Principles of magnetic resonance imaging. *Revista Mexicana De Fisica* 50: 272-286 (2004).

- 158 Rohrer M, Bauer H, Mintorovitch J, Requardt M, Weinmann JH: Comparison of magnetic properties of MRI contrast media solutions at different magnetic field strengths. *Investigative Radiology* 40: 715-724 (2005).
- 159 Rozie S, de Weert TT, de Monyé C, Homburg PJ, Tanghe HL, Dippel DW, van der Lugt A: Atherosclerotic plaque volume and composition in symptomatic carotid arteries assessed with multidetector CT angiography; relationship with severity of stenosis and cardiovascular risk factors. *European Radiology* (article in press) (2009).
- 160 Saebo BK: Degradation, metabolism and relaxation properties of iron oxide particles for magnetic resonance imaging. Ph.d. Acta Universitatis Upsaliensis, Upsala (2004).
- 161 Santra S, Bagwe RP, Dutta D, Stanley JT, Walter GA, Tan W, Moudgil BM, Mericle RA: Synthesis and characterization of fluorescent, radio-opaque, and paramagnetic silica nanoparticles for multimodal bio imaging applications *Advanced Materials* 17: 2165- 2169 (2005).
- 162 Savitz SI, Rosenbaum DM, Dinsmore JH, Wechsler LR, Caplan LR: Cell transplantation for stroke. *Annals of Neurology* 52: 266-275 (2002).
- 163 Schafer R, Ayturan M, Bantleon R, Kehlbach R, Siegel G, Pintaske J, Conrad S, Wolburg H, Northoff H, Wiskirchen J, Weissert R: The use of clinically approved small particles of iron oxide (SPIO) for labeling of mesenchymal stem cells aggravates clinical symptoms in experimental autoimmune Encephalomyelitis and influences their in vivo distribution. *Cell Transplantation* 17: 923-941 (2008).
- 164 Scheffler K, Hennig J:  $T_1$  quantification with inversion recovery True-FISP. *Magnetic Resonance in Medicine* 45: 720-723 (2001).

- 165 Schick F, Pintaske J, Martirosian P, Graf H , Erb G, Lodemann KP, Claussen CD: Relaxivity of gadopentetate dimeglumine, gadobutrol and gadobenate dimeglumine in human blood plasma at 0.2, 1.5 and 3T. *Contrast Media & Molecular Imaging* 1: 52-92 (2006).
- 166 Schlaad H, Kukula H, Rudloff J, Below I: Synthesis of  $\alpha,\omega$ -heterobifunctional poly(ethylene glycol)s by metal-free anionic ring-opening polymerization. *Macromolecules* 34: 4302-4304 (2001).
- 167 Schmidtke-Schrezenmeier G: Iron labeling of mesenchymal stem/stromal cells for magnetic resonance imaging: Studies on poly-L-lactic acid-iron nanoparticles. Dissertation, University of Ulm, Ulm (2009).
- 168 Schwertmann U, Cornell RM: Iron oxides in the laboratory. Weinheim NewYork-Basel-Cambridge: VCH Verlagsgesellschaft GmbH (1991).
- 169 Settle F: Handbook of instrumental techniques for analytical chemistry. Prentice Hall, New Jersey (1997).
- 170 Shake JG, Gruber PJ, Baumgartner WA, Senechal G, Meyers J, Redmond JM, Pittenger MF, Martin BJ: Mesenchymal stem cell implantation in a swine myocardial infarct model: engraftment and functional effects. *The Annals of Thoracic Surgery* 73: 1919-1925; discussion 1926 (2002).
- 171 Sharma S, Boujraf S, Bornstedt A, Rasche V: Quantification of Calcifications in Endarterectomy Samples by Means of High-resolution Ultra-short TE Imaging. In *Proceedings Annual Meeting ISMRM, Honolulu*, 833 (2009).
- 172 Shellock FG, Parker JR, Venetianer C, Pirovano G, Spinazzi A: Safety of Gadobenate Dimeglumine (MultiHance) *Investigative Radiology* 41: 500-509



(2006).

- 173 Shen T, Weissleder R, Papisov M, Bogdanov A Jr, Brady TJ: Monocrystalline iron oxide nano compounds (MION): physicochemical properties. *Magnetic Resonance Medicine* 29: 599-604 (1993).
- 174 Simamora P, Chern W: Poly-L-Lactic acid: an overview. *Journal of Drugs in Dermatology* 5: 436-440 (2006).
- 175 Skoog DA, West DM, Holler FJ, Crouch SR: *Fundamentals of analytical chemistry*. Brooks/Cole, USA (2004).
- 176 Smith JR, Pochampally R, Perry A, Hsu SC, Prockop DJ: Isolation of a highly clonogenic and multipotential subfraction of adult stem cells from bone marrow stroma. *Stem Cells* 22: 823-831 (2004).
- 177 Solomon I: Relaxation Processes in a System of Two Spins. *Physical Review* 99: 559-565 (1955).
- 178 Sosnovik DE, Nahrendorf M, Weissleder R: Magnetic nanoparticles for MR imaging: agents, techniques and cardiovascular applications. *Basic Research in cardiology* 103: 122-130 (2008).
- 179 Strobl G: *The Physics of Polymers Concepts for Understanding Their Structures and Behaviour*. Springer-Verlag, Berlin, Germany (1997).
- 180 Sykova E, Jendelova P: Migration, fate and in vivo imaging of adult stem cells in the CNS. *Cell Death and Differentiation* 14: 1336-1342 (2007).
- 181 Tanimoto A, Koichi O, Suematsu M, Pouliquen D, Stark DD: Relaxation effects of clustered particles. *Journal of Magnetic Resonance Imaging* 14: 72-77 (2001).

- 182 Taylor AM, Panting JR, Keegan J, Gatehouse PD, Amin D, Jhooti P, Yang GZ, McGill S, Burman ED, Francis JM, Firmin DN, Pennell DJ: Safety and preliminary findings with the intravascular contrast agent NC100150 injection for MR coronary angiography. *Journal of magnetic resonance imaging* 9: 220- 227 (1999).
- 183 Terrovitis JV, Bulte JW, Sarvananthan S, Crowe LA, Sarathchandra P, Batten P, Sachlos E, Chester AH, Czernuszka JT, Firmin DN, Taylor PM, Yacoub MH: Magnetic resonance imaging of ferumoxide-labeled mesenchymal stem cells seeded on collagen scaffolds—relevance to tissue engineering. *Tissue Engineering* 12: 2765-2775 (2006).
- 184 Tiarks F, Landfester K, and Antonietti M: Preparation of polymeric nanocapsules by miniemulsion polymerization. *Langmuir* 17: 908-918 (2001).
- 185 Tofts. P: Quantitative MRI of the brain. Measuring changes caused by disease. John Wiley & Sons Ltd England (2003).
- 186 Toma C, Pittenger MF, Cahill KS, Byrne BJ, Kessler PD: Human mesenchymal stem cells differentiate to a cardiomyocyte phenotype in the adult murine heart *Circulation* 105: 93-98 (2002).
- 187 Tombach B, Reimer P, Bremer C, Allkemper T, Engelhardt M, Mahler M, Ebert W, Heindel W: First pass and equilibrium MRA of the aortoiliac region with a superparamagnetic iron oxide blood pool MR contrast agent SH U 555 C, results of a human pilot study. *NMR in Biomedicine* 17: 500-506 (2004).
- 188 Toth E, Helm L, Merbach AE: Relaxivity of MRI contrast agents. *Topics in Current Chemistry* 221 (Contrast Agents I): 61-101. Springer Berlin/Heidelberg (2002).
- 189 Turner JL, Pan D, Plummer R, Chen Z, Whittaker AK, Wooley KL: Synthesis of a

- gadolinium-labeled shell crosslinked nanoparticle for magnetic resonance imaging applications. *Advance Functional Materials* 15: 1248-1254 (2005).
- 190 Tyler DJ, Robson MD, Henkelman RM, Young IR, Bydder GM: Magnetic resonance imaging with ultrashort TE (UTE) PULSE sequences: Technical considerations. *Journal of Magnetic Resonance Imaging* 25: 279-289 (2007).
  - 191 Uccelli A, Moretta L, Pistoia V: Mesenchymal stem cells in health and disease *Nature Reviews Immunology* 8: 726-36 (2008).
  - 192 Unger E, Shen DK, Wu G, Fritz T: Liposomes as MR contrast agents: pros and cons. *Magnetic Resonance in Medicine* 22: 304-308 (1991).
  - 193 Verfaillie CM, Schwartz R, Reyes M, Jiang Y: Unexpected potential of adult stem cells. *Annals of the New York Academy of Sciences* 996: 235-234 (2003).
  - 194 Virmani R, Narula J, Leon MB, Willerson JT: *The Vulnerable Atherosclerotic Plaque: Strategies for Diagnosis and Management*. Blackwell Publishing (2007).
  - 195 Vladimir PT: Polymeric Contrast Agents for Medical Imaging. *Current Pharmaceutical Biotechnology* 1: 183-215 (2000).
  - 196 Waldman A, Rees JH, Brock CS, Robson MD, Gatehouse PD, Bydder GM: MRI of the brain with ultra-short echo-time pulse sequences. *Neuroradiology* 45: 887-892 (2003).
  - 197 Wallis de Vries BM, van Dam GM, Tio RA, Hillebrands JL, Slart RH, Zeebregts CJ: Current imaging modalities to visualize vulnerability within the atherosclerotic carotid plaque. *Journal of Vascular Surgery* 48: 1620-1629 (2008).
  - 198 Wang YX, Hussain SM, Krestin GP, Bonnemain B: Superparamagnetic agents in

- magnetic resonance imaging: physicochemical characteristics and clinical applications: A review. *Journal of Drug Targeting* 6: 167-174 (1998).
- 199 Wang YX, Hussain SM, Krestin GP: Superparamagnetic iron oxide contrast agents: physicochemical characteristics and applications in MR imaging. *European radiology* 11: 2319-2331 (2001).
  - 200 Watson KE, Demer LL: The atherosclerosis-calcification link? Current opinion in lipidology 7: 101-104 (1996).
  - 201 Weishaupt D, Koechli VD, Marincek B: How Does MRI Work? An Introduction to the Physics and Function of Magnetic Resonance Imaging Springer- Verlag, Berlin Heidelberg New York (2006).
  - 202 Weiss CK, Lorenz MR, Landfester K, Mailänder V: Cellular uptake behaviour of unfunctionalized and functionlaized PBCA particles prepared in a miniemulsion. *Macromolecular Bioscience* 7: 883-896 (2007).
  - 203 Weissleder R, Elizondo G, Wittenberg J, Rabito CA, Bengele HH, Josephson L: Ultrasmall superparamagnetic iron oxide: characterization of a new class of contrast agents for MR imaging. *Radiology* 175: 489-493 (1990).
  - 204 Werner EJ, Datta A, Jocher CJ, Raymond KN: High-Relaxivity MRI Contrast Agents: Where Coordination Chemistry Meets Medical Imaging. *Angewandte Chemie-International Edition* 47: 8568-8580 (2008).
  - 205 Westbrook C, Roth KR, Talbot J: MRI in practice. Blackwell Science (1998).
  - 206 Wiener E, Brechbiel MW, Brothers H, Magin RL, Gansow OA, Tomalia DA, Lauterbur PC: Dendrimer-based metal chelates: A new class of magnetic resonance imaging contrast agents. *Magnetic Resonance in Medicine* 31: 5- 8 (1994).

- 207     Wikipedia: Energy Filtered Transmission Electron Microscopy  
         [http://en.wikipedia.org/wiki/Energy\\_filtered\\_transmission\\_electron\\_microscopy](http://en.wikipedia.org/wiki/Energy_filtered_transmission_electron_microscopy)
- 208     Wikipedia: Gel  
         <http://en.wikipedia.org/wiki/Gel>
- 209     Wikipedia: Scanning Transmission Electron Microscopy  
         [http://en.wikipedia.org/wiki/Scanning\\_Transmission\\_Electron\\_Microscope](http://en.wikipedia.org/wiki/Scanning_Transmission_Electron_Microscope)
- 210     Wikipedia: Transmission Electron Microscopy  
         [http://en.wikipedia.org/wiki/Transmission\\_electron\\_microscope](http://en.wikipedia.org/wiki/Transmission_electron_microscope)
- 211     Winter PM, Caruthers SD, Yu X, Song SK, Chen J, Miller B, Bulte JWM, Robertson JD, Gaffney PJ, Wickline SA, Lanza GM: Improved molecular imaging contrast agent for detection of human thrombus. *Magnetic Resonance in Medicine* 50: 415-416 (2003).
- 212     Wnek GE, Bowlin GL: *Encyclopaedia of Biomaterials and Biomedical Engineering*. Informa health care, New York (2008).
- 213     Wu EX, Tang H, Jensen JH: Review Article Applications of ultrasmall superparamagnetic iron oxide contrast agents in the MR study of animal models. *NMR in Biomedicine* 17: 478-483 (2004).
- 214     [www.malvern.com/dynamic light scattering](http://www.malvern.com/dynamic_light_scattering).
- 215     Xiang Y, Wang J, Shahid HM, Gabriel KP: Superparamagnetic iron oxide contrast agents: Physiochemical characteristics and applications in MR imaging. *European Radiology* 11: 2319-2331 (2001).

- 216 Yeh TC, Zhang W, Ildstad ST, Ho C: In vivo dynamic MRI tracking of rat T-cells labeled with superparamagnetic iron-oxide particles. *Magnetic Resonance in Medicine* 33: 200-208 (1995).
  
- 217 Zhang TY, Yeung NH, Carson LP, Ellis HJ. Experimental analysis of  $T_1$  imaging with a single-scan, multiple-point, inversion-recovery technique. *Magnetic Resonance in Medicine* 25: 337-343 (1991).
  
- 218 Zimmerman SC, Zeng F, David ECR, Sergei VK: Self-Assembling Dendrimers. *Science* 271: 1095-1098 (1996).

## Appendix A

Details about  $T_1$  data used for calculating the relaxivities of different types of gadolinium based contrast agents (chapter 3) with and without encapsulation

Table A.1: Concentration (mmol/L) and  $T_1$  (ms) values of Polyurethane, Polyurea and Dextran encapsulated Magnevist® nanocapsules along with their relaxivity values.

Gd <sup>3+</sup> concentration for PU encapsulated Magnevist®	$T_1$ (ms)	$T_1$ (ms)	$T_1$ (ms)	$T_1$ (ms)
0.6	333.34	333.6	333.99	337.89
0.3	601.262	601.26	601.84	605.13
0.15	991.276	991.16	988.14	984.66
0.09	1378	1380	1320	1330
0.06	1603	1600	1590	1580
0	2600	2600	2600	2600
	$r_1 = 4.39$	$r_1 = 4.38$	$r_1 = 4.36$	$r_1 = 4.30$
Mean $r_1 = 4.35 \pm 0.035$				

Table A.1: Concentration (mmol/L) and  $T_1$  (ms) values of Polyurethane, Polyurea and Dextran encapsulated Magnevist<sup>®</sup> nanocapsules along with their relaxivity values. **Continued.....**

Gd <sup>3+</sup> concentration for dextran encapsulated Magnevist <sup>®</sup>	$T_1$ (ms)	$T_1$ (ms)	$T_1$ (ms)	$T_1$ (ms)
0.4775	396.68	402.0	397.25	407.98
0.2387	702.3	730.76	720.66	730.29
0.1193	1132	1150	1133	1130
0.0596	1628	1550	1480	1510
0	2600	2600	2600	2600
	$r_1 = 4.50$	$r_1 = 4.40$	$r_1 = 4.43$	$r_1 = 4.30$
Mean $r_1 = 4.40 \pm 0.080$				
Gd <sup>3+</sup> concentration for polyurea encapsulated Magnevist <sup>®</sup>	$T_1$ (ms)	$T_1$ (ms)	$T_1$ (ms)	$T_1$ (ms)
0.5164	356.74	356.3	359.92	357.85
0.2582	636.51	635.9	637.22	636.91
0.1291	1042	1043	1041	1041
0.0645	1421	1421	1410	1391
0.0322	1679	1670	1630	1680
0	2600	2600	2600	2600
	$r_1 = 4.62$	$r_1 = 4.63$	$r_1 = 4.56$	$r_1 = 4.60$
Mean $r_1 = 4.60 \pm 0.027$				



Table A.2: Concentration (mmol/L) and  $T_1$  (ms) values of Gadovist<sup>®</sup> and Multihance<sup>®</sup> nanocapsules along with their relaxivity values.

Gd <sup>3+</sup> concentration for PU encapsulated Gadovist <sup>®</sup>	$T_1$ (ms)	$T_1$ (ms)	$T_1$ (ms)	$T_1$ (ms)
0.55	335.515	335.51	339.72	337.54
0.275	638.907	638.9	626.27	632
0.1375	1062	1067	1059	1050
0.0825	1483	1460	1410	1410
0.055	1728	1740	1680	1700
0	2600	2600	2600	2600
	$r_1 = 4.77$	$r_1 = 4.77$	$r_1 = 4.69$	$r_1 = 4.72$
Mean $r_1 = 4.73 \pm 0.035$				
Gd <sup>3+</sup> concentration for PU encapsulated Multihance <sup>®</sup>	$T_1$ (ms)	$T_1$ (ms)	$T_1$ (ms)	$T_1$ (ms)
0.4	380	381	382.5	382
0.2	700	704.32	701.0	689.32
0.1	1150	1.15	1.11	1.08
0.06	1536	1.53	1.42	1.43
0.04	1829	1.82	1.74	1.72
0	2600	2600	2600	2600
	$r_1 = 5.70$	$r_1 = 5.67$	$r_1 = 5.58$	$r_1 = 5.60$
Mean $r_1 = 5.64 \pm 0.18$				

Table A.3: Concentration (mmol/L) and  $T_1$  (ms) values of non encapsulated Magnevist<sup>®</sup>, Gadovist<sup>®</sup> and Multihance<sup>®</sup> along with their relaxivity values.

Gd <sup>3+</sup> concentration for non nonencapsulated Magnevist <sup>®</sup>	$T_1$ (ms)	$T_1$ (ms)	$T_1$ (ms)	$T_1$ (ms)
1	222.76	224.53	224.22	223.9
0.5	402.84	402.84	409.86	415.18
0.25	704.31	704.31	712.64	715.31
0.125	1108	1110	1130	1110
0	2600	2600	2600	2600
	$r_1 = 4.10$	$r_1 = 4.075$	$r_1 = 4.082$	$r_1 = 4.077$
Mean $r_1 = 4.08 \pm 0.10$				
Gd <sup>3+</sup> concentration for non nonencapsulated Gadovist <sup>®</sup>	$T_1$ (ms)	$T_1$ (ms)	$T_1$ (ms)	$T_1$ (ms)
1	209.76	211.48	212.78	209.44
0.5	389.91	392.84	394.43	389.91
0.25	705.49	709.6	703.41	707.85
0.125	1091	1100	1100	1089
0	2610	2610	2610	2600
	$r_1 = 4.40$	$r_1 = 4.36$	$r_1 = 4.33$	$r_1 = 4.40$
Mean $r_1 = 4.37 \pm 0.033$				
Gd <sup>3+</sup> concentration for non nonencapsulated Multihance <sup>®</sup>	$T_1$ (ms)	$T_1$ (ms)	$T_1$ (ms)	$T_1$ (ms)
1.25	132.09	132.48	137.21	135.95
0.5	319.85	319.85	324.53	324.24
0.25	574.67	573.91	581.12	579.58
0.125	964.68	964.08	973.33	964.30
0	2600	2600	2600	2600
	$r_1 = 5.77$	$r_1 = 5.75$	$r_1 = 5.54$	$r_1 = 5.60$
Mean $r_1 = 5.63 \pm 0.08$				

Table A.4: Concentration (mmol/L) and  $T_1$  (ms) values of Magnevist<sup>®</sup> loaded polyurethane nanocapsules synthesized using different amount of diol: TDI.

Gd <sup>3+</sup> concentration for PU encapsulated Magnevist <sup>®</sup> synthesized with diol: TDI 1:4	$T_1$ (ms)	$T_1$ (ms)	$T_1$ (ms)	$T_1$ (ms)
0.9803	208.59	208.94	207.9	209
0.4901	392.26	391.61	391.8	391
0.2451	686.83	680.099	684.92	673
0.1225	1050	1051	1048	1030
0.0613	1540	1540	1540	1530
0	2600	2600	2600	2600
	$r_I = 4.50$	$r_I = 4.48$	$r_I = 4.50$	$r_I = 4.47$
Mean $r_I = 4.48 \pm 0.01$				
Gd <sup>3+</sup> concentration for PU encapsulated Magnevist <sup>®</sup> synthesized with diol: TDI 1:8	$T_1$ (ms)	$T_1$ (ms)	$T_1$ (ms)	$T_1$ (ms)
0.974	215.8	215.17	215.62	211
0.487	408.75	408.03	408.04	386
0.244	668.03	676.98	671.9	662
0.122	1050	1054	1049	1080
0.061	1550	1550	1560	1619.9
0	2600	2600	2600	2600
	$r_I = 4.33$	$r_I = 4.35$	$r_I = 4.34$	$r_I = 4.50$
Mean $r_I = 4.37 \pm 0.06$				

Table A.4: Concentration (mmol/L) and  $T_I$  (ms) values of Magnevist<sup>®</sup> loaded polyurethane nanocapsules synthesized using different amount of diol: TDI. **Continued.....**

Gd <sup>3+</sup> concentration for PU encapsulated Magnevist <sup>®</sup> synthesized with diol: TDI 1:10	$T_I$ (ms)	$T_I$ (ms)	$T_I$ (ms)	$T_I$ (ms)
0.436	436.68	436.57	429.41	436.68
0.218	734.80	734.78	742.87	740.28
0.109	1186	1186	1170	1184
0.055	1600	1620	1630	1720
0.027	1990	1960	2090	2196
0	2600	2600	2600	2600
	$r_I = 4.39$	$r_I = 4.38$	$r_I = 4.49$	$r_I = 4.44$
Mean $r_I = 4.40 \pm 0.044$				

Table A.5: Concentration (mmol/L) and  $T_I$  (ms) values of nanocapsules synthesized using Magnevist<sup>®</sup> and TDI.

Gd <sup>3+</sup> concentration for nanocapsules synthesized using Magnevist <sup>®</sup> + TDI	$T_I$ (ms)	$T_I$ (ms)	$T_I$ (ms)	$T_I$ (ms)
0.988	210.87	208.62	208.89	211.5
0.494	388.59	376.96	365.79	386
0.247	674.25	666.15	675.26	662
0.123	1009	1095	1030	1080
0.062	1630	1640	1640	1619
0	2600	2600	2600	2600
	$r_I = 4.43$	$r_I = 4.50$	$r_I = 4.50$	$r_I = 4.41$
Mean $r_I = 4.46 \pm 0.040$				

Table A.6: Concentration and  $T_I$  values of Polyurethane encapsulated Multihance<sup>®</sup> in plasma medium along with nonencapsulated Multihance<sup>®</sup> in plasma medium.

Gd <sup>3+</sup> concentration for nonencapsulated Multihance <sup>®</sup> in plasma	$T_I$ (ms)	$T_I$ (ms)	$T_I$ (ms)	$T_I$ (ms)
1.25	105.37	103.75	103.25	105.5
0.50	237.26	234.70	237.26	237.2
0.25	420.45	417.15	418.71	420.5
0.125	697.35	688.53	689.76	694.8
0	1610	1610	1610	1610
	$r_I = 7.12$	$r_I = 7.24$	$r_I = 7.28$	$r_I = 7.113$
Mean $r_I = 7.18 \pm 0.055$				
Gd <sup>3+</sup> concentration for PU encapsulated Multihance <sup>®</sup> in plasma	$T_I$ (ms)	$T_I$ (ms)	$T_I$ (ms)	$T_I$ (ms)
0.751	204.7	204.74	204.005	204.09
0.626	226.8	226.84	221.54	224.35
0.418	257.2	257.16	251.08	251.05
0.210	379.2	380.00	381.05	378.84
0	1388	1388	1388	1388
	$r_I = 5.43$	$r_I = 5.43$	$r_I = 5.52$	$r_I = 5.48$
Mean $r_I = 5.46 \pm 0.038$				

Table A.7: Concentration and  $T_I$  values of Dextran encapsulated Multihance<sup>®</sup> in plasma and water medium.

Gd <sup>3+</sup> concentration for dextran encapsulated Multihance <sup>®</sup> in plasma	$T_I$ (ms)	$T_I$ (ms)	$T_I$ (ms)	$T_I$ (ms)
0.593	259.1	259.14	257.28	259.10
0.555	269.5	269.09	266.04	267.69
0.494	289.8	289.76	287.07	290.30
0.412	316.0	316.02	315.27	314.59
0	1388	1388	1388	1388
	$r_I = 5.61$	$r_I = 5.62$	$r_I = 5.55$	$r_I = 5.55$
Mean $r_I = 5.58 \pm 0.032$				
Gd <sup>3+</sup> concentration for dextran encapsulated Multihance <sup>®</sup> in water	$T_I$ (ms)	$T_I$ (ms)	$T_I$ (ms)	$T_I$ (ms)
0.413	386.21	383.96	376.86	386.21
0.165	829.37	774.80	790.81	842.21
0.0826	1280	1260	1270	1290
0	2600	2600	2600	2600
	$r_I = 5.38$	$r_I = 5.41$	$r_I = 5.54$	$r_I = 5.38$
Mean $r_I = 5.42 \pm 0.066$				

## Appendix B

Details about  $T_1$  data used for calculating the relaxivities of Magnevist<sup>®</sup> contrast agent (chapter 3-Part B) loaded in nanocapsules synthesized by using gel approach.

Table B.1: Concentration (mmol/L) and  $T_1$  (ms) values of Magnevist<sup>®</sup> encapsulated in nanocapsules synthesized by using PAAm gel.

Gd <sup>3+</sup> concentration for dialyzed UPN 5 sample	$T_1$ (ms)	$T_1$ (ms)	$T_1$ (ms)	$T_1$ (ms)
0.56305	205.895	205.2	204.7	206.2
0.281525	477.989	477.92	476.9	476.5
0.140763	1024	1021	1020.3	1022
0.070381	1510	1509	1506	1509
0	2600	2600	2600	2600
	$r_1 = 8.14$	$r_1 = 8.16$	$r_1 = 8.19$	$r_1 = 8.13$
Mean $r_1 = 8.15 \pm 0.023$				

Table B.1 Concentration (mmol/L) and  $T_1$  (ms) of Magnevist® encapsulated in nanocapsules synthesized by using PAAm gel. **Continued .....**

Gd <sup>3+</sup> concentration for dialyzed UPN 7	$T_1$ (ms)	$T_1$ (ms)	$T_1$ (ms)	$T_1$ (ms)
0.50565	229.466	229	228.3	231.7
0.252825	542.8	540.2	539.8	541.3
0.126413	1058	1056	1055	1052
0.063206	1549	1542	1537	1537
0	2600	2600	2600	2600
	$r_I = 8.00$	$r_I = 8.024$	$r_I = 8.04$	$r_I = 7.91$
Mean $r_I = 7.99 \pm 0.05$				
Gd <sup>3+</sup> concentration for dialyzed UPN 8	$T_1$ (ms)	$T_1$ (ms)	$T_1$ (ms)	$T_1$ (ms)
1.0325	230.00	229	231.2	229.3
0.51625	515.795	514.8	515.3	514.1
0.258125	10619	1060	1062	1060
0.129063	15414	1543	1541	1539
0.064531	2600	2600	2600	2600
	$r_I = 7.85$	$r_I = 7.89$	$r_I = 7.81$	$r_I = 7.88$
Mean $r_I = 7.85 \pm 0.0311$				
Gd <sup>3+</sup> concentration for dialyzed UPN 3	$T_1$ (ms)	$T_1$ (ms)	$T_1$ (ms)	$T_1$ (ms)
0.53945	206.456	206.1	205.8	205.91
0.269725	453.47	452.1	451.4	452
0.134863	10045	10042	1004	1005.4
0.067431	15059	1501	1504	1506
0	2600	2600	2600	2600
	$r_I = 8.50$	$r_I = 8.52$	$r_I = 8.39$	$r_I = 8.53$
Mean $r_I = 8.48 \pm 0.055$				



Table B.2: Concentration and  $T_I$  values of Magnevist<sup>®</sup> encapsulated in nanocapsules synthesized by using PAA gel.

Gd <sup>3+</sup> concentration for dialyzed UPN 9	$T_I$ (ms)	$T_I$ (ms)	$T_I$ (ms)	$T_I$ (ms)
0.367	320.53	321.35	318.98	320.92
0.183	771.86	771.46	772.07	763.10
0.091	1280	1300	1298	1294
0.045	1715	1770	1790	1780
0	2600	2600	2600	2600
	$r_I = 7.51$	$r_I = 7.51$	$r_I = 7.58$	$r_I = 7.53$
Mean $r_I = 7.53 \pm 0.032$				
Gd <sup>3+</sup> concentration for dialyzed UPN10	$T_I$ (ms)	$T_I$ (ms)	$T_I$ (ms)	$T_I$ (ms)
0.506	227.9	231.69	235.46	233.58
0.253	553.71	558.79	565.51	559.37
0.126	1077	1088	1082	1104
0.063	1531	1550	1600	1610
0	2600	2600	2600	2600
	$r_I = 8.04$	$r_I = 7.90$	$r_I = 7.77$	$r_I = 7.85$
Mean $r_I = 7.89 \pm 0.098$				
Gd <sup>3+</sup> concentration for dialyzed UPN12	$T_I$ (ms)	$T_I$ (ms)	$T_I$ (ms)	$T_I$ (ms)
0.627	198.05	197.57	197.04	196.22
0.313	455.35	455.68	455.27	449.17
0.156	961.732	972	967	952
0.078	1464	1480	1460	1480
0	2600	2600	2600	2600
	$r_I = 7.61$	$r_I = 7.64$	$r_I = 7.65$	$r_I = 7.70$
Mean $r_I = 7.65 \pm 0.032$				

Table B.2: Concentration and  $T_I$  values of Magnevist<sup>®</sup> encapsulated in nanocapsules synthesized by using PAA gel. **Continued.....**

Gd <sup>3+</sup> concentration for dialyzed UPN13	$T_I$ (ms)	$T_I$ (ms)	$T_I$ (ms)	$T_I$ (ms)
0.501	237.58	237.78	237.64	235.82
0.250	543.76	547.47	544.08	543.85
0.125	1073	1079	1070	1080
0.062	1573	1590	1590	1600
0	2600	2600	2600	2600
	$r_I = 7.80$	$r_I = 7.78$	$r_I = 7.79$	$r_I = 7.86$
Mean $r_I = 7.80 \pm 0.031$				

## Appendix C

Details about synthesis procedure of iron-PLLA nanoparticles and phantom preparation in Agarose gel (Chapter-4) are provided in this section.

For work presented in chapter 4- synthesis of iron-PLLA nanoparticles was done by Markus Urban, MPI Mainz. This synthesis procedure was provided by him and is as follows:

### C.1 Synthesis of Iron loaded nanoparticles by the process of miniemulsion Materials<sup>\*\*</sup>

Ferric chloride hexahydrate ( $\text{FeCl}_3 \cdot 6 \text{H}_2\text{O}$ , Merck, 99%), oleic acid (Riedel-de Haen, 58%), methanol (Merck, 98.5%), sodium hydroxide (Merck, 99%), 1-octadecane (Merck, 92%), acetone (Merck, 99%), n-octane (Fluka, 95%), Biomer<sup>®</sup>L9000 supplied by Biomer, Germany ( $M_n \sim 66500 \text{ g} \cdot \text{mol}^{-1}$ ,  $M_w \sim 145000 \text{ g} \cdot \text{mol}^{-1}$  determined by GPC in chloroform), chloroform (Fisher Scientific, 99.99%), sodium n-dodecyl sulphate (Alfa Aesar, 99%), cetyltrimethylammonium chloride (CTMA-Cl, 25% solution in water, Fluka), N-(2,6-diisopropylphenyl)-perylene-3,4-dicarbonacid-imide (PMI) (BASF) and hydrochloric acid 37% (Prolabo, AnalaR NORMAPUR). All chemicals were used as received. Demineralised (demin.) water was used throughout the work.

#### Preparation of poly (L-lactide) particles with encapsulated iron oxide

The synthesis of iron oxide particles was performed according to [A]. PLLA (300 mg), PMI (0.23 mg) and different amounts of iron oxide were dispersed in chloroform (10 g) at 40 °C and mixed afterwards with a solution consisting of water (24 g) and SDS (72 mg) or CTMA-Cl (125 mg). After mechanical stirring for one hour at 500 rpm, the miniemulsion was prepared by ultrasonification for 180 sec (30 s pulse, 10 s pause) at 70% amplitude using Branson sonifier W450 Digital, 1/2" tip under ice cooling in

order to prevent the evaporation of chloroform. The miniemulsion was transferred into the round bottom flask with a wide neck and heated at 40 °C under mechanical stirring (400 rpm) over night to evaporate chloroform (Fig.C.1). To remove non-encapsulated iron oxide the sample was first centrifuged at 2000 rpm for 20 minutes and then the upper phase was transferred into another tube. The sample was dialyzed using Millipore Centrifugal Filter Devices with 100000 MWCO, 2500 rpm for 30 min until the conductivity was below 9  $\mu\text{S}/\text{cm}$ .

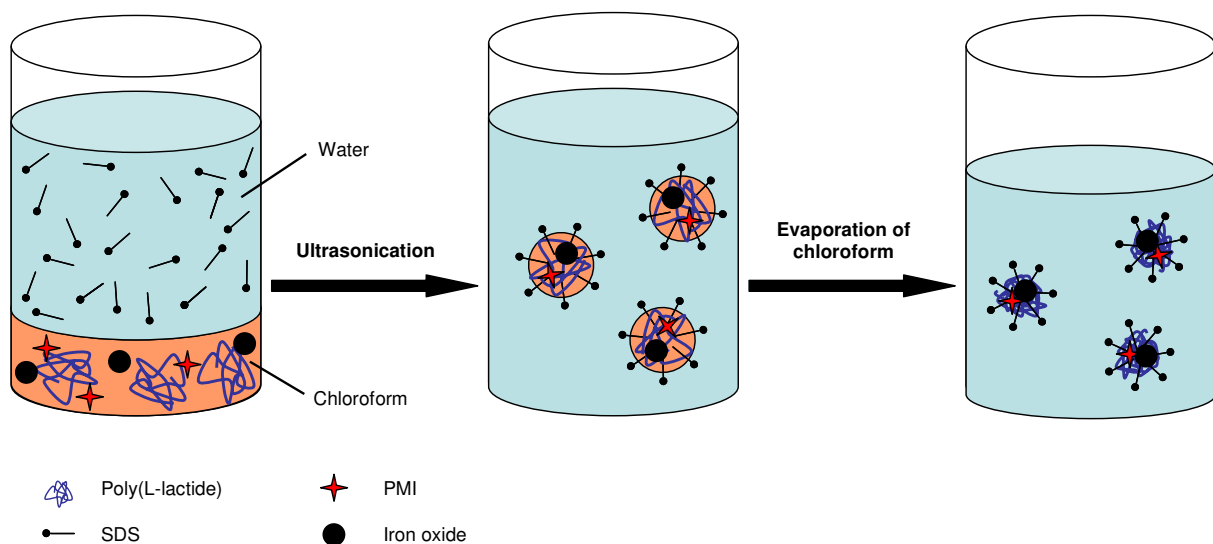


Fig.C.1 Schematic representation of magnetite and fluorescent dye encapsulation into PLLA particles.

[ A ] N. R. Jana, Y. F. Chen, X. G. Peng, *Chemistry of Materials* **2004**, 16, 3931.

Table C.1 General Protocol for  $T_2^*$  measurement at 3T.

<b>Parameter</b>	<b><math>T_2^*</math> experiment</b>	<b><math>T_2^*</math> experiment</b>
Total scan duration	40:01 min	4 hr 2 min 41 sec
Resolution	0.5 x 0.5 x 8 mm	0.25 x 0.25 x 8 mm
Act TR/TE delta TE(ms)	500/2.5/4.3	650/4/7.4
Acq matrix M x P	400 x 400	800 x 800
Acq voxel MPS(mm)	0.5/0.5/8.0	0.25/0.25/8.0
Rec.voxel MPS(mm)	0.5/0.5/8.0	0.25/0.25/8.0
Act.WFS(pix)/BW(Hz)	0.695/625.0	1.341/324.1
Min WFS(pix)/Max B	0.693/627.0	1.317/330
Min TR/TE/delta TE	69/2.5/4.3	236/4.0/7.4
NSA	12	28
Reconstruction Matrix	400	800
FOV	210 mm	210 mm
Slice thickness	8 mm	8 mm

Table C.2 General Protocol for  $T_2$  measurement at 3T.

<b>Parameter</b>	<b><math>T_2</math> experiment</b>	<b><math>T_2</math> experiment</b>
Total scan duration	1 h 46 min 42 sec	8 h 38 min 43 sec
Resolution	0.5 x 0.5 x 8 mm	0.25 x 0.25 x 8 mm
Act TR	1500	1500
Acq matrix M x P	400 x 400	740 x 740
Acq voxel MPS(mm)	0.5/0.5/8.0	0.25/0.25/8.0
Rec.voxel MPS(mm)	0.5/0.5/8.0	0.25/0.25/8.0
Min TR	1138	1138
B <sub>1</sub> rms (μT)	1.4	1.4
Act TE	8 x 10	8 x 12
NSA	10	28

For work presented in chapter 4 all the phantoms in agarose gel were prepared by Ms Gerlinde Schmidtke-Schrezenmeier (Clinic of Dermatology and Allergology of the University Hospital Ulm). All the details presented in this section were provided by her.

Table C.3: Details of phantom preparation for different types of iron –PLLA nanoparticles (Batch I). Iron normalization was done on the basis of Fe content obtained from ICP-OES.

	Resovist®	Fe Conc. in 2 ml Agarose	MU 119-5zdz	Fe Conc. in 2 ml Agarose
Stock Solution	2µl in 2 ml PBS = 28µg Fe/ml	625 µl in 2ml Agarose = 6.6 µg Fe/ml	23,8 µl in 1979µl PBS= 28µg Fe/ml	625 µl in 2 ml Agarose = 6.6 µg Fe/ml
Dilution 1	1 ml Stock Solution + 1ml PBS = 14 µg Fe/ml	625 µl in 2 ml Agarose = 3.3 µg Fe/ml	1ml Stock Solution + 1 ml PBS = 14 µg Fe/ml	625 µl in 2 ml Agarose = 3.3 µg Fe/ml
Dilution 2	1 ml Dilution 1 + 1 ml PBS = 7 µg Fe/ml	625 µl in 2ml Agarose = 1.66 µg Fe/ml	1 ml Dilution 1 + 1ml PBS = 7 µg Fe/ml	625 µl in 2 ml Agarose = 1.66 µgFe/ml
Dilution 3	1ml Dilution 1 + 1ml PBS = 3,5 µg/Fe/ml	625 µl in 2ml Agarose = 0,833 µg Fe/ml	1 ml Dilution 2 + 1ml PBS = 3.5 µg Fe/ml	625 µl in 2 ml Agarose = 0.833 µg Fe/ml
	MU 119-1zd N2	Fe Conc. in 2 ml Agarose	MU 128-1zd	Fe Conc. in 2 ml Agarose
Stock Solution	56 µl in 1944µl PBS= 28µg Fe/ml	625 µl in 2 ml Agarose = 6.6 µg Fe/ml	140µl in 1860µl PBS= 28 µg Fe/ml	625 µl in 2 ml Agarose = 6.6 µg Fe/ml
Dilution 1	1ml Stock Solution + 1 ml PBS = 14 µg Fe/ml	625 µl in 2 ml Agarose = 3.3 µg Fe/ml	1ml Stock Solution + 1 ml PBS = 14 µg Fe/ml	625 µl in 2 ml Agarose = 3.3 µg Fe/ml
Dilution 2	1 ml Dilution 1 + 1ml PBS = 7 µg Fe/ml	625 µl in 2 ml Agarose = 1.66 µg Fe/ml	1 ml Dilution 1 + 1ml PBS = 7 µg Fe/ml	625 µl in 2 ml Agarose = 1.66 µg Fe/ml
Dilution 3	1 ml Dilution 2 + 1ml PBS = 3.5 µg Fe/ml	625 µl in 2 ml Agarose = 0.833 µg Fe/ml	1 ml Dilution 2 + 1ml PBS = 3.5 µg Fe/ml	625 µl in 2 ml Agarose = 0.833 µg Fe/ml

Table C.4: Details of phantom preparation for different types of iron –PLLA nanoparticles (Batch II).

	Resovist®	Fe Conc. in 2 ml Agarose	MU 119-5zdz N2	Fe Conc. in 2 ml Agarose
Stock Solution	2 µl in 2 ml PBS = 28 µg Fe/ml	625 µl in 2ml Agarose = 6.6 µg Fe/ml	20.9 µl in 1980 µl PBS= 28 µg Fe/ml	625 µl in 2 ml Agarose = 6.6 µg Fe/ml
Dilution 1	1 ml Stock Solution + 1ml PBS = 14 µg Fe/ml	625 µl in 2 ml Agarose = 3.3 µg Fe/ml	1ml Stock Solution + 1 ml PBS = 14 µg Fe/ml	625 µl in 2 ml Agarose = 3.3 µg Fe/ml
Dilution 2	1 ml Dilution 1 + 1 ml PBS = 7 µg Fe/ml	625 µl in 2ml Agarose = 1.66 µg Fe/ml	1 ml Dilution 1 + 1ml PBS = 7 µg Fe/ml	625 µl in 2 ml Agarose = 1.66 µg Fe/ml
Dilution 3	1ml Dilution 1 + 1ml PBS = 3.5 µg /Fe/ml	625 µl in 2ml Agarose = 0.833 µg Fe/ml	1 ml Dilution 2 + 1ml PBS = 3.5 µg Fe/ml	625 µl in 2 ml Agarose = 0.833 µg Fe/ml
	MU 130-5zdz	Fe Conc. in 2 ml Agarose	MU 119-5zdz N3+N4	Fe Conc. in 2 ml Agarose
Stock Solution	21,8 µl in 1979 µl PBS= 28 µg Fe/ml	625 µl l in 2 ml Agarose = 6.6 µg Fe/ml	20,5 µl in 1980 µl PBS = 28 µg Fe/ml	625 µl in 2ml Agarose = 6.6 µg Fe/ml
Dilution 1	1ml Stock Solution + 1 ml PBS = 14 µg Fe/ml	625 µl in 2 ml Agarose = 3.3 µg Fe/ml	1ml Stock solution +1 ml PBS = 14 µg Fe/ml	625 µl l in 2 ml Agarose = 3.3 µg Fe/ml
Dilution 2	1 ml Dilution 1 + 1ml PBS = 7 µg Fe/ml	625 µl l in 2 ml Agarose = 1.66 µg Fe/ml	1ml Dilution 1 + 1ml PBS = 7 µg Fe/ml	625 µl in 2ml Agarose = 1.66 µg Fe/ml
Dilution 3	1 ml Dilution 2 + 1ml PBS = 3.5 µg Fe/ml	625 µl in 2 ml Agarose = 0.833 µg Fe/ml	1 ml Dilution 2 + 1 ml PBS = 3.5 µg Fe/ml	625 µl in 2ml Agarose = 0.833 µg Fe/ml

Table C.5: Details of phantom preparation for Resovist<sup>®</sup> labeled cells.

Sample	Details
Sample 1: Neg Control	2% Agarose and about 250 000 unlabeled cells per ml
Sample 2	250 000 labeled cells per ml in 2% Agarose
Sample 3	125 000 Resovist <sup>®</sup> labeled cells per ml in 2% Agarose
Sample 4	62 500 Resovist <sup>®</sup> per ml labeled cells in 2 % Agarose
Sample 5	31 250 Resovist <sup>®</sup> labeled cells in 2% Agarose
Sample 6	15 600 Resovist <sup>®</sup> labeled per ml cells in 2% Agarose
Sample 7	7800 Resovist <sup>®</sup> labeled cells per ml in 2% Agarose
Sample 8	0.5 µl in 0.5 ml Medium Resovist <sup>®</sup> in 2.5 ml Agarose 2%
Positive Control Resovist <sup>®</sup>	

Table C.6: Details of phantom preparation for Resovist<sup>®</sup> labeled cells (Focus was on lower cell number)

Sample 1	7 µg/ml Resovist <sup>®</sup> in 2 ml Agarose 2%
Positive Control Resovist <sup>®</sup>	(2µl Resovist <sup>®</sup> in 2 ml PBS – there of 1 ml in 4 ml Agarose 2%)
Sample 2	32 000 Resovist <sup>®</sup> PLL (50/0.75) labeled cells in 1 ml PBS diluted in 4 ml Agarose 2%
Sample 3	16 000 Resovist <sup>®</sup> PLL (50/0.75) labeled cells in 1 ml PBS diluted in 4 ml Agarose 2%
Sample 4	8000 Resovist <sup>®</sup> PLL (50/0.75) labeled cells in 1 ml PBS diluted in 4 ml Agarose 2%
Sample 5	4000 Resovist <sup>®</sup> PLL (50/0.75) labeled cells in 1 ml Medium diluted in 4 ml Agarose 2%
Sample 6	32000 unlabeled cells diluted in 1 ml PBS in 4 ml Agarose 2%
Negative Control	



Kinetic study explained in section C and D (chapter 4) were aimed to

- To test (MR Imaging and Prussian Blue Staining), how the MR Signal and the intracellular iron content (Prussian Blue Staining) develops 24, 48 and 96 hours after withdrawal of the iron containing nutrition medium in MSCs seeded in a density with low stimulation to divide (high density seeding).
- To test (MR Imaging and Prussian Blue Staining), how the MR Signal and the intracellular iron content (Prussian Blue Staining) develops 24, 48 and 96 hours after withdrawal of the iron containing nutrition medium in MSCs seeded in a density with high stimulation to divide (low density seeding)

Table C.7: Phantom preparation for sample at imaging time points 0 h (directly after 24 hour incubation with Resovist®)

Sample	Details
Sample 1	7 µg iron/ml Resovist® Agarose 2%
Positive Control Resovist®	0.75 µl Resovist® in 1 ml PBS 0.5 ml in 1 ml Agarose %
Sample 2 - directly after 24 h incubation with PLL/ Resovist®	200 000 cells/ ml 24 hour incubated with Resovist®/PLL 0.3 mio cells in 0.5 ml PBS diluted in 1 ml Agarose 2%
Sample 3 – directly after 24 h incubation with Resovist®/PLL	50 000 cells/ml 75 000 cells in 0.5 PBS diluted in 1 ml Agarose 2%
Sample 4	200 000 unlabeled cells per ml
Negative Control	0.3 mio cells in 0.5 ml PBS in 1 ml Agarose 2%

Table C.8: Phantom preparation for samples at imaging time points 24 h, 48 h, and 96 h.

Sample	Details
Sample 1	7 µg iron/ml Resovist® Agarose 2%
Positive Control Resovist®	0.75 µl Resovist in 1 ml PBS. 0.5 ml in 1 ml Agarose %
Sample 2 – low stimulation to divide	200 000 cells/ ml of high density seeded cells 24 h; 48 or 96 hours after iron withdrawal. 0.3 mio cells in 0.5 ml PBS diluted in 1 ml Agarose 2%
Sample 3 high stimulation to divide	200 000 cells/ ml of low density seeded cells 24h; 48 or 96 hours after iron withdrawal. 0.3 mio cells in 0.5 ml PBS diluted in 1 ml Agarose 2%
Sample 4	200 000 unlabeled cells per ml
Neg Control	0.3 mio cells in 0.5 ml PBS in 1 ml Agarose 2%
Sample 5 – low stimulation to divide	50 000 cells/ml of high density seeded cells 24 h, 48 h or 96 h after iron withdrawal
Sample 6 – high stimulation to divide	50 000 cells/ml of low density seeded cells after 24 h, 48h or 96 h after iron withdrawal

Table C.9: Phantom preparation for sample at imaging time point 144 h (144 h after withdrawal of Resovist®/PLL).

Sample	Details
Sample 1	7 µg iron/ml Resovist® Agarose 2% ,0.75 µl Resovist® in 1 ml PBS,
Positive Control Resovist®	0.5 ml in 1 ml Agarose %
Sample 2 PLL/ Resovist®	200 000 cells/ ml 24 hour incubated with Resovist®/PLL
Low density seeded cells 144 after Resovist® withdrawal	144 after withdrawal 0.3 mio cells in 0.5 ml PBS diluted in 1 ml Agarose 2%
Sample 3	50 000 cells/ml 24 hours incubated with Resovist®/PLL 144 after withdrawal 75 000 cells in 0.5 PBS diluted in 1 ml Agarose 2%
Sample 4	200 000 unlabeled cells per ml
Neg Control	0.3 mio cells in 0.5 ml PBS in 1 ml Agarose 2%

Table C.10: Phantom preparation for kinetic study of particle MU 119-5zdz N3+N4.

96 h after particle removal	
Row 1	200 000 cells per ml (0.5 ml PBS in 1 ml Agarose) high density seeded (200
Sample 1	000 cells per well)
Row 1	50 000 cells per ml (0.5 ml PBS in 1 ml Agarose) high density seeded (200 000
Sample 2	cells per well)
Row 1	200 000 cells per ml (0.5 ml PBS in 1 ml Agarose) low density seeded (50 000
Sample 3	cells per well)
Row 1	50 000 cells per ml (0.5 ml PBS in 1 ml Agarose) low density seeded (50 000
Sample 4	cells per well)
24h after particle removal	
Row 2	Negative Control
Sample 1	200 000 cells per ml unlabeled (0.5ml PBS in 1 ml Agarose)
Row 2	200 000 cells per ml 24 hours after particle removal dense seeded (0.5 ml PBS
Sample 2	in 1 ml Agarose)
Row 2	50 000 cells per ml 24 h after particle removal dense seeded (0.5 ml PBS in 1
Sample 3	ml Agarose)
Row 2	Negative Control
Sample 4	50 000 cells / ml
Directly after incubation	
Row 3	200 000 cells per ml directly after incubation (0.5 ml PBS in 1 ml Agarose)
Sample 1	
Row 3	Negative Control
Sample 2	200 000 cells per ml (0.5 ml PBS 1ml Agarose)
Row 3	Negative Control
Sample 3	50 000 cells per ml (0.5 ml PBS 1ml Agarose)
Row 3	50 000 cells per ml directly after incubation (0.5 ml PBS in 1 ml Agarose)
Sample 4	
Agarose only 1	0.5 ml PBS in 1 ml Agarose
Agarose only 2	0.5 ml PBS in 1 ml Agarose

## Acknowledgement

The work presented in this thesis has been made possible by the association of many people and I would like to take this opportunity to acknowledge their contributions. First and foremost I thank the ALMIGHTY for giving me this opportunity and strength for completing this thesis.

It gives me immense pleasure to express my deep sense of gratitude and sincere thanks to my research supervisor, Prof. Dr. rer. nat. Volker Rasche. He is not only a great professor with deep vision, but also a very kind person. I am indebted to him for exposing me to this exciting, interesting and challenging area of research. His tireless enthusiasm was always a source of motivation and inspiration throughout the duration of my work. His constant support was invaluable and went a long way towards the completion of this thesis. At this point I would like to express my sincere thanks to our Head of the Department Prof. Vinzenz Hombach for giving me an opportunity to work in this department. I would like to thank Dr. Axel Bornstedt for helping me in learning many new things in the lab. I cannot forget help of Dr. Robert Manzke's in X-ray analysis when I needed that most.

My thesis involves a lot of collaborative work both within our university and outside. Special thanks go to Prof. Katharina Landfester (MPI, Mainz) for providing me lab facilities to synthesize polymer loaded nanocapsules during my first year of research. I would like to thank Dr. Nicole Jagielski, Dr. Umaporn Paiphansiri and Markus Urban from Prof. Katharina Landfester's group for their active collaborations. I sincerely thank Prof. Paul Walther, Prof. U. Kaiser and Dr. A. Chuvilin (Electron Microscopy Group of Materials Science, University of Ulm) for their help in characterizing the nanocapsules using various advanced microscopic techniques. Very special thanks to Dr. Dirk Dautzenberg (Radiochemistry Department, TU-Munich) for doing ICP measurements of the samples.

Dr. G.Schmidtke-Schrezenmeier contribution to my thesis is very valuable and I would like to sincerely thank her.

I would like to express my sincere thanks to Dr. Alexander Oberhuber for providing me the carotids samples. I cannot forget the helps rendered by Regine Baur. I learned many experimental techniques from her. Thanks to Prof. Anitha Ignatius (Institute for Experimental Surgery and Biomechanics, University of Ulm) for her kind collaboration and to Ursula Maile for doing plastic histology for many of my samples without any hesitation.

I would like to thank my lab mate Anja Lutz deep down from my heart for being very warm and friendly. Besides, I would like to thank Lucy Gruenfelder and Rahime Celik for their helps in various stages. I acknowledge the friendly and very cooperative attitude of all my MRI room colleagues, Dr. Markus, Dr. Spiess, Dr. Peter, Dr. Nico, Anne, Magda, Utah, Rita. I really enjoyed staying in MRI scanner room because of these friendly colleagues.

Very special thanks to my second family in Ulm (Srikant, Bavani Srikant, Divya and Vidya). Thanks a lot for taking care of me like a family member. Thanks to my very special German friends Benjamin Schulte and Alexandra Zaik for making my stay in Germany a very memorable one. Many thanks to my friends Vinayak, Srinath, Sudarshan, Amarjeet and Amit. Special thanks to Meghna, Smitha, and Vikas for their constant support throughout my thesis.

I would like to thank Dr. P.R. Rajamohanam (NCL, Pune, India) for giving me the flavor of research for the first time.

Last but not the least, I would like to thank all my family members especially my grandmother, father, mother, sisters, brothers in law, brothers, sisters in law, nieces and nephews for their unconditional support and love which gave me the strength to stay alone and finish this thesis. A special thanks to Sankar for his love and support right from the moment I landed in Germany. Thanks for all the literature and books.

**CURRICULUM VITAE**

Name	Sonu Sharma	
Email address	sonusharma128@gmail.com	
Date of birth	12-04-78	
Education	2006-2009	Doctoral Thesis: “MRI studies of Gadolinium based contrast agents loaded nanocapsules and iron loaded nanoparticles in chemical and biological environment”.
	2002-2004	Master of Technology (M.Tech) in Modern Methods of Analytical Chemistry; Department of Chemistry, I.I.T. Delhi, New Delhi.
	1999-2001	Master of Science (M.Sc.) in Organic Chemistry Department of Chemistry University of Jodhpur, Rajasthan, India.
	1996-1999	Bachelor of Science (B.Sc.) in Chemistry (Botany and Zoology as Ancillaries)
Working Experience	July 2004 – March 2006	Senior Research Fellow at National Chemical Laboratory (NCL, Pune).

## **Publications list**

### **Peer reviewed Journals:**

- Jagielski N, Sharma S, Hombach V, Mailänder V, Rasche V, Landfester K: Nanocapsules Synthesized by Miniemulsion Technique for Application as New Contrast Agent Materials. *Macromol. Chem. Phys.* 208: 2229-2241 (2007).
- Sharma S, Paiphansiri U, Hombach V, Mailänder V, Landfester K, Rasche V: Characterization of MRI contrast agent loaded polymeric nanocapsules as versatile vehicle for targeted imaging (*Contrast Media and Molecular Imaging*-under revision).
- Sharma S, Boujraf S, Bornstedt A, Rasche V. Quantification of Calcifications in Endarterectomy Samples by means of high-resolution ultra-short TE imaging *Investigative Radiology* (In Press)

### **International Conferences:**

- Jagielski N, Sharma S, Hombach V, Mailänder V, Rasche V, Landfester K: Nanocapsules Synthesized by Miniemulsion Technique as Versatile New Contrast agent Materials; Poster accepted in Joint Molecular Imaging Conference, Providence, Rhode Island, (USA), 2007.
- Sharma S, Paiphansiri U, Schmitz J, Hombach V, Mailänder V, Landfester K, Rasche V: Contrast Agent Loaded Functionalized Polyurethane Nanocapsules as Versatile Vehicle for Targeted Imaging; Poster accepted in World Molecular Imaging Congress, Nice (France), 2008.
- Sharma S, Boujraf S, Bornstedt A, Rasche V: Quantification of Calcifications in Endarterectomy Samples by Means of High-resolution Ultra-short TE Imaging; Poster accepted in International Society For Magnetic Resonance in Medicine, Honolulu, Hawaii, (USA), 2009.
- Rasche V, Hombach V, Sharma S, Schmidtke-Schrezenmeier G Bornstedt A: Bright-iron imaging applying an off-resonance modulating pre-pulse (OMPP); Poster accepted in International Society For Magnetic Resonance in Medicine, Honolulu, Hawaii, (USA), 2009.
- Schmidtke-Schrezenmeier G, Urban M, Sharma S, Dausend J, Rojewski M, Mailänder V, Rasche V, Landfester K, Schrezenmeier H: A promising candidate for cell-labeling to allow studies on in-vivo trafficking of advanced cell therapies by Magnetic Resonance Imaging (MRI); Accepted in Joint Annual Meeting of the German, Austrian and Swiss companies of Haematology and Oncology, 2009.





